Doctoral Dissertation (Shinshu University)

Space weather observations with the Global Muon Detector Network

March 2016

Masayoshi Kozai

Department of Materials Science and Engineering,
Interdisciplinary Graduate School of Science and Technology,
Shinshu University

Contents

Abstract

Intensity of galactic cosmic rays (GCRs) shows dynamic temporal variations in various time scales; transient decreases lasting for several days, diurnal variation, 11-year or 22-year cycle variation, and so on. Only a worldwide detector network allows us to separately deduce variations of the isotropic intensity (or GCR density) and the anisotropy on an hourly basis. In this thesis, I present results of the space weather study based on the GCR observations with the Global Muon Detector Network (GMDN).

In former works analyzing a single detector data, diurnal (or ecliptic) and north-south (NS) anisotropies were derived on a daily basis from separate analysis methods and/or separate detectors. The GMDN, on the other hand, provides us with a three-dimensional (3D) anisotropy using a single analysis method on an hourly basis. I confirm that the anisotropy is more accurately derived by the GMDN than by the traditional analysis, while results obtained from two analyses are fairly consistent with each other as far as the yearly mean value is concerned.

Based on the convection-diffusion equation describing the large-scale transport of GCRs in the interplanetary space, the spatial gradient of GCR density is deduced from the observed anisotropy. High temporal resolution of the GMDN allows us to infer the spatial structure of the GCR depleted region formed behind the interplanetary shock (IP-shock) which causes a short-term density decrease (called Forbush Decreases; FDs) on its arrival at the earth. By analyzing FDs following the IP-shocks generated by the solar eruptions (such as coronal mass ejections; CMEs) from various heliographic locations on the sun, I derive the 3D average distribution of GCRs in the depleted region for the first time. It is confirmed that the magnetic sheath in the western flank of IP-shock excludes more GCRs than in the eastern flank, in accord with the east-west asymmetric magnetic configuration model of IP-shock expected from the spiral configuration of the interplanetary magnetic field (IMF) arising from the solar rotation. I also confirm the density gradient suggesting a density minimum in an expanding CME propagating radially outward from the eruption location on the sun. The FDs observed simultaneously by the neutron monitors (NMs) and the GMDN, which are sensitive to $\sim$ 10 GV and $\sim$ 60 GV GCRs, respectively, show a soft rigidity spectrum of the FD.

I also analyze the year-to-year variation of the 3D anisotropy using the GMDN for the first time. The first order anisotropy observed with the GMDN from 1992 to 2013 shows a variation in a correlation with the solar activities. Amplitude of the diurnal anisotropy shows 11-year cycle variation in a correlation with the solar activity, while the phase varies according to the 22-year periodic reversals of the solar dipole magnetic field polarity, referred as the $A > 0$ ($A < 0$) epoch when the dipole directs northward (southward). I find that the anisotropy component parallel to the IMF in the ecliptic plane shows a 22-year cycle variation which is responsible to the phase variation of the diurnal anisotropy. NS component of the gradient indicates a local density maximum close to the heliospheric current sheet (HCS) in $A < 0$ epoch while the gradient indicates a local minimum close to the HCS in $A > 0$ epoch. This 22-year variation of the gradient is in an agreement with the drift model prediction. The radial density gradient, on the other hand, does not show a clear 22-year variation predicted by the drift model, while it shows a significant 11-year variation. The parallel mean free path of the pitch angle scattering of GCRs deduced from the anisotropy and the radial gradient also show significant 11-year variations out of phase with each other, indicating equilibrium between the radial diffusion and the solar wind convection of GCRs. The parallel mean free path has an average magnitude of $\sim$ 1 AU for $\sim$ 60 GV GCRs which is comparable to the numerical simulation of the pitch angle scattering.

In addition to the GMDN data, I also analyze GCRs recorded by a single muon detector (MD) at Nagoya over 44 years from 1970 to 2013. The diurnal anisotropy is derived from the diurnal variation of the muon count rate, while the NS anisotropy is derived from a difference between count rates (called the "GG-component") recorded by the north-viewing channel and the south-viewing channel of Nagoya MD. The 3D anisotropy is deduced by combining the diurnal anisotropy and the NS anisotropy. From the long-term variation over 4 solar activity cycles, I find a small 22-year variation of the radial gradient, but it is masked by a larger 11-year variation and by a persistent long-term trend over the last several solar cycles. It is also found that the anisotropy parallel to the IMF, i.e. the parallel diffusion streaming of GCRs, has a flat

rigidity spectrum, while the perpendicular anisotropy mainly arising from the drift streaming has a harder spectrum.

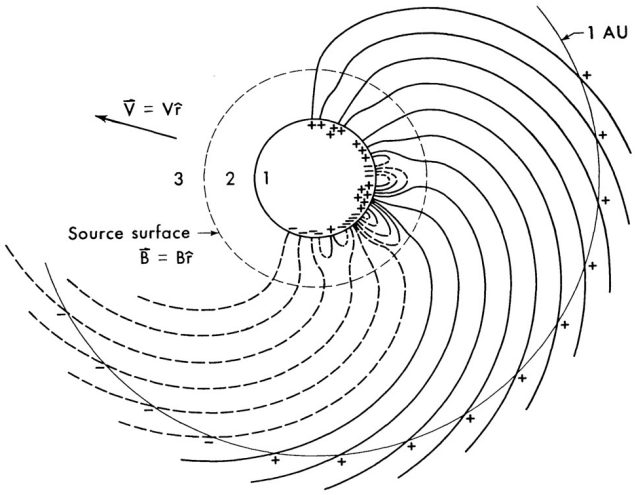

Figure 1: Schematic view of the Parker spiral. The central solid line circle represents the solar surface. Currents flowing near the source surface eliminate the transverse components of the magnetic field, and the solar wind extends the source surface magnetic field into interplanetary space. (Schatten et al., 1969)

1 Introduction

1.1 Solar modulation of galactic cosmic rays (GCRs)

Existence of the solar wind, supersonic plasma flow from the sun, was first suggested by Biermann (1957) from the acceleration of the ion tails of comets. Based on a dynamical model, Parker (1958) predicted the super sonic solar wind and suggested that the solar dipole magnetic field frozen-in (Alfvén, 1942) the solar wind moves with the solar wind and forms a spiral configuration (Parker spiral; Figure 1) of the interplanetary magnetic field (IMF). The existences of the solar wind and the Parker spiral have been confirmed by a number of spacecraft observations. The solar wind moving radially outward from the sun reduces its pressure by the adiabatic expansion until it decelerates at the solar wind termination shock (TS) formed around 100 AU from the sun. Beyond the TS, there is a boundary called the heliopause where the solar wind pressure balances with the interstellar gas. The region filled with the solar wind plasma inside the heliopause is called the heliosphere. Galactic cosmic rays (GCRs) in the interstellar space interact with the IMF and its irregularities moving outward from the sun and form a characteristic density distribution in the heliosphere, i.e. the density distribution formed by the solar modulation of GCRs.

1.1.1 Transport equation of GCRs in the interplanetary space

Transport equation of GCRs The transport equation (or continuity equation) of GCRs in the interplanetary space is given (cf. Parker, 1965; Gleeson & Axford, 1967; Gleeson, 1969; Gleeson & Webb, 1980; Webb & Gleeson, 1979) as

$$\frac{\partial U}{\partial t} + \frac{\partial}{\partial \boldsymbol{r}} \cdot \boldsymbol{S} = -\frac{\partial}{\partial p}\left(\frac{p\boldsymbol{V}_{\rm SW}}{3} \cdot \frac{\partial U}{\partial \boldsymbol{r}}\right) \tag{1}$$

where the particle position $\boldsymbol{r}$, momentum p, and time t are specified in the frame fixed in the solar system and $\boldsymbol{V}_{\rm SW}$ is the solar wind velocity. A term on the right hand side of equation (1) represents the adiabatic cooling of GCRs arising from the expansion of the radial solar wind. $U(\boldsymbol{r}, p, t)$ and $\boldsymbol{S}(\boldsymbol{r}, p, t)$ are the differential number density and the bulk flow of GCRs related to

the phase-space density $F(\boldsymbol{r}, \boldsymbol{p}, t)$ as

$$U(\boldsymbol{r}, p, t)\Delta p = \int_{\tau_p} F(\boldsymbol{r}, \boldsymbol{p}, t) d^3p, \tag{2}$$

$$\boldsymbol{S}(\boldsymbol{r}, p, t)\Delta p = \int_{\tau_p} \boldsymbol{v} F(\boldsymbol{r}, \boldsymbol{p}, t) d^3p \tag{3}$$

where τ_p is the region in the momentum space surrounded by two spheres of radii p and $p + \Delta p$ and $\boldsymbol{v}$ is the particle velocity.

The GCR flow $\boldsymbol{S}$ is expressed as

$$\boldsymbol{S} = CU\boldsymbol{V}_{\rm SW} - \mathbf{K} \cdot \frac{\partial U}{\partial \boldsymbol{r}} \tag{4}$$

where the first and second terms in the right side represent the convection and diffusion flows of GCRs, respectively.

$$C = 1 - \frac{1}{3U}\frac{\partial (pU)}{\partial p} \tag{5}$$

is the Compton-Getting factor (Compton & Getting, 1935; Gleeson & Axford, 1968a; Cutler & Groom, 1986; Amenomori et al., 2004). The second term of the right side in equation (5), which depends on the momentum spectrum of the density $U(p)$, arises from a change of the momentum spectrum due to the transformation of the reference frame from the solar wind frame moving with $\boldsymbol{V}_{\rm SW}$ to the fixed frame (Gleeson & Axford, 1968a). $\mathbf{K}$ is the diffusion tensor representing the diffusion and drift effects of GCRs and written in an orthogonal coordinate system $(\boldsymbol{e}_1, \boldsymbol{e}_2, \boldsymbol{e}_3)$ with $\boldsymbol{e}_1$ parallel to the mean IMF which remains after averaging small fluctuations of the magnetic field, as

$$\mathbf{K} = \begin{pmatrix} K_\parallel & 0 & 0 \\ 0 & K_\perp & K_T \\ 0 & -K_T & K_\perp \end{pmatrix}. \tag{6}$$

$K_\parallel$ is the diffusion coefficient parallel to the IMF given as

$$K_\parallel = \frac{\lambda_\parallel v}{3} \tag{7}$$

where $\lambda_\parallel$ is the mean free path of the GCR pitch angle scattering (Jokipii, 1971) in the direction parallel to the IMF. $K_\perp$ is the diffusion coefficient perpendicular to the IMF given as

$$K_\perp = \frac{1}{1 + \alpha_\parallel^2} K_\parallel \tag{8}$$

where

$$\alpha_\parallel = \lambda_\parallel / R_L \tag{9}$$

is the dimensionless mean free path parallel to the IMF normalized to the Larmor radius of GCR particles in the mean IMF, R_L. In many cases of the solar modulation, $K_\perp$ is significantly smaller than $K_\parallel$ by $1/(1 + \alpha_\parallel^2)$ because of a large $\alpha_\parallel$.

$$K_T = \frac{\alpha_\parallel}{1 + \alpha_\parallel^2} K_\parallel \tag{10}$$

is the off-diagonal diffusion coefficient representing the diamagnetic drift effect.

Force-field solution The force-field solution (Gleeson & Axford, 1968b; Gleeson & Urch, 1973) of equation (1) allows us a simple estimation of the solar modulation of GCRs. On the spherically-symmetric assumption, equation (4) is replaced by

$$S_r = CUV_{\rm SW} - K_{rr}\frac{\partial U}{\partial r} \tag{11}$$

where r is the radial distance from the sun, S_r is the radial component of the bulk flow, and

$$K_{rr} = K_{\parallel}\cos^2\psi + K_{\perp}\sin^2\psi \tag{12}$$

is the radial diffusion coefficient with ψ denoting an angle between the Parker spiral and the radial direction. If the angular distribution of GCRs is nearly isotropic, i.e. the integration in equation (3) is nearly zero ($S_r \sim 0$), we obtain from equation (11)

$$G_r = \frac{1}{U}\frac{\partial U}{\partial r} = \frac{CV_{\rm SW}}{K_{rr}} \tag{13}$$

where G_r is the radial (fractional) density gradient of GCRs. The radial distribution $U(r)$, therefore, is derived as

$$U(r) = U(r_B)\exp\left(-\int_r^{r_B}\frac{CV_{\rm SW}}{K_{rr}}dr\right) \tag{14}$$

where r_B is the position of the heliospheric boundary. For the GCRs with relativistic speeds, momentum spectrum $U(p)$ is expressed by the power-law spectrum $\propto p^{-\gamma}$ with $\gamma \sim 2.7$ and C becomes a constant

$$C = \frac{2+\gamma}{3} \tag{15}$$

according to equation (5). $U(r)$ in equation (14), therefore, increases with increasing r, i.e. the radial density gradient G_r is positive (outward gradient). This implies that the outward convection flow represented by the first term of the right side in equation (11) balances with the inward diffusion flow represented by the second term which arises from the radial density gradient resulting from the convection.

The radial density gradient (or positive G_r) has been confirmed by a number of in situ observations with spacecraft (e.g. Neher & Anderson, 1964; O'Gallagher, 1967; O'Gallagher & Simpson, 1967) and $S_r \sim 0$ in the steady state, i.e. the balance between the convection and diffusion flows, is also roughly confirmed from ground-based observations of the GCR anisotropy (e.g. Rao et al., 1963; Bercovitch, 1963). We can, therefore, conclude that the convection-diffusion equilibrium mentioned above plays a primary (or major) role in the solar modulation of GCRs.

1.1.2 The first order anisotropy of GCRs

The force-field model mentioned in the previous section assumes a spherically-symmetric transport of GCRs in equation (11). I note, however, that the azimuthal and latitudinal components of $\boldsymbol{S}$ are almost always detected with a substantial value. This indicate that there is a limit to deduce a correct density distribution of GCRs using the force-field model. Observation of the three-dimensional GCR anisotropy which is eliminated in derivation of the equation (13), on the other hand, allows us to infer the density gradient $\partial U/\partial \boldsymbol{r}$ via equation (4) without such an assumption.

The first order anisotropy and the density gradient The GCR anisotropy at a space-time $(\boldsymbol{r}, t)$ is represented by the phase space density $F(\boldsymbol{p})$ which is a function of an observed momentum magnitude p. $F(\boldsymbol{p})$ is expanded in the spherical harmonics in the polar coordinate system (p, θ, ϕ) as

$$F(\boldsymbol{p}) = \sum_{n=0}^{\infty} Y_n(p,\theta,\phi) = \sum_{n=0}^{\infty}\sum_{m=0}^{n}\left\{F_n^{mc}(p)\cos m\phi + F_n^{ms}(p)\sin m\phi\right\}P_n^m(\cos\theta) \tag{16}$$

where θ and ϕ are orientation angles of a vector $\boldsymbol{p}$ and $P_n^m(\cos\theta)$ is the semi-normalized spherical function by Schmidt (Chapman & Bartels, 1940). The zeroth and first harmonics, $Y_0(p,\theta,\phi)$ and $Y_1(p,\theta,\phi)$ are related with the GCR density $U(p)$ and bulk flow $\boldsymbol{S}(p)$ (e.g. Klimas & Sandri, 1971; Gleeson, 1969; Gleeson & Webb, 1980) as

$$Y_0(p,\theta,\phi)\Delta p = F_0^{0c}(p)\Delta p = \frac{1}{4\pi p^2}\int_{\tau_p} F(\boldsymbol{p})d^3p = \frac{1}{4\pi p^2}U(p)\Delta p, \tag{17}$$

$$\left(F_1^{1c}(p), F_1^{1s}(p), F_1^{0c}(p)\right)\Delta p = \frac{3}{4\pi p^2}\int_{\tau_p}\frac{\boldsymbol{v}}{v}F(\boldsymbol{p})d^3p = \frac{3}{4\pi v p^2}\boldsymbol{S}(p)\Delta p. \tag{18}$$

The first order anisotropy vector, $\boldsymbol{\xi}(p)$ is defined as

$$\boldsymbol{\xi}(p) = -\frac{1}{F_0^{0c}(p)}\left(F_1^{1c}(p), F_1^{1s}(p), F_1^{0c}(p)\right). \tag{19}$$

From equations (4), (17) and (18), $\boldsymbol{\xi}(p)$ is related to the GCR flow $\boldsymbol{S}$ and the density gradient $\partial U/\partial \boldsymbol{r}$ as

$$\boldsymbol{\xi} = -\frac{3\boldsymbol{S}}{vU} = -\frac{3C}{v}\boldsymbol{V}_{\rm SW} + \frac{3}{vU}\mathbf{K}\cdot\frac{\partial U}{\partial \boldsymbol{r}}. \tag{20}$$

The anisotropy vector $\boldsymbol{\xi}$ is defined to direct opposite to $\boldsymbol{S}$, pointing toward the upstream direction of $\boldsymbol{S}$. On the frame fixed to the earth moving around the sun with the orbital motion velocity $\boldsymbol{V}_E$, the solar wind velocity $\boldsymbol{V}_{\rm SW}$ is modified to $\boldsymbol{V}_{\rm SW} - \boldsymbol{V}_E$, that is,

$$\boldsymbol{\xi} = -\frac{3C}{v}\left(\boldsymbol{V}_{\rm SW} - \boldsymbol{V}_E\right) + \frac{3}{vU}\mathbf{K}\cdot\frac{\partial U}{\partial \boldsymbol{r}}. \tag{21}$$

The dimensionless mean free path $\alpha_\parallel$ in equation (9) is considered to be $\alpha_\parallel \sim 10$ for ~ 60 GeV GCRs (Bieber et al., 2004) analyzed in this thesis, indicating $\alpha_\parallel^2 \gg 1$. The off-diagonal diffusion coefficient K_T in equation (10), therefore, can be approximated as

$$K_T \sim K_\parallel/\alpha_\parallel = vR_L/3 \tag{22}$$

from equation (7). The perpendicular diffusion coefficient $K_\perp$ in equation (8) is redefined using a mean free path ($\lambda_\perp$) perpendicular to the IMF as

$$K_\perp = \lambda_\perp v/3. \tag{23}$$

Inserting equations (7), (9), (15), (22) and (23) to equation (21), we obtain

$$\boldsymbol{\xi} = -\frac{2+\gamma}{c}\left(\boldsymbol{V}_{\rm SW} - \boldsymbol{V}_E\right) + \begin{pmatrix} \lambda_\parallel & 0 & 0 \\ 0 & \lambda_\perp & R_L \\ 0 & -R_L & \lambda_\perp \end{pmatrix}\cdot\boldsymbol{G} \tag{24}$$

where I replaced the particle speed v with the speed of light, c which is approximately equal to v for GCRs analyzed in this thesis and

$$\boldsymbol{G} = \frac{1}{U}\frac{\partial U}{\partial \boldsymbol{r}} \tag{25}$$

represents the fractional density gradient vector normalized to the density U. It is noted that the first term of the right side in equation (24), representing the solar wind convection flow and the earth's orbital motion around the sun, is independent of the particle momentum p. Equation (24) can be rewritten as

$$\boldsymbol{\xi} = -\frac{2+\gamma}{c}\left(\boldsymbol{V}_{\rm SW} - \boldsymbol{V}_E\right) + \lambda_\parallel\boldsymbol{G}_\parallel + \lambda_\perp\boldsymbol{G}_\perp - R_L\frac{\boldsymbol{B}}{B}\times\boldsymbol{G}_\perp \tag{26}$$

where $\boldsymbol{G}_\parallel$ and $\boldsymbol{G}_\perp$ are the density gradients parallel and perpendicular to the IMF, $\boldsymbol{B}$ is the IMF vector. The second and third terms of the right side in equation (26) represent the diffusion flow of GCRs, while the forth term represents the drift flow (or the diamagnetic drift) arising from a combination of the gyro motion and the density gradient of GCRs. Equation (24) or (26) allows us to deduce the density gradient $\boldsymbol{G}$ in the vicinity of the earth (or to infer the density distribution in the interplanetary space) from the observed anisotropy $\boldsymbol{\xi}$.

Co-rotation anisotropy The first order anisotropy in the ecliptic plane is known to have an amplitude of ~ 0.4 % and a phase at 90° GSE longitude (e.g. Rao et al., 1963; Bercovitch, 1963) in general. From equation (8), the ratio between parallel and perpendicular mean free paths, α is estimated as

$$\alpha = \frac{\lambda_\perp}{\lambda_\parallel} = \frac{K_\perp}{K_\parallel} \sim \frac{1}{1+\alpha_\parallel^2} \sim 0.01 \tag{27}$$

The third term of the right side in equation (26) is, therefore, negligible if $\boldsymbol{G}_\perp$ is comparable with or less than $\boldsymbol{G}_\parallel$ and I also eliminate the fourth term because of $R_L/\lambda_\parallel = 1/\alpha_\parallel \sim 0.1$. The ecliptic (radial and azimuthal) components of $\boldsymbol{\xi}$ in equation (26) are given in the GSE coordinate system, as

$$\xi_x = \frac{2+\gamma}{c} V_{\rm SW} - \lambda_\parallel G_\parallel \cos\psi \tag{28}$$

$$\xi_y = \lambda_\parallel G_\parallel \sin\psi \tag{29}$$

where the earth's orbital motion speed V_E is ignored because its magnitude (30 km/s) is negligible compared with $V_{\rm SW} \sim 400$ km/s. Applying an assumption of $\xi_x \sim 0$, i.e. the radial convection-diffusion equilibrium, we obtain

$$\xi_y = \frac{2+\gamma}{c} V_{\rm SW} \tan\psi \sim 0.6\ \% \tag{30}$$

where I used $\gamma = 2.7$, $V_{\rm SW} = 400$ km/s, and $\psi = 45°$. The difference from the observed anisotropy (~ 0.4 %) is attributed to the contribution from $\boldsymbol{G}_\perp$ which is ignored in this calculation (Gleeson, 1969). This anisotropy is called co-rotation anisotropy and interpreted as the convection flow of GCRs arising from the "co-rotation" of the IMF around the sun.

1.2 Space weather

The force-field model and the co-rotation anisotropy mentioned in the previous sections had provided us with a limited success in the study of GCR modulation, which assume the radial equilibrium between the solar wind convection and the diffusion ($S_r \sim 0$ and $\xi_r \sim 0$). The interplanetary environment including the GCRs actually shows dynamic variations deviating from such an equilibrium state, called the "space weather", because of the dynamic solar activity and the contribution from the latitudinal drift flow which were ignored in the radial convection-diffusion equilibrium. In this thesis, I present results of the space weather study by focusing on two phenomena of the GCR modulation, the GCR density depression behind interplanetary shocks (IP-shocks) and the solar cycle variation of the GCR density distribution. I introduce previous studies related to them in this section.

1.2.1 GCR depression behind interplanetary shocks (IP-shocks)

Short term decreases in the galactic cosmic ray (GCR) isotropic intensity (or density) following geomagnetic storm sudden commencements (SSCs) were first observed by Forbush (1937) (Forbush Decreases, FDs). In general, FDs start with a sudden decrease within 3 hours of the SSC onset (Lockwood, 1960), reach maximum depression within about a day and recovers to the usual level over several days (recovery phase). Most of the decreases follow geomagnetic SSCs but correlation studies between the ground-based cosmic ray data and spacecraft (e.g. Fan et al., 1960) or solar radio (e.g. Obayashi, 1962) data indicate that the origin of the FD is not the geomagnetic storm but the IP-shock associated with the solar eruption such as the coronal mass ejection (CME), which causes the SSC as well (Yermolaev & Yermolaev, 2006; Gopalswamy et al., 2007).

The depleting effect of IP-shocks on GCRs is explained by the "propagating diffusive barrier" model (Wibberenz et al., 1998). The compressed and disturbed magnetized plasma in the sheath behind the IP-shock reduces the GCR diffusion from the outer heliosphere due to the enhanced pitch angle scattering and works as a diffusive barrier. The diffusive barrier suppresses the inward

flow arising from the radial density gradient of GCRs and sweeps out GCRs as it propagates radially outward, forming the GCR depleted region behind the IP-shock.

Investigating a relation between the heliographic longitude of associated solar eruptions on the sun and the magnitude of GCR depression in FDs, a number of studies suggest the east-west asymmetry (E-W asymmetry) of FDs associated with eruptions on the eastern region of the sun have slightly larger magnitude than western eruptions (Kamiya, 1961; Sinno, 1962; Yoshida & Akasofu, 1965; Haurwitz et al., 1965; Barnden, 1973a,b; Cane et al., 1996). It is also reported that large FDs with prominent magnitudes are often observed in association with eruptions near the central meridian of the sun. Yoshida & Akasofu (1965) called this the "center-limb effect". I note, however, that the E-W asymmetry presented by previous papers seems insignificant due to a large event-by-event dispersion of the maximum density depression in FD masking the systematic E-W dependence.

Barnden (1973a,b) and Cane (2000) gave a comprehensive interpretation of the observations including the E-W asymmetry and center-limb effect applying the magnetic configuration model of Hundhausen (1972) to FDs. The IP-shocks associated with solar eruptions are driven by the ejected "driver gas" (Hirshberg et al., 1970), i.e. the interplanetary CME. The central region of the CME (or the CME ejecta), whose longitudinal extent is less than 50° at 1 AU (Cane & Richardson, 2003), is detected only for IP-shocks originating near the central meridian, while the accompanying shock formed ahead of the CME has a greater longitudinal extent exceeding 100° (Cane, 1988). A closed magnetic field configuration called the magnetic flux rope (MFR) is formed in the central region of the CME (Burlaga et al., 1981; Klein & Burlaga, 1982). Expansion of the MFR excludes GCRs from penetrating into the MFR, causing a prominent FD as found by Cane et al. (1996). The E-W asymmetry, on the other hand, is attributed to the IP-shock which has a global effect on the GCRs (Cane et al., 1994). The interplanetary magnetic field (IMF) has a spiral configuration known as the Parker spiral (Parker, 1958) and the eruption site on the solar photosphere moves toward west due to the sun's rotation before the IP-shock arrives at the earth. The compressed IMF in the sheath of IP-shock, therefore, has a larger magnitude at the western flank of the IP-shock than at the eastern flank, leading to a small diffusion coefficient of the GCR pitch angle scattering (Jokipii, 1971) and a larger FD in the eastern events. This CME-driven shock model is also consistent with the observed longitudinal distribution of the solar energetic particles (Reames, 1995; Reames et al., 1996).

In addition to the temporal variation of GCR density, FDs are often accompanied by dynamic variations of the anisotropic intensity of GCRs (or GCR anisotropy) observed with ground-based detectors such as neutron monitors and muon detectors. The cosmic ray counting rate observed with a ground-based detector is known to show a diurnal variation (Hess & Graziadei, 1936), indicating an equatorial GCR flow from the direction of the local time when a maximum count rate is observed. The enhancement of amplitude and the rotation of phase of the diurnal variation accompanying FDs were first reported by Duggal & Pomerantz (1962) and Wada & Suda (1980) performed a statistical analysis of the evolution of diurnal anisotropy for SSC events. Duggal & Pomerantz (1970) and Suda & Wada (1981) also found enhanced north-south asymmetry in GCR intensities observed with the northern and southern geographic polar detectors, indicating an enhancement of the north-south GCR anisotropy in FDs. Combination of the observed diurnal and north-south anisotropies enabled Nagashima et al. (1968) to infer the three-dimensional density distribution. However, after that, such a three-dimensional analysis of the transient anisotropy was rarely performed until a worldwide detector network started operation. The counting rate of a single neutron monitor, which is analyzed in most previous studies, contains contributions from the GCR density and anisotropy superposed to each other and analyzing these two contributions separately has been difficult. Also the analysis of the diurnal variation provides only the daily mean of the equatorial anisotropy, which is insufficient for analyzing the dynamic variation during FDs. This has been a problem also in analysis of the temporal variation of GCR density in previous studies, as pointed out by Cane et al. (1996).

1.2.2 Solar cycle variation of GCRs

Solar cycle variations of the solar wind parameters, such as the solar wind velocity, magnitude and orientation of the solar magnetic field and/or IMF, and the tilt angle of the heliospheric current sheet (HCS), alter the spatial distribution of GCR density in the heliosphere as partly mentioned in Section 1.1. Long-term variations of the interplanetary environment arising from the 11-year and 22-year cycle variations of the sun, i.e. the solar cycle variations of the interplanetary space, are called the "space climate". We can easily expect from the force-field solution (equations (13) and (14)) that the radial density gradient and the density of GCRs at the earth vary in a positive and negative correlations with the 11-year cycle variation of the solar activity, because the turbulent (quiet) magnetic field in the solar activity maximum (minimum) may reduce (enhance) the diffusion coefficient of GCRs, resulting in the large (small) density gradient and the low (high) density.

The drift model (Jokipii & Kopriva, 1979) applied the drift flow of GCRs to the numerical model of the GCR modulation. The diamagnetic drift represented by the fourth term of the right hand side of equation (26) causes an apparent GCR flow which appears as the inflow of GCR particles into an spatial volume element, but does not transport the particles beyond a range of the gyro radius. We can, however, expect a particle transportation traversing the line of magnetic force via other drift processes, if there is a spatial gradient of the magnetic field as in the interplanetary space. From equations (1), (4) and (6), the density variation arising from the drift flow, proportional to the off-diagonal diffusion coefficient K_T, is written as

$$\begin{aligned}\left(\frac{\partial U}{\partial t}\right)_D &= \frac{\partial}{\partial \boldsymbol{r}} \cdot \left\{ \begin{pmatrix} 0 & 0 & 0 \\ 0 & 0 & K_T \\ 0 & -K_T & 0 \end{pmatrix} \cdot \frac{\partial U}{\partial \boldsymbol{r}} \right\} \\ &= \frac{\partial K_T}{\partial x_2}\frac{\partial U}{\partial x_3} - \frac{\partial K_T}{\partial x_3}\frac{\partial U}{\partial x_2} = -\frac{\partial}{\partial \boldsymbol{r}} \cdot (U \boldsymbol{V}_D) \end{aligned} \tag{31}$$

where $\boldsymbol{V}_D$ is the drift velocity defined as

$$\boldsymbol{V}_D = \left(0, \frac{\partial K_T}{\partial x_3}, -\frac{\partial K_T}{\partial x_2}\right) = \frac{\partial}{\partial \boldsymbol{r}} \times \left(K_T \frac{\boldsymbol{B}}{B}\right). \tag{32}$$

The right hand side of equation (31) can be simply understood as a GCR flow convected with a velocity $\boldsymbol{V}_D$ in addition to the solar wind convection represented by the first term of the right hand side of equation (4). From equation (22), the drift velocity in equation (32) is written as

$$\begin{aligned}\boldsymbol{V}_D &= \frac{\partial}{\partial \boldsymbol{r}} \times \left(K_T \frac{\boldsymbol{B}}{B}\right) = \frac{vP}{3c}\frac{\partial}{\partial \boldsymbol{r}} \times \left(\frac{\boldsymbol{B}}{B^2}\right) \\ &= \frac{vP}{3cB^4}\left(B^2 \frac{\partial}{\partial \boldsymbol{r}} \times \boldsymbol{B} + \boldsymbol{B} \times \frac{\partial B^2}{\partial \boldsymbol{r}}\right) \end{aligned} \tag{33}$$

where the Larmor radius R_L is given as $R_L = P/(cB)$ with P denoting the rigidity of GCR particle. The first term in the parenthesis represents the curvature drift arising from the magnetic field curvature $\nabla \times \boldsymbol{B}$, while the second term is the gradient drift (or the ∇B drift) arising from the spatial gradient of the magnetic field magnitude perpendicular to the force line (Parker, 1957; Isenberg & Jokipii, 1979). The orientation of the drift flow in equation (32) clearly depends on the magnetic field orientation. The curvature and the radial gradient of the Parker spiral magnetic field cause a latitudinal GCR flow, which cannot be described by the GCR modulation model (such as the force-field model) taking account of only the convection and diffusion flows.

A polarity of the IMF (pointing away from or toward the sun) is determined by the polarity of the solar magnetic field at the foot point on the sun. The polarity of the solar dipole magnetic field is opposite on the northern and southern sides of the equator forming a sector structure in the heliosphere as shown in the left panel of Figure 2. The boundary surface between the IMF sectors is called the HCS (Wilcox & Ness, 1965) and predicted to form a wavy structure in the heliosphere (Figure 2), due to the tilt of the solar dipole from the solar rotation axis. The

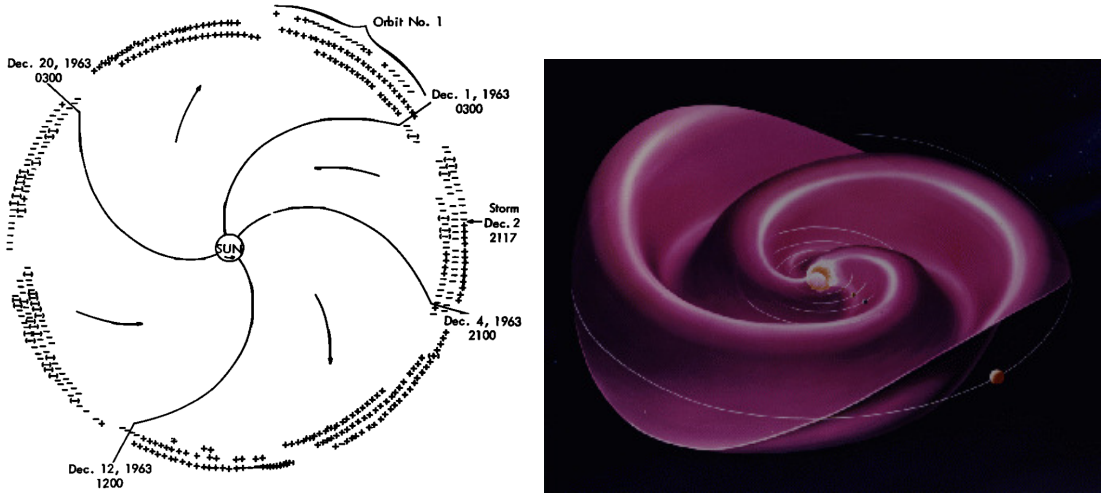

Figure 2: (Left) Sector structure of the IMF observed with IMP 1 spacecraft from December 1963 to February 1964 (Schardt & Opp, 1967). (Right) Schematic view of the wavy HCS [http://wso.stanford.edu/].

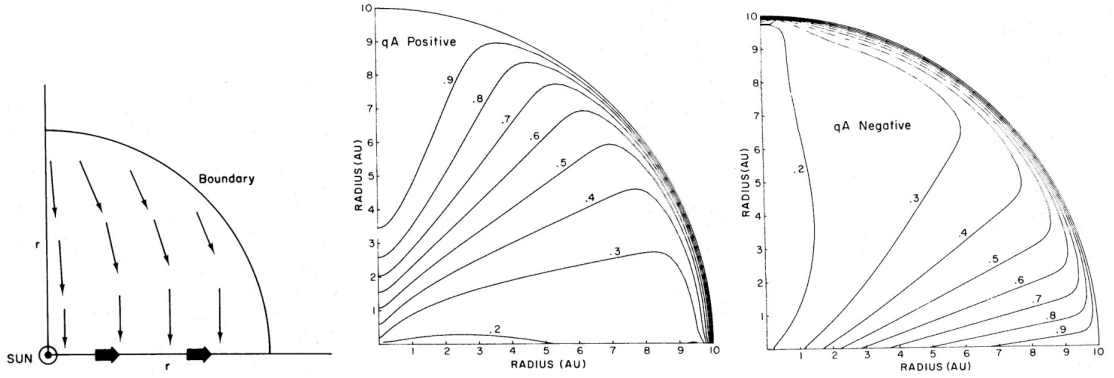

Figure 3: (Left) Latitudinal drift flow of GCRs in the heliosphere in the $A > 0$ epoch. The system is symmetric about both axes. (Middle) GCR density distribution in the heliosphere in the $A > 0$ epoch. (Right) GCR density distribution in the heliosphere in the $A < 0$ epoch. (Jokipii & Kopriva, 1979)

drift model (Figure 3) of GCR transport predicts a bi-directional latitudinal gradient pointing in opposite directions on the opposite sides of the HCS if the HCS is flat (Jokipii & Kopriva, 1979). The predicted spatial distribution of the GCR density has a minimum along the HCS in the "positive" polarity period of the solar polar magnetic field (also referred as $A > 0$ epoch), when the IMF directs away from (toward) the sun in the northern (southern) hemisphere, while the distribution has the local maximum on the HCS in the "negative" period ($A < 0$ epoch) with the opposite field orientation in each hemisphere. The field orientation reverses every 11 years around the maximum period of the solar activity. A tilted current sheet introduces modifications of density distribution around the wavy HCS. For example the local minimum of the density in $A > 0$ epoch does not locate right on the HCS, but the general tendencies in the sense of the latitudinal gradient remain the same as outlined above (Kóta & Jokipii, 1982, 1983).

The variation of the spatial distribution of GCR density causes the variation of the first order anisotropy of GCRs at the earth as expected from equation (24). One of such variations is the 22-year variation of the solar diurnal anisotropy in which the phase of the anisotropy shifts toward earlier hours in the local solar time around every $A > 0$ solar minima (Thambyahpillai & Elliot, 1953; Forbush, 1967; Ahluwalia, 1988; Bieber & Chen, 1991, and references therein). By

analyzing the anisotropy observed with neutron monitors (NMs) in 1968-1988, Chen & Bieber (1993) revealed that the observed phase-shift of the diurnal anisotropy is due to the decrease of the diffusion streaming parallel to the IMF, i.e. the second term ($\lambda_{\parallel} G_{\parallel}$) of the right side of equation (26), in $A > 0$ solar minima. The simple drift model predicts smaller G_r (or smaller $G_{\parallel}$) in $A > 0$ epoch than in $A < 0$ epoch, if the diffusion coefficients are the same in both epochs (Levy, 1976; Erdös & Kóta, 1980; Kóta & Jokipii, 1983; Potgieter & Moraal, 1985). Finding a significant 11-year solar cycle variation but no clear 22-year variation in the observed G_r, however, Chen & Bieber (1993) suggested that the smaller parallel streaming was caused by the smaller $\lambda_{\parallel}$ in the $A > 0$ epoch, possibly due to the magnetic helicity effect in the turbulent magnetic field (Bieber & Pomerantz, 1986; Bieber et al., 1987).

The long-term variation of the north-south (NS) anisotropy normal to the ecliptic plane has been derived also from NM data. Bieber & Pomerantz (1986) and Chen & Bieber (1993) derived this anisotropy from the difference between count rates in a pair of NMs which are located near the north and south geographical poles observing intensities of GCRs arriving from the north and south pole orientations, respectively. They found a $\sim$ 10-year cycle variation in this component anisotropy which implied the radial density gradient (G_r) changing in a correlation with the solar activity, while they found no significant difference between G_rs in $A > 0$ and $A < 0$ epochs in a contradiction to the simple drift model prediction. Derivation of the NS anisotropy, however, have been difficult because the difference between only two detector's count rates is easily affected by instrumental variations of each detector such as the gain change.

1.3 Research object

The space weather or the space climate has been studied using only the spacecraft observation by many previous works. An in situ (or a single point) observation with spacecraft, however, can give the information only of a local spatial structure, in which the global magnetic structure such as the Parker spiral, IP-shock, MFR, or HCS is masked by small scale fluctuations of the solar wind plasma. There is also a remote sensing (or optical) observation probing the global spatial structure, but it observes only the solar surface or solar corona and cannot measure the interplanetary space. In this thesis, I present results of analyses on the space weather or space climate using a worldwide network of the cosmic ray detectors, the Global Muon Detector Network (GMDN). The GCR observation can make a major contribution to the space weather study because the solar modulation of GCRs is governed by a global magnetic structure over the scale comparable to the Larmor radius ($\sim$ 0.3 AU for $\sim$ 60 GV GCR in $\sim$ 5 nT magnetic field) as practically demonstrated by Kuwabara et al. (2004, 2009) and Fushishita et al. (2010b). It is also noted that the heliospheric magnetic field contributes to GCR modulation as an integration because GCRs pass the whole heliosphere before approaching the earth, as typically demonstrated by the force-field solution in equation (14). This allows us to infer the average magnetic configuration in the whole heliosphere from the GCR observation.

The 3D vector of the first order anisotropy corrected for the solar wind convection and the earth's orbital motion around the sun represents a GCR flow proportional to the spatial density gradient of GCRs as seen in equation (24). We can thus derive the density gradient from the observed 3D anisotropy based on Parker's transport equation. While the scalar density reflects only the information at the observation point, the density gradient vector allows us to infer the 3D spatial distribution of GCRs. In most of former works, however, the diurnal anisotropy and the NS anisotropy were studied separately using a single NM or muon detector (MD) because the two anisotropy components are derived by quite different analysis methods and/or different detectors. Only a worldwide detector network viewing various directions in space, such as the GMDN, can derive the 3D anisotropy simultaneously and separately from the density variation with a sufficient temporal resolution even for the short-term variation, such as the FD.

In Section 2, I describe a theoretical background of the MD data analysis and the analysis method of the GMDN. In Section 3, I deduce the GCR density distribution behind IP-shocks using the GMDN. In former analyses of the IP-shock events observed with the GMDN, the GCR density and density gradient have been used to analyze a geometry of the GCR depleted region in each individual FD (Munakata et al., 2003, 2006; Kuwabara et al., 2004, 2009; Rockenbach

et al., 2014). I perform, on the other hand, superposed epoch analyses of the GCR density and gradient derived from observations with the GMDN for 45 IP-shock events and analyze the average spatial distribution of GCR density behind the IP-shock. The solar cycle variation of the global density distribution in the heliosphere during a period from 1992 to 2013 is also deduced using the GMDN in Section 4. I also describe the traditional analysis method and compare the NS anisotropies derived by the GMDN and traditional method. After confirming the consistency between anisotropies observed with the GMDN and a single MD at Nagoya, I expand the period of analysis back to 1970's by combining the diurnal and NS anisotropies observed with a single MD at Nagoya. In Sections 3 and 4, the rigidity dependences of the GCR depression behind IP-shock and the solar cycle variation of GCRs are also studied by comparing observations with the MD and NM. I present the summary and conclusion of this thesis in Section 5.

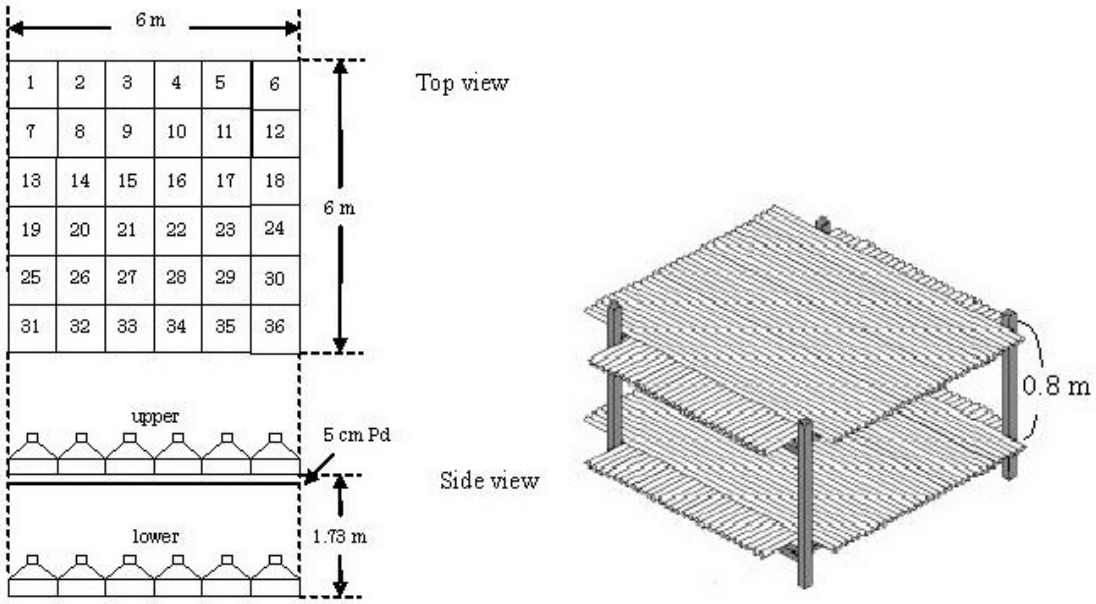

Figure 4: Schematic views of (left) the scintillator-type MD and (right) the PRC-type MD at Nagoya and Kuwait station, respectively (http://cosray.shinshu-u.ac.jp/crest).

2 Observation and data analysis

2.1 Muon detector (MD) and modeling the muon intensity

The MDs used in this thesis consist of two (upper and lower) horizontal layers of plastic scintillators or proportional counter (PRC) tubes, respectively, and a 5 cm layer of lead is located among or above them to absorb the soft component of the secondary cosmic rays. Each horizontal layer of the scintillator-type MD (left of Fgiure 4) comprises an array of 1 m $\times$ 1 m plastic scintillators, each viewed by a photomultiplier tube. Each PRC tube in the PRC-type MD (right of Fgiure 4) is a 5 m long cylinder with a 10 cm diameter and each layer of the PRC-type MD consists of a pair of PRC tube arrays, X- and Y-layers. In the X-layer, axes of the PRC tubes are aligned north-south (Y) direction to determine the east-west (X) position of the muon path, while the PRC tubes are aligned X direction in the Y-layer to determine the Y position. The upper and lower layers are vertically separated by 1.73 m in the scintillator-type MD and 0.8 m in the PRC-type MD, respectively, to determine a incident direction of a muon from positions of the unit detectors outputting a signal of muon detection. A recording system in the scintillator-type or PRC-type MD is triggered by the twofold or fourfold coincidence of pulses from all layers, respectively, and counts a number of muons for each directional channel.

From a numerical calculation of the cosmic ray propagation in the atmosphere, Murakami et al. (1979) derived a response function ($R(P, \Theta, d, E_\mu)$) of the atmospheric muon intensity to the isotropic component of the primary cosmic rays. $R(P, \Theta, d, E_\mu)$ is a function for the primary cosmic ray rigidity P, zenith angle Θ of the muon incident angle in a polar coordinate system (Θ, Φ) fixed on the detector with the z-axis corresponding to the vertical direction, atmospheric depth d, and threshold energy E_μ of muons. The average number of muons produced by primary cosmic rays with rigidity P and recorded by the j-th directional channel of the i-th station is expressed as

$$\langle n_{i,j}(P) \rangle = \int_{S_{i,j}} \int_{\Omega_{i,j}} g_i(P, \Theta, \Phi) R(P, \Theta, d, E_\mu) d\Omega dS \tag{34}$$

where $S_{i,j}$ and $\Omega_{i,j}$ are the effective area and the effective solid angle of the j-th directional channel. In this calculation, I set an element of the effective area, dS, as a 10 cm $\times$ 10 cm square area. An element of the solid angle multiplied by an element of the effective area, $d\Omega dS$ is given

as

$$(d\Omega dS)_{lu} = \frac{dS_l dS_u \cos^4\Theta_{lu}}{h_i^2} \tag{35}$$

where Θ_{lu} is a zenith angle of the viewing direction from an element dS_l in the lower layer to an element dS_u in the upper layer of the detector, and h_i is a vertical interval between the lower and upper layers of the i-th detector. The integral in equation (34) is carried out by summing up the integrand for all $(d\Omega dS)_{lu}$s in the j-th directional channel of the i-th detector. The atmospheric depth ($d = d_i$) is calculated from the altitude of the i-th detector and the muon threshold energy E_μ depends on the column density of the lead layer along the path of muons, i.e. a function $(E_\mu(\Theta))$ for Θ. $g_i(P,\Theta,\Phi)$ is defined as

$$\begin{aligned} g_i(P,\Theta,\Phi) &= 0 \text{ for } P < P_{ci}(\Theta,\Phi) \\ &= 1 \text{ for } P \geq P_{ci}(\Theta,\Phi) \end{aligned} \tag{36}$$

where $P_{ci}(\Theta,\Phi)$ is a geomagnetic cut off rigidity of primary cosmic rays below which $\langle n_{i,j}(P)\rangle$ is insignificant. $P_{ci}(\Theta,\Phi)$ is a function for (Θ,Φ) and the geographic location of the i-th detector and calculated using a particle trajectory code (Lin et al., 1995) in the geomagnetic field. From equation (34), we can derive the average number of muons produced by primary cosmic rays in all rigidity range, as

$$\langle N_{i,j}\rangle = \int_0^\infty \langle n_{i,j}(P)\rangle\, dP = \int_0^\infty \int_{S_{i,j}} \int_{\Omega_{i,j}} g_i(P,\Theta,\Phi) R(P,\Theta,d,E_\mu) d\Omega dS dP. \tag{37}$$

The median primary rigidity $P_{mi,j}$ of the j-directional channel of the i-th detector is defined as

$$\frac{1}{2}\langle N_{i,j}\rangle = \int_0^{P_{mi,j}} \langle n_{i,j}(P)\rangle\, dP. \tag{38}$$

From equation (16), ratio of the cosmic ray intensity $J(P,\theta,\phi)$ to the isotropic component, $J(P) = Y_0(P)$, is expressed as

$$\begin{aligned} \frac{J(P,\theta,\phi)}{J(P)} &= \frac{\sum_{n=0}^\infty Y_n(P,\theta,\phi)}{Y_0(P)} \\ &= \sum_{n=0}^\infty \sum_{m=0}^n \left\{ \frac{F_n^{mc}(P)}{F_0^{0c}(P)} \cos m\phi + \frac{F_n^{ms}(P)}{F_0^{0c}(P)} \sin m\phi \right\} P_n^m(\cos\theta). \end{aligned} \tag{39}$$

It is noted that the magnitude of the cosmic ray momentum, p, is replaced with the cosmic ray rigidity P and the angle (θ,ϕ) is redefined to represent the incident angle of primary cosmic rays while it represented the direction of $\boldsymbol{p}$ in equation (16), opposite to the incident angle. From equations (34) and (39), the number of muons including the anisotropic component is written as

$$\begin{aligned} n_{i,j}(P) &= \int_{S_{i,j}} \int_{\Omega_{i,j}} g_i(P,\Theta,\Phi) R(P,\Theta,d,E_\mu) \frac{J(P,\theta,\phi)}{J(P)} d\Omega dS \\ &= \sum_{n=0}^\infty \sum_{m=0}^n \int_{S_{i,j}} \int_{\Omega_{i,j}} g_i(P,\Theta,\Phi) R(P,\Theta,d,E_\mu) G_n(P) \cdot \\ &\qquad \{\eta_n^{mc} \cos m\phi + \eta_n^{ms} \sin m\phi\} P_n^m(\cos\theta) d\Omega dS \end{aligned} \tag{40}$$

where

$$G_n(P) \begin{pmatrix} \eta_n^{mc} \\ \eta_n^{ms} \end{pmatrix} = \begin{pmatrix} F_n^{mc}(P)/F_0^{0c}(P) \\ F_n^{ms}(P)/F_0^{0c}(P) \end{pmatrix} \tag{41}$$

and $G_n(P)$ represents a rigidity spectrum of the n-th harmonics. The incident angles θ and ϕ are defined in the local geographical (GEO) coordinate system and related to P, Θ, and Φ as

$$\theta(P,\Theta,\Phi) = \theta_i^{\rm or}(P,\Theta,\Phi) \tag{42}$$

$$\phi(P,\Theta,\Phi) = \phi_i^{\rm or}(P,\Theta,\Phi) - \phi_i^{\rm st} + \omega t_i \tag{43}$$

where $\phi_i^{\rm st}$ is the geographic longitude of the i-th station, t_i is the local solar time in hour at the station i, and $\omega = \pi/12$. The GEO coordinate system is defined as the z-axis is directed toward geographic north pole, the x-axis is in the equatorial plane pointing toward the mid-night (00:00 local solar time) direction, and the y-axis completes the right-handed coordinate set. Angles $\theta_i^{\rm or}(P,\Theta,\Phi)$ and $\phi_i^{\rm or}(P,\Theta,\Phi)$ are the geographic co-latitude and longitude of the asymptotic direction of primary cosmic rays with rigidity P before entering the earth's magnetosphere, respectively, and calculated using the particle trajectory code as well as $P_{ci}(\Theta,\Phi)$.

I introduce differential coupling coefficients (Nagashima, 1971; Fujimoto et al., 1984) defined as

$$\left(\begin{array}{c} dc^m_{ni,j}(P) \\ ds^m_{ni,j}(P) \end{array} \right) = \frac{dP}{\langle N_{i,j} \rangle} \int_{S_{i,j}} \int_{\Omega_{i,j}} g_i(P,\Theta,\Phi) R(P,\Theta,d,E_\mu) \cdot P^m_n(\cos\theta_i^{\rm or}) \left(\begin{array}{c} \cos m(\phi_i^{\rm or} - \phi_i^{\rm st}) \\ \sin m(\phi_i^{\rm or} - \phi_i^{\rm st}) \end{array} \right) d\Omega dS. \quad (44)$$

The differential coupling coefficients are determined by the detector properties, e.g. i and j, and the primary cosmic ray rigidity P. Using equations (42), (43), and (44), equation (40) is rewritten as

$$\begin{aligned} n_{i,j}(P)dP &= \langle N_{i,j} \rangle \sum_{n=0}^{\infty} \sum_{m=0}^{n} G_n(P) \cdot \\ &\quad \left[\eta_n^{mc} \left\{ dc^m_{ni,j}(P) \cos m\omega t_i - ds^m_{ni,j}(P) \sin m\omega t_i \right\} \right. \\ &\quad \left. + \eta_n^{ms} \left\{ ds^m_{ni,j}(P) \cos m\omega t_i + dc^m_{ni,j}(P) \sin m\omega t_i \right\} \right]. \end{aligned} \quad (45)$$

By integrating with P, number of muons is given as

$$\begin{aligned} N_{i,j} = \int_0^\infty n_{i,j}(P)dP &= \langle N_{i,j} \rangle \sum_{n=0}^{\infty} \sum_{m=0}^{n} \left\{ \eta_n^{mc} \left(c^m_{ni,j} \cos m\omega t_i - s^m_{ni,j} \sin m\omega t_i \right) \right. \\ &\quad \left. + \eta_n^{ms} \left(s^m_{ni,j} \cos m\omega t_i + c^m_{ni,j} \sin m\omega t_i \right) \right\} \end{aligned} \quad (46)$$

where

$$\left(\begin{array}{c} c^m_{ni,j} \\ s^m_{ni,j} \end{array} \right) = \int_{P=0}^{\infty} G_n(P) \left(\begin{array}{c} dc^m_{ni,j}(P) \\ ds^m_{ni,j}(P) \end{array} \right) \quad (47)$$

are constants called the coupling coefficients.

In the case that the anisotropy is expressed only in terms of the first order harmonics, the fractional deviation of the muon number is given as

$$\begin{aligned} I^{\rm fit}_{i,j}(t) = \frac{N_{i,j}(t)}{\langle N_{i,j} \rangle} &= I_0(t) c^0_{0i,j} + \xi_x^{\rm GEO}(t) \left(c^1_{1i,j} \cos\omega t_i - s^1_{1i,j} \sin\omega t_i \right) + \\ &\quad \xi_y^{\rm GEO}(t) \left(s^1_{1i,j} \cos\omega t_i + c^1_{1i,j} \sin\omega t_i \right) + \xi_z^{\rm GEO}(t) c^0_{1i,j} \end{aligned} \quad (48)$$

where t is an universal time and ωt_i is derived as

$$\omega t_i = \omega t + \phi_i^{\rm st}. \quad (49)$$

$I_0(t) = \eta_0^{0c}(t)$ represents the density variation and

$$\left(\xi_x^{\rm GEO}(t), \xi_y^{\rm GEO}(t), \xi_z^{\rm GEO}(t) \right) = \left(\eta_1^{1c}(t), \eta_1^{1s}(t), \eta_1^{0c}(t) \right) \quad (50)$$

represents the first order anisotropy vector $\boldsymbol{\xi}$ in GEO coordinate system. The rigidity spectrum of the first order anisotropy is assumed as

$$\begin{aligned} G_1(P) = G(P) &= 1 \text{ for } P \le P_u \\ &= 0 \text{ for } P > P_u \end{aligned} \quad (51)$$

where P_u is an upper limiting rigidity of the anisotropy set at 10^5 GV, far above the most sensitive rigidity of the muon detectors, as in Kuwabara et al. (2004, 2009); Okazaki et al. (2008) and Fushishita et al. (2010a,b).

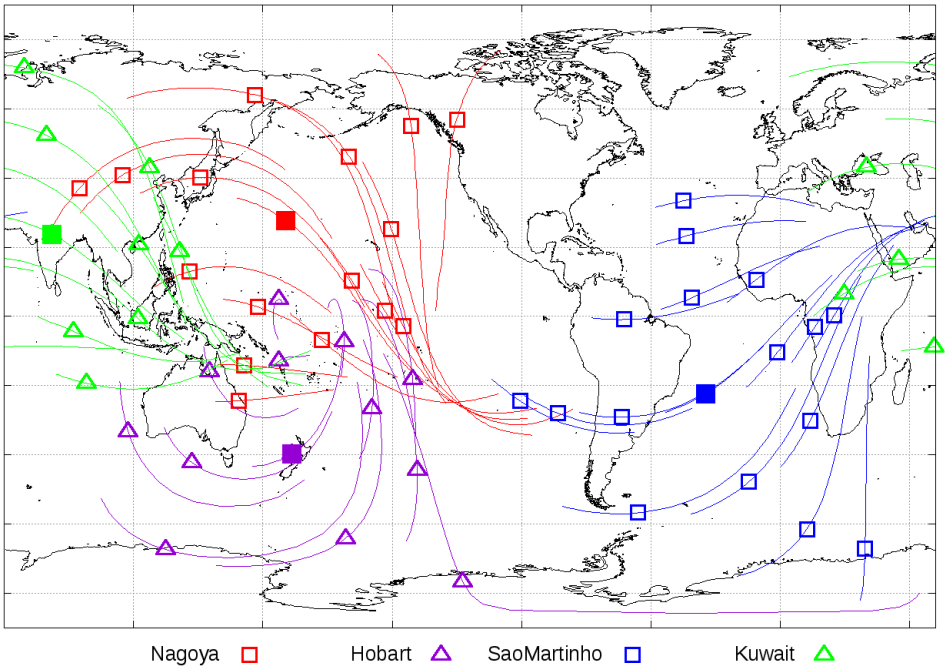

Figure 5: The asymptotic directions of all directional channels of the GMDN. A solid character represents the vertical channel of each detector. A Line is the direction of primary cosmic rays with rigidities in central 80 % ($10 - 90$ %) response of each channel.

2.2 The Global Muon Detector Network (GMDN)

The GMDN[1] started operation measuring the three dimensional (3D) anisotropy on an hourly basis with two-hemisphere observations using a pair of MDs at Nagoya (Japan) and Hobart (Australia) in 1992. In 2001, another small detector at São Martinho da Serra (Brazil) was added to the network to fill a gap in directional coverage over the Atlantic ocean. The current GMDN consisting of four multi-directional muon detectors was completed in 2006 by expanding the São Martinho da Serra MD and installing a new detector in Kuwait. Figure 5 maps the asymptotic directions of all directional channels available in the GMDN. For more detail description of the GMDN, readers can refer to Okazaki et al. (2008).

I analyze a percent deviation, $I_{i,j}(t)$, of the pressure corrected hourly count rate of muons in the j-th directional channel of the i-th detector in the GMDN at the universal time t. GCR density $I_0(t)$ and three components ($\xi_x^{\mathrm{GEO}}(t)$, $\xi_y^{\mathrm{GEO}}(t)$, $\xi_z^{\mathrm{GEO}}(t)$) of the first order anisotropy in the GEO coordinate system are derived on an hourly basis by best-fitting $I_{i,j}^{\mathrm{fit}}(t)$ in equation (48) to $I_{i,j}(t)$ (see Appendix A).

[1] http://cosray.shinshu-u.ac.jp/crest

3 Average spatial distribution of GCRs behind IP-shocks

3.1 Derivation of GCR density and density gradient

In this section, I derive the anisotropy ($\xi_x^{\rm GEO}(t)$, $\xi_y^{\rm GEO}(t)$, $\xi_z^{\rm GEO}(t)$) and the density $I_0(t)$ from the fractional deviation $I_{i,j}(t)$ of the pressure corrected muon count rate from the average over 27-days centered by the SSC onset, using the analysis method described in Appendix A. In order to remove longer-time density variations superposed on the short-term decreases in FDs, e.g. the 27-days cycle variations arising from the sun's rotation, I also take a fractional deviation of $I_0(t)$ in each SSC event from the average over 5-days from a day before the SSC onset for the superposition analysis in Section 3.4.

The GCR density variation free from the atmospheric temperature effect can be deduced from count rates recorded by polar neutron monitors (NMs), as

$$I_0^{\rm NM}(t) = \frac{I^{\rm Thule}(t) + I^{\rm McMurdo}(t)}{2} \tag{52}$$

where $I^{\rm Thule}(t)$ and $I^{\rm McMurdo}(t)$ are fractional deviations of the pressure corrected count rates in Thule and McMurdo NMs[2] in Greenland and Antarctica, respectively, from the 5-days average. $I_0^{\rm NM}(t)$ in equation (52) gives a good measure of the GCR density, also because it contains only minor effects of the diurnal and north-south anisotropies (Suda & Wada, 1981). By comparing $I_0(t)$ by the GMDN with $I_0^{\rm NM}(t)$ by NMs in Sections 3.3 and 3.4, I will confirm that my conclusions in this thesis are not seriously affected by the atmospheric temperature effect. Since the median rigidity of primary GCRs observed by NMs is $\sim$ 10 GV, while the median rigidity of GCRs observed by the GMDN is $\sim$ 60 GV, we can also analyze the rigidity dependence of the GCR density depression in FDs by comparing $I_0(t)$ with $I_0^{\rm NM}(t)$.

I correct the anisotropy vector for the solar wind convection and the Compton-Getting effect, using the solar wind velocity $\boldsymbol{V}_{\rm SW}$ in spacecraft data and the earth's orbital motion speed set at 30 km/s, as

$$\boldsymbol{\xi}^w(t) = \boldsymbol{\xi}(t) + \frac{2+\gamma}{c}\left(\boldsymbol{V}_{\rm SW}(t) - \boldsymbol{V}_E\right) \tag{53}$$

based on equation (26). Hourly solar wind velocity $\boldsymbol{V}_{\rm SW}(t)$ for my analysis is mainly given by the ACE level 2 data[3] and I also use the WIND spacecraft data[4] when there is a gap in the ACE data, after confirming consistency between two data sets before and after the data gap. The ACE and WIND data are lagged for 1 hour as a rough correction for the solar wind transit time between the spacecraft at L1 Lagrangian point and the earth. From equations (9) and (26), the corrected anisotropy $\boldsymbol{\xi}^w(t)$ is related to the parallel ($\boldsymbol{G}_\parallel(t)$) and perpendicular ($\boldsymbol{G}_\perp(t)$) density gradients, as

$$\boldsymbol{\xi}^w(t) = R_L(t)\left\{\alpha_\parallel \boldsymbol{G}_\parallel(t) + \alpha_\perp \boldsymbol{G}_\perp(t) - \frac{\boldsymbol{B}(t)}{B(t)} \times \boldsymbol{G}_\perp(t)\right\} \tag{54}$$

where $\alpha_\perp = \lambda_\perp(t)/R_L(t)$ is a dimensionless mean free path perpendicular to the IMF. From equation (54), the density gradient $\boldsymbol{G}(t)$ is given in terms of the anisotropy, as

$$\boldsymbol{G}(t) = \boldsymbol{G}_\parallel(t) + \boldsymbol{G}_\perp(t) = \frac{1}{R_L\alpha_\parallel}\boldsymbol{\xi}_\parallel^w + \frac{1}{R_L(1+\alpha_\perp^2)}\left(\alpha_\perp \boldsymbol{\xi}_\perp^w + \frac{\boldsymbol{B}}{B} \times \boldsymbol{\xi}_\perp^w\right) \tag{55}$$

where $\boldsymbol{\xi}_\parallel^w(t)$ and $\boldsymbol{\xi}_\perp^w(t)$ are components of $\boldsymbol{\xi}^w$ parallel and perpendicular to the IMF. The Larmor radius $R_L(t)$ is calculated as $R_L(t) = P/(cB(t))$ with P denoting the rigidity of GCR particle which I set at 60 GV for my analysis of the GMDN data, the representative median rigidity of primary GCRs observed with the GMDN. The IMF vector $\boldsymbol{B}(t)$ is given by the IMF vector in the ACE or WIND data lagged for 1 hour. Following theoretical calculations by Bieber et al. (2004), I assume in this thesis constant $\alpha_\parallel$ and $\alpha_\perp$ at $\alpha_\parallel = 7.2$ and $\alpha_\perp = 0.05\alpha_\parallel$. This

[2] http://neutronm.bartol.udel.edu/
[3] http://www.srl.caltech.edu/ACE/ASC/
[4] http://wind.nasa.gov/data.php

assumption is also used by Okazaki et al. (2008) and Fushishita et al. (2010a) and proved to result in reasonable GCR density distribution in the vicinity of the interplanetary disturbance. Moreover, Fushishita et al. (2010b) deduced the parallel mean free path $\lambda_{\parallel}$ from the observed "decay length" of the loss-cone precursor of an IP-shock event and obtained $\lambda_{\parallel}$ comparable to my assumption of $\lambda_{\parallel} = 7.2R_L$.

3.2 Identification of IP-shocks associated with solar eruptions

I infer spatial distribution of GCRs behind IP-shock, by analyzing temporal variations of the GCR density and its spatial gradient in IP-shock events, each identified with a source location on the sun. IP-shocks are known to cause the geomagnetic storm sudden commencements (SSCs) in general (Smith, 1983; Wang et al., 2006). I identify IP-shock arrivals with SSCs listed by the German Research Centre for Geosciences (GFZ) and extract 79 CME-associated shocks (CME events) from 214 SSCs in a period between 2006 and 2014, referring to the space weather news (SW news) of the National Institute of Technology (NIT), Kagoshima College[5] on the date of each SSC occurrence. The SW news reports current status of the solar surface and interplanetary space each day, monitoring SDO, SOHO, ACE, and GOES spacecraft data, geomagnetic indices, and solar wind prediction by the Space Weather Prediction Center (SWPC), NOAA. It estimates not only the interplanetary origin of each geomagnetic storm but also the associated solar event, allowing us to associate a CME eruption on the sun with each IP-shock event recorded at the earth. For the heliographic location of the CME eruption on the solar surface, I use the location of the associated H-α flare or filament disappearance in the solar event list by SWPC.

Table 1 lists 79 CME events collected in this manner. All the SSC onsets in the CME events coincide with discontinuous increases in solar wind speed, magnetic field magnitude or proton density in the ACE or WIND data, ensuring that the SSC can be used as an indicator of the IP-shock arrival in CME event. Solar event associations of 26 events in this table are also included in the Richardson/Cane Near-Earth Interplanetary CMEs list[6] (Cane & Richardson, 2003; Richardson & Cane, 2010). From further analysis in this thesis, I exclude 12 events noted with † or ‡ in Table 1 which lack the GMDN data or the location of the CME erutpion in the SWPC data and use remaining 67 events.

Figure 6a displays heliographic locations of 67 CME eruptions on the solar surface. The latitudinal (λ) distribution of CME eruptions is limited in the low- and mid-latitude zone between 0°-40° above and below the heliographic equator, as shown by a gray filled histogram in Figure 6c. The longitudinal (ϕ) distribution of CME eruptions, on the other hand, spreads over a wide range as shown by a gray filled histogram in Figure 6b, allowing us to analyze the longitudinal distribution of GCRs behind IP-shock. It is also seen in Figure 6b that the maximum number of events occurs around the longitudinal center as reported in previous studies (e.g. Gopalswamy et al., 2007). Each red number in Figure 6a indicates a number of CME eruptions in each heliographic region on the sun enclosed by solid lines denoting equator ($\lambda = 0°$) and 5 meridians ($\phi = -90°, -45°, 0°, 45°, +90°$).

Out of the 67 CME events, I use for my superposition analyses only 45 events associated with CME eruptions in the central region ($-45° \leq \phi \leq +45°$) on the sun (I call these events as "central events"), because other 22 events associated with CME eruptions outside this region are known to show different properties when observed at the earth (Gopalswamy et al., 2007). In subsections 3.4.2 and 3.4.3, I will perform superposition analyses for 22 "E-events" and 23 "W-events" of the central events associated with CME eruptions in eastern ($-45° \leq \phi < 0°$) and western ($0° \leq \phi \leq +45°$) regions on the sun, respectively. Blue and red histograms in Figure 6b represent ϕ distributions in the E- and W-events. In subsection 3.4.4, on the other hand, I will classify the central events into 26 "N-events" associated with northern ($\lambda > 0°$) CME eruptions and 19 "S-events" associated with southern ($\lambda < 0°$) CME eruptions, as represented by red and blue histograms in Figure 6c.

[5] http://www.kagoshima-ct.ac.jp/
[6] http://www.srl.caltech.edu/ACE/ASC/DATA/level3/icmetable2.htm

Table 1: List of SSC events associated with solar eruptions (Kozai et al., 2016)

	SSC onset		FD (GMDN)[a]			FD (NMs)[b]			Associated event on the sun				
No.	date	time	date	time	mag. [%]	date	time	mag. [%]	type[c]	date[d]	time[d]	X-ray class[d]	heliographic lat. & long.[d]
†1	2006/01/01	14:05	–	–	–	2006/01/01	19:30	0.2	FLA	2005/12/29	21:11	C1.1	N11E17
2	2006/07/09	21:36	2006/07/12	04:30	1.29	2006/07/11	08:30	4.0	FLA	2006/07/06	08:23	M2.5	S11W32
3	2006/08/19	11:30	2006/08/20	10:30	0.59	2006/08/20	10:30	2.9	FLA	2006/08/16	16:17	C3.6	S14W13*
4	2006/12/08	04:35	2006/12/08	21:30	0.38	2006/12/11	03:30	3.4	FLA	2006/12/05	10:38	X9.0	S07E79
5	2006/12/14	14:14	2006/12/15	02:30	2.34	2006/12/15	00:30	7.4	FLA	2006/12/13	02:34	X3.4	S06W24
6	2006/12/16	17:55	2006/12/16	23:30	0.06	2006/12/16	23:30	0.4	FLA	2006/12/14	22:17	X1.5	S06W46
7	2007/05/21	23:20	2007/05/22	11:30	0.51	2007/05/22	14:30	1.6	DSF	2007/05/19	12:31	B9.5	N07W06
‡8	2007/11/19	18:11	2007/11/20	01:30	0.31	2007/11/20	04:30	2.5	–	–	–	–	–
9	2008/04/30	15:57	2008/04/30	21:30	0.11	2008/05/01	19:30	0.9	FLA	2008/04/26	14:00	B3.8	N08E09
‡10	2008/12/16	11:59	2008/12/17	13:30	0.45	2008/12/17	13:30	2.9	DSF	–	–	–	–
†‡11	2009/10/22	00:17	–	–	–	2009/10/23	01:30	1.4	–	–	–	–	–
12	2010/04/05	08:26	2010/04/06	13:30	0.75	2010/04/06	02:30	2.6	FLA	2010/04/03	00:24	B7.4	S25W00
13	2010/04/11	13:04	2010/04/12	03:30	0.32	2010/04/12	07:30	1.4	FLA	2010/04/08	03:25	B3.7	N24E12*
‡14	2010/05/28	02:58	2010/05/29	08:30	0.47	2010/05/30	04:30	1.9	FLA	2010/05/24	14:46	B1.1	–
15	2010/08/03	17:40	2010/08/04	10:30	0.76	2010/08/04	05:30	3.4	FLA	2010/08/01	08:26	C3.2	N20E36
16	2010/12/19	21:32	2010/12/20	02:30	0.18	2010/12/22	10:30	0.7	DSF	2010/12/16	04:27	B7.4	N18E27*
17	2011/02/18	01:30	2011/02/18	11:30	1.37	2011/02/18	12:30	4.6	FLA	2011/02/15	01:56	X2.2	S21W15*
18	2011/03/10	06:32	2011/03/12	14:30	0.73	2011/03/11	08:30	2.7	FLA	2011/03/07	20:12	M3.7	N24W58*
19	2011/04/06	09:33	2011/04/08	22:30	1.23	2011/04/08	04:30	1.6	FLA	2011/04/03	05:19	C1.2	N15W15*
20	2011/04/18	06:52	2011/04/18	07:30	0.03	2011/04/19	09:30	0.6	FLA	2011/04/15	17:11	M1.3	N14W19
21	2011/06/04	20:44	2011/06/05	09:30	1.04	2011/06/05	05:30	3.2	FLA	2011/06/01	16:56	C4.1	S20E20
22	2011/06/10	08:47	2011/06/10	23:30	0.97	2011/06/10	18:30	1.8	FLA	2011/06/07	06:29	M2.5	S21W54
23	2011/06/17	02:39	2011/06/17	13:30	1.18	2011/06/18	02:30	2.9	DSF	2011/06/14	21:42	M1.3	N15E77
24	2011/07/11	08:51	2011/07/11	16:30	1.20	2011/07/12	02:30	3.1	FLA	2011/07/09	00:48	–	S18E11*
25	2011/08/05	17:51	2011/08/06	22:30	1.07	2011/08/06	13:30	4.4	FLA	2011/08/03	13:50	M6.0	N16W30
26	2011/09/17	03:43	2011/09/18	13:30	0.46	2011/09/18	10:30	2.3	FLA	2011/09/13	23:33	–	N23W03
27	2011/09/25	11:45	2011/09/26	01:30	0.41	2011/09/26	02:30	1.4	FLA	2011/09/22	10:57	X1.4	N13E78
28	2011/09/26	12:35	2011/09/28	11:30	0.99	2011/09/27	06:30	4.5	FLA	2011/09/24	13:20	M7.1	N13E51
29	2011/10/05	07:36	2011/10/05	18:30	0.85	2011/10/05	21:30	2.4	FLA	2011/10/02	00:49	M3.9	N09W12
30	2011/10/24	18:31	2011/10/25	09:30	1.17	2011/10/25	06:30	5.9	FLA	2011/10/22	10:18	M1.3	N25W77
31	2011/11/12	05:59	2011/11/13	04:30	0.40	2011/11/13	15:30	1.7	FLA	2011/11/09	13:35	M1.1	N18E26*

Table continued

	SSC onset		FD (GMDN)[a]			FD (NMs)[b]			Associated event on the sun				
No.	date	time	date	time	mag. [%]	date	time	mag. [%]	type[c]	date[d]	time[d]	X-ray class[d]	heliographic lat. & long.[d]
32	2011/11/28	21:50	2011/11/29	14:30	0.40	2011/11/30	10:30	2.4	FLA	2011/11/26	07:10	C1.2	N08W39*
33	2011/12/18	19:03	2011/12/22	11:30	0.63	2011/12/22	13:30	1.8	FLA	2011/12/13	23:34	C4.8	S19W84
34	2012/01/22	06:12	2012/01/22	23:30	0.76	2012/01/23	10:30	3.4	FLA	2012/01/16	04:44	C6.5	N27E61*
35	2012/01/24	15:03	2012/01/24	16:30	0.75	2012/01/24	17:30	3.3	FLA	2012/01/23	04:04	M8.7	N28W21
36	2012/01/30	16:24	2012/02/01	12:30	0.69	2012/02/01	07:30	3.4	FLA	2012/01/27	18:51	X1.7	N27W71
37	2012/02/26	21:40	2012/02/29	12:30	1.90	2012/02/28	14:30	3.3	DSF	2012/02/24	02:25	–	N32E38
38	2012/03/07	04:20	2012/03/08	10:30	0.82	2012/03/08	10:30	2.8	FLA	2012/03/05	03:48	X1.1	N17E52
39	2012/03/08	11:03	2012/03/09	00:30	1.98	2012/03/09	07:30	9.8	FLA	2012/03/07	00:17	X5.4	N17E27
40	2012/03/12	09:15	2012/03/13	01:30	1.03	2012/03/13	04:30	4.8	FLA	2012/03/09	03:53	M6.3	N17W01*
41	2012/03/15	13:07	2012/03/15	23:30	0.28	2012/03/15	18:30	1.1	FLA	2012/03/13	17:41	M7.9	N18W61*
‡42	2012/04/23	03:20	2012/04/26	11:30	1.27	2012/04/26	05:30	3.4	–	2012/04/19	15:15	C1.8	–
43	2012/05/21	19:37	2012/05/22	20:30	0.09	2012/05/22	05:30	0.7	FLA	2012/05/17	01:34	M5.1	N11W76
44	2012/06/16	20:20	2012/06/17	05:30	1.15	2012/06/17	04:30	4.5	FLA	2012/06/13	13:41	M1.2	S16E18
45	2012/07/14	18:09	2012/07/15	13:30	1.26	2012/07/15	18:30	5.9	FLA	2012/07/12	16:25	X1.4	S15W01
46	2012/08/02	10:50	2012/08/02	15:30	0.50	2012/08/03	08:30	0.3	FLA	2012/07/28	20:58	M6.1	S25E54
47	2012/08/16	13:15	2012/08/16	14:30	0.02	2012/08/17	06:30	0.9	FLA	2012/08/14	11:37	C1.1	N20W12*
48	2012/09/03	12:13	2012/09/05	10:30	1.48	2012/09/05	10:30	4.6	FLA	2012/08/31	20:43	C8.4	S19E42
49	2012/09/30	23:05	2012/10/02	07:30	1.40	2012/10/02	05:30	1.8	FLA	2012/09/27	23:48	C3.7	N06W34
50	2012/10/08	05:16	2012/10/10	03:30	0.20	2012/10/10	14:30	1.9	FLA	2012/10/05	07:30	B7.8	S22W30*
‡51	2012/10/31	15:39	2012/11/01	15:30	0.25	2012/11/01	07:30	1.6	DSF	–	–	–	–
‡52	2012/11/12	23:12	2012/11/13	18:30	0.77	2012/11/13	17:30	3.3	DSF	2012/11/09	16:06	–	–
‡53	2012/11/23	21:52	2012/11/26	05:30	1.00	2012/11/24	22:30	3.2	FLA	2012/11/20	12:41	M1.7	–
54	2013/02/16	12:09	2013/02/18	13:30	1.37	2013/02/18	06:30	2.4	DSF	2013/02/13	03:00	–	S28W54
55	2013/03/17	06:00	2013/03/19	12:30	1.23	2013/03/18	03:30	4.4	FLA	2013/03/15	06:37	M1.1	N11E12
56	2013/04/13	22:55	2013/04/16	11:30	1.13	2013/04/15	13:30	3.4	FLA	2013/04/11	07:10	M6.5	N09E12
57	2013/04/30	09:49	2013/04/30	21:30	0.64	2013/05/01	09:30	2.8	DSF	2013/04/26	09:25	–	S38W05
58	2013/05/18	01:10	2013/05/18	19:30	0.57	2013/05/18	22:30	1.7	FLA	2013/05/15	01:40	X1.2	N12E64
59	2013/05/19	23:08	2013/05/20	10:30	0.25	2013/05/21	00:30	1.1	FLA	2013/05/17	08:54	M3.2	N12E31
60	2013/05/24	18:10	2013/05/26	04:30	0.66	2013/05/26	06:30	3.0	FLA	2013/05/22	13:22	M5.0	N15W70
‡61	2013/05/31	16:18	2013/06/04	00:30	0.49	2013/06/01	01:30	1.4	–	–	–	–	–
62	2013/06/27	14:38	2013/06/28	08:30	0.76	2013/06/28	05:30	2.5	FLA	2013/06/23	20:53	M2.9	S15E62
‡63	2013/10/02	01:55	2013/10/02	07:30	0.88	2013/10/02	07:30	3.1	DSF	2013/09/29	23:39	C1.2	–
‡64	2013/12/13	13:22	2013/12/14	11:30	0.38	2013/12/14	13:30	1.0	–	–	–	–	–

Table continued

	SSC onset		FD (GMDN)[a]			FD (NMs)[b]			Associated event on the sun				
No.	date	time	date	time	mag. [%]	date	time	mag. [%]	type[c]	date[d]	time[d]	X-ray class[d]	heliographic lat. & long.[d]
65	2014/02/07	17:05	2014/02/07	21:30	0.14	2014/02/08	16:30	0.7	FLA	2014/02/04	03:58	M5.2	S14W06
66	2014/02/20	03:20	2014/02/20	18:30	0.49	2014/02/20	18:30	2.9	DSF	2014/02/18	06:14	–	S31E54
67	2014/02/27	16:50	2014/02/28	23:30	0.94	2014/02/28	17:30	3.9	FLA	2014/02/25	00:47	X4.9	S12E82
68	2014/03/25	20:04	2014/03/26	19:30	0.22	2014/03/26	16:30	1.4	FLA	2014/03/23	03:23	C5.0	S12E40
69	2014/04/20	10:56	2014/04/20	19:30	0.58	2014/04/20	23:30	1.2	FLA	2014/04/18	13:03	M7.3	S15W36*
70	2014/04/29	20:26	2014/04/30	00:30	0.05	2014/04/30	05:30	0.9	FLA	2014/04/25	00:42	X1.3	S15W90
71	2014/06/23	23:08	2014/06/24	11:30	0.05	2014/06/24	15:30	0.3	DSF	2014/06/19	09:15	–	S01E15
72	2014/07/03	00:42	2014/07/03	07:30	0.11	2014/07/03	01:30	0.1	FLA	2014/06/28	08:58	C1.1	N09E05
73	2014/08/19	06:57	2014/08/19	20:30	0.14	2014/08/19	23:30	1.5	DSF	2014/08/15	17:09	–	N26E18
74	2014/09/11	23:45	2014/09/12	09:30	0.75	2014/09/12	08:30	2.0	FLA	2014/09/09	00:38	M4.5	N12E29
75	2014/09/12	15:53	2014/09/12	20:30	1.09	2014/09/13	01:30	5.1	FLA	2014/09/10	17:33	X1.6	N14E02
76	2014/11/10	02:21	2014/11/10	13:30	0.75	2014/11/10	19:30	3.6	FLA	2014/11/07	17:26	X1.6	N15E35*
77	2014/12/21	19:11	2014/12/22	12:30	1.82	2014/12/22	14:30	6.0	FLA	2014/12/17	04:42	M8.7	S20E09
78	2014/12/22	15:11	2014/12/23	10:30	0.69	2014/12/23	00:30	0.7	FLA	2014/12/20	00:26	X1.8	S21W24
79	2014/12/23	11:15	2014/12/23	11:30	1.01	2014/12/23	20:30	1.7	FLA	2014/12/21	12:17	M1.0	S11W28*

[a]The maximum density depression in FD observed with the GMDN together with its recorded date and time.
The maximum density depression in % is normalized to the 6 hours average of the GCR density prior to the SSC onset.
[b]The maximum density depression in FD observed with the NMs together with its recorded date and time.
[c]Type of the solar eruption specified from the SW news; FLA is flare, DSF is filament disappearance.
[d]Solar event properties given in the SWPC solar event list.
Listed date and time represent the timing of maximum intensity of the H-α or X-ray emissions,
while those indicate the start time of event for the filament disappearance.
†Excluded from the analysis in this thesis due to the lack of the GMDN data.
‡Excluded from the analysis in this paper because the heliographic location of the solar eruption could not be specified in this event.
∗Location of the solar eruption is specified from the SWPC Solar Region Summary report,
because the SWPC solar event list provides only the solar region number for this event.

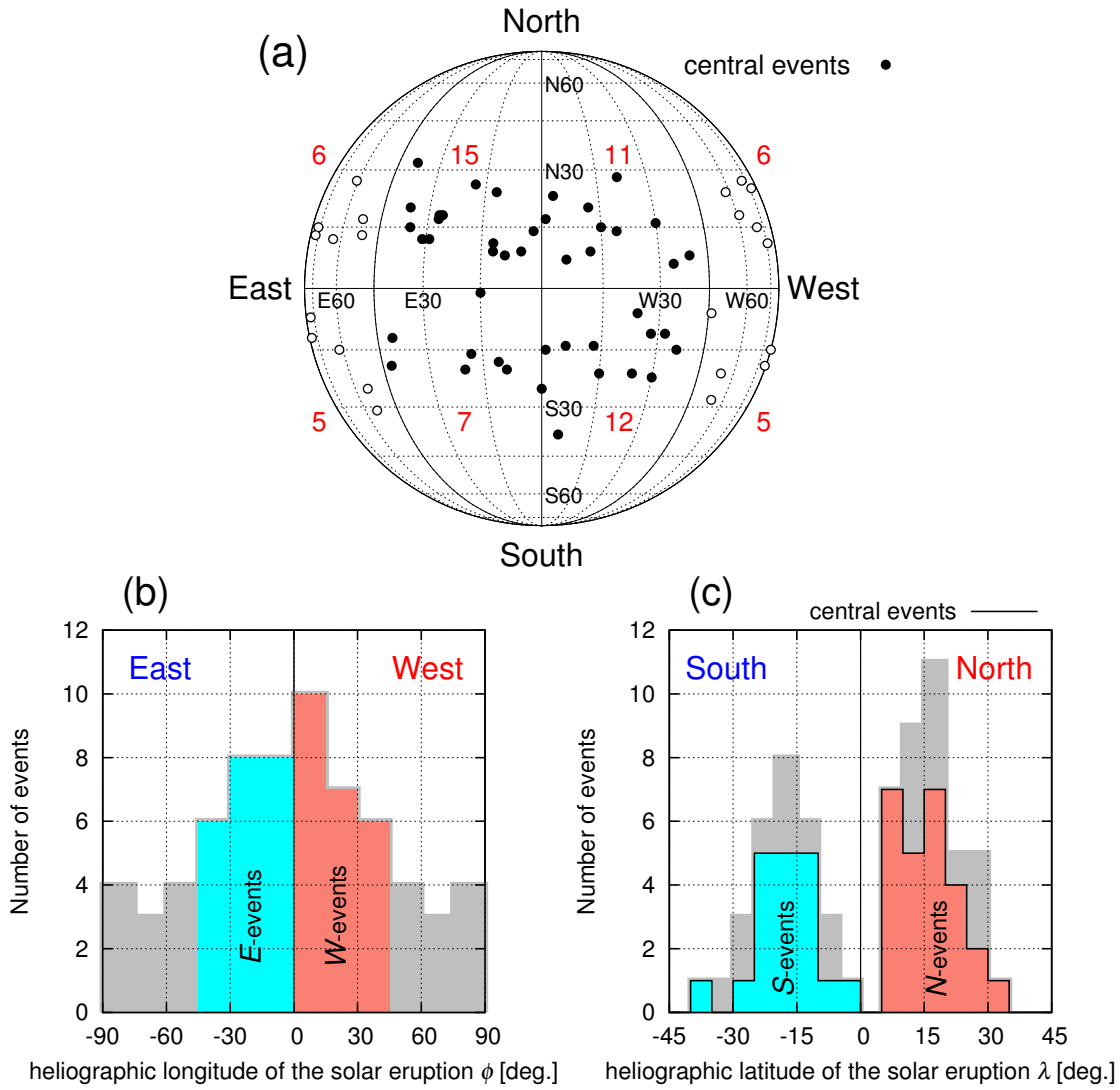

Figure 6: Heliographic locations of solar flares and filament disappearances associated with 67 events in Table 1. The top panel displays the locations plotted on the solar surface (a), while bottom panels display histograms of the heliographic longitude, ϕ (b) and latitude, λ (c) of the location. Black solid points in panel (a) indicate the "central events" in $-45° \leq \phi \leq +45°$. A red number in panel (a) indicates the event number in each region on the sun divided by black solid lines, equator line ($\lambda = 0°$) and 5 meridian lines ($\phi = -90°, -45°, 0°, +45°, +90°$). Blue and red histograms in panel (b) represent the E- and W-events while those in panel (c) are the S- and N-events, groups in the central events. For the definition of the E-, W-, N- and S-events, see the text. (Kozai et al., 2016)

3.3 Event samples

I first present some event samples in this Section, before I analyze the average spatial distribution of GCRs by superposing events.

3.3.1 December 14, 2006 SSC event

This SSC event is followed by a record intense geomagnetic storm with the maximum Kp index of +8. The associated CME occurred following an X3.4 solar flare on December 13, 02:34 UT at S06W24. A comprehensive view of this event is presented by Liu et al. (2008) based on spacecraft data, while Fushishita et al. (2010b) analyzed a precursory "loss-cone" anisotropy observed with the GMDN prior to this event recorded at the earth. I focus on the GCR density distribution observed after the SSC in the present thesis.

Figure 7 displays temporal variations of the solar wind data in panels (a) to (d), the GCR density I_0 observed with the GMDN (color shaded curve) and NMs (green curve) in panel (e) and three GSE components of the density gradient $\boldsymbol{G}$ derived from the GMDN data in panels (f) to (h), all during a time interval from 1 day before the SSC onset to 3 days after the SSC onset. The IMF sector polarity indicated by red and blue points in Figure 7a is designated referring to the hourly mean magnetic field $\boldsymbol{B}(t)$ observed in the GSE coordinate system, as *away* when $B_x < B_y$ and *toward* when $B_x > B_y$, as expected from the Parker's spiral magnetic field. The variance of the magnetic field, $\sigma_B^2(t)$ displayed by a green curve in Figure 7b is derived on an hourly basis as

$$\sigma_B^2(t) = \frac{1}{3 \times 60} \sum_{i=1}^{60} \left\{ \left(b_x^i(t) - B_x(t)\right)^2 + \left(b_y^i(t) - B_y(t)\right)^2 + \left(b_z^i(t) - B_z(t)\right)^2 \right\} \tag{56}$$

where $\boldsymbol{b}^i(t)$ $(i = 1, 2, \cdots, 60$ minute) is a minute average of the magnetic field in a temporal interval $t \sim t + 1$ hours. The GCR densities, $I_0(t)$ and $I_0^{\rm NM}(t)$ are normalized to the 6 hours average prior to the SSC onset.

As reported by Liu et al. (2008), the azimuthal angle ϕ_B of the magnetic field orientation in Figure 7c shows a monotonous rotation during one day after the end of December 14, indicating a Magnetic Flux Rope (MFR) passing the earth. G_x in Figure 7f shows a negative enhancement after the SSC onset until the end of the magnetic sheath region behind IP-shock, corresponding to the decreasing phase of the density in Figure 7e. This is consistent with a density minimum approaching the earth from the sunward direction ($x > 0$) and being observed as a negative enhancement of G_x. Following the sheath region, positive G_y and G_z in Figures 7g and 7h are clearly enhanced when the earth enters the minimum density region inside the magnetic flux rope (MFR), indicating that the density minimum passed the south-west of the earth ($y < 0$ and $z < 0$) after propagating radially outward from the CME eruption on the sun. According to Liu et al. (2008), the GSE latitude and longitude of the MFR axis orientation best-fitted to the spacecraft data are ~ 60 degree and ~ 270 degree in the GSE-coordinate, respectively, and the axis passed the west of the earth. The density gradient in Figure 7 is consistent with the GCR density minimum located on the MFR axis approaching and leaving the earth. Kuwabara et al. (2004, 2009) presented the detail analysis of the density gradient vector derived from the GMDN data and deduced the cylinder geometry of the GCR depleted region in CMEs.

I also note that the temporal variation of the GCR density, I_0, derived from the GMDN data in Figure 7e is in a good agreement with $I_0^{\rm NM}$ (green curve) derived from NM data which is free from the atmospheric temperature effect. This ensures that the GCR density is properly derived from the GMDN data in this event by my analysis method. Magnitude of the FD, on the other hand, is larger in $I_0^{\rm NM}$ derived from NM data than in I_0 derived from the GMDN data, indicating a soft rigidity spectrum of the density depression in FD.

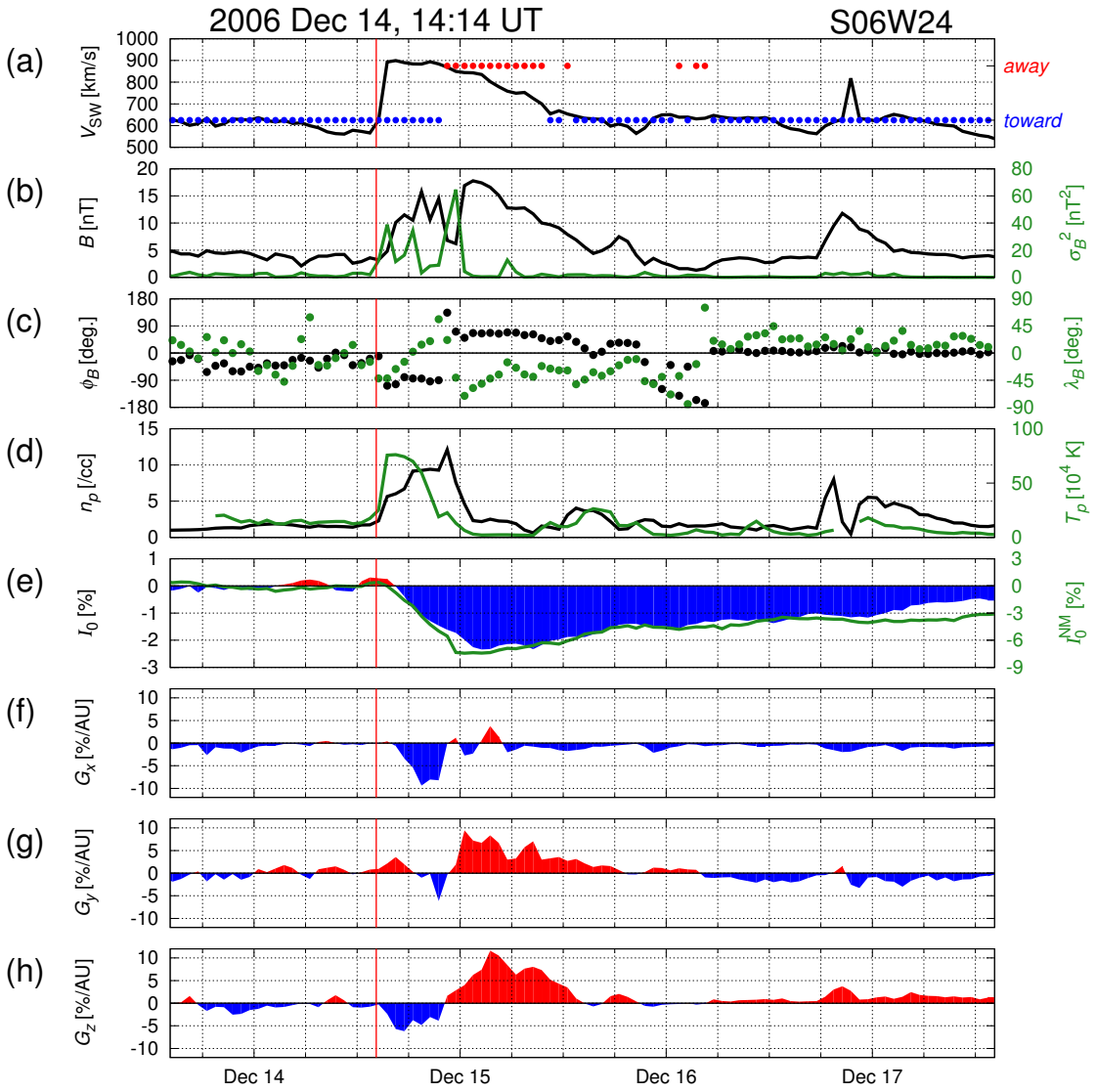

Figure 7: A sample event following the SSC on December 14, 2006 at 14:14 UT. The heliographic location of the solar eruption associated with this SSC event is indicated above the right top corner of this figure. Panels from the top to the bottom display (a) hourly values of the solar wind speed ($V_{\rm SW}$), (b) magnetic field magnitude (B) and variance (σ_B^2), (c) GSE longitude (ϕ_B) and latitude (λ_B) of the magnetic field orientation, (d) solar wind proton density (n_p) and temperature (T_p), (e) GCR density (I_0), and (f-h) GSE-x, y, z components of the GCR dnesity gradient ($\boldsymbol{G}$), each as a function of time on the horizontal axis. The solar wind parameters in panels (a-d) are measured by ACE or WIND spacecraft. The GCR parameters in panels (e-h) are derived from the GMDN data, except for the green curve in panel (e) which is derived from NM data and whose scale is shown on the right vertical axis. In panels (a-d), black and green curves or circles are plotted on the left and right vertical axes, respectively. Also the *away* and *toward* IMF sector polarities in each hour are respectively indicated by a red and blue solid circles in panel (a). The vertical red line in each panel indicates the SSC onset time. (Kozai et al., 2016)

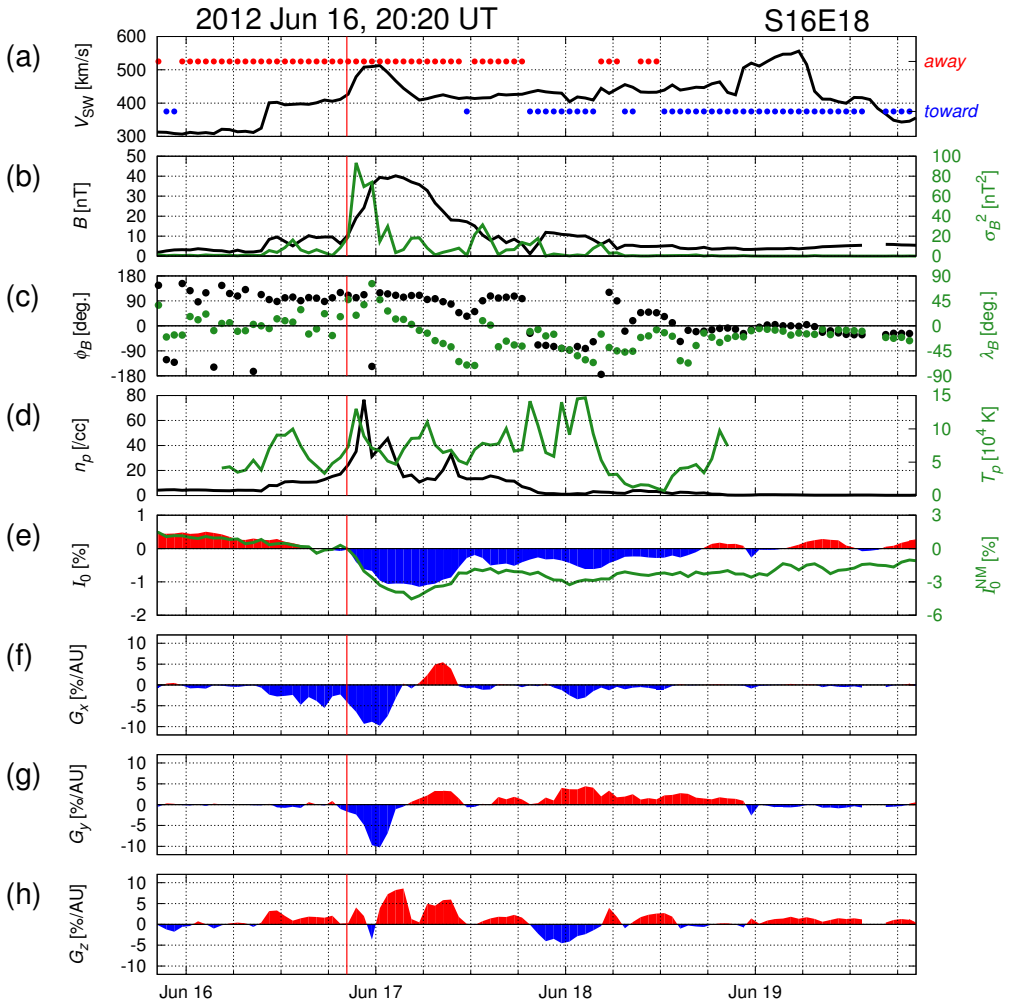

Figure 8: A sample event following the SSC on June 16, 2012 at 20:20 UT displayed in the same manner as Figure 7. (Kozai et al., 2016)

3.3.2 June 16, 2012 SSC event

This SSC event displayed in Figure 8 is observed with a CME which erupted from the sun accompanying an M1.2 solar flare on June 13, 13:41 UT at S16E18. G_y and G_z in Figures 8g and 8h show negative and positive enhancements, respectively, indicating that the density minimum region passed the south-east of the earth after propagating radially outward from the CME eruption on the sun. A nearly 180° rotation of the magnetic field latitude λ_B in Figure 8c accompanied by the rapid decrease and recovery of I_0 in Figure 8e indicates a MFR passing the earth in the first half of June 17. During the same period, ecliptic components of the gradient, G_x and G_y in Figures 8f and 8g, show clear reversals from negative to positive when the earth passes near the density minimum in the MFR. G_z remains positive during the same period possibly indicating the density minimum passed the south of the earth. It should be noted, however, that the earth is mostly in the *away* IMF sector during this period as indicated by red points in Figure 8a and the positive G_z is also expected from the drift model for the large-scale GCR transportation in *away* sector. The positive G_z in December 14, 2006 event is also observed mostly in *away* sector (see Figures 7a and 7h). I will analyze this effect in detail later in Section 3.4.4. I note again that the overall temporal variations of I_0 and I_0^{NM} in Figure 8e are in a good agreement with each other, while the magnitude of the density depression in FD is significantly larger in I_0^{NM} than in I_0, indicating a soft rigidity spectrum of the density depression in FD.

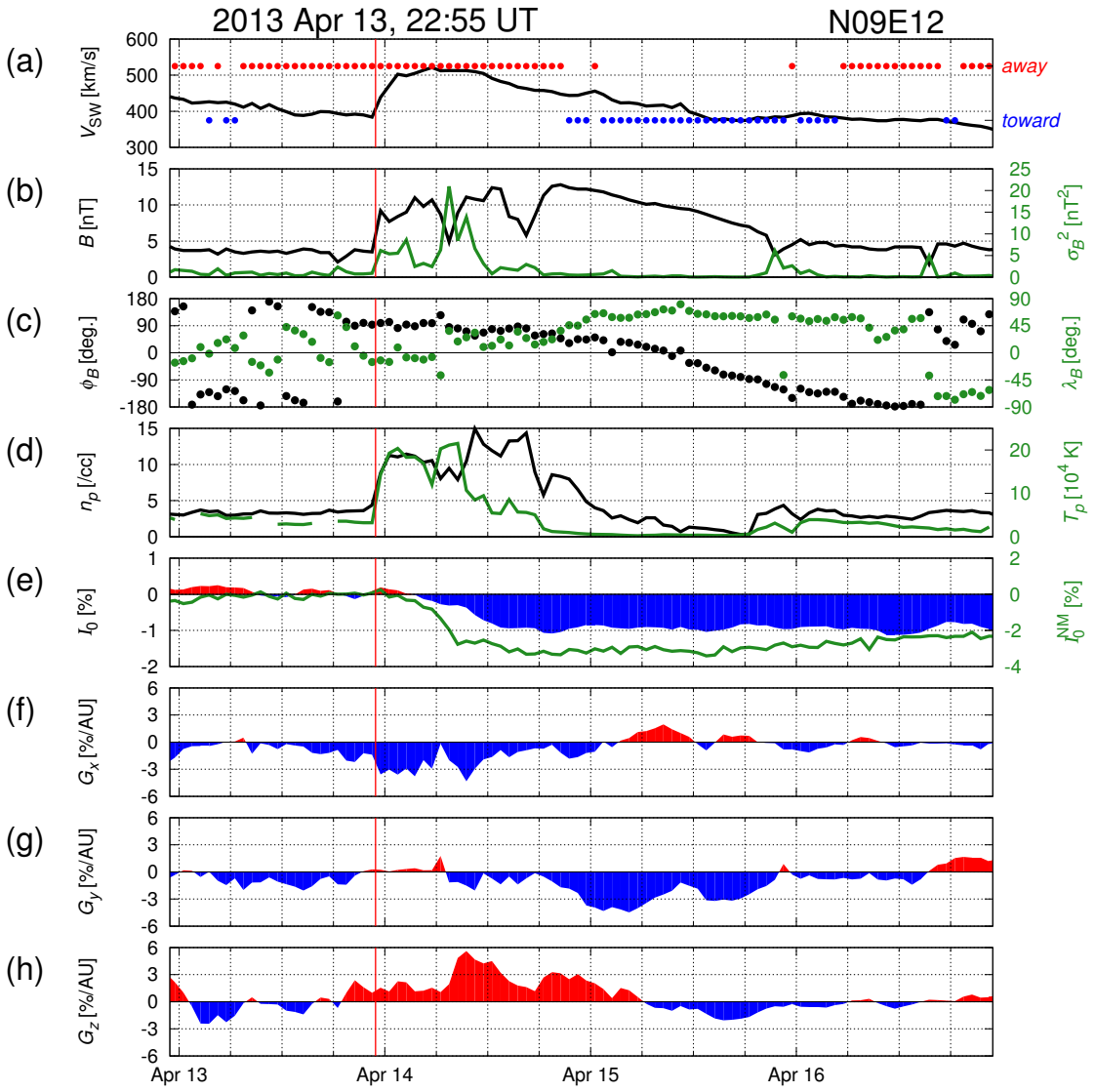

Figure 9: A sample event following the SSC on April 13, 2013 at 22:55 UT displayed in the same manner as Figure 7. (Kozai et al., 2016)

3.3.3 April 13, 2013 SSC event

This SSC event displayed in Figure 9 is observed with a CME which erupted from the sun accompanying an M6.5 solar flare on April 11, 07:10 UT at N09E12. A monotonous rotation of ϕ_B in Figure 9c and decreases of the proton density n_p and temperature T_p in Figure 9d indicate an MFR passing the earth during a day after 3/4 of April 14, but it shows only a minor effect on the GCR density I_0 and $I_0^{\rm NM}$ in Figure 9e. G_y in Figure 9g, on the other hand, shows a negative enhancement during the MFR period in accord with the GCR density minimum region propagating radially outward from the CME eruption on the sun and passing the east of the earth. G_z shows a clear reversal of its sign from positive to negative during the MFR period. G_x and G_y in June 16, 2012 SSC event displayed in the previous subsection also showed similar reversals. This typically demonstrates an advantage of the density gradient (or anisotropy) observations in deriving a three-dimensional geometry of the GCR depleted region in the MFR, which is difficult to deduce only from the observed GCR density (I_0 and $I_0^{\rm NM}$).

3.4 Superposition analysis and the average spatial distribution of GCR density

In this section, I perform a superposition analysis of the 45 central events and deduce the average spatial distribution of GCRs. As seen in sample events in Section 3.3, all events show different temporal profiles of the solar wind parameters, i.e. the duration and magnitude of the solar wind speed and magnetic field enhancements, the duration of the magnetic sheath and the MFR signatures following the sheath, are all different in one event from the other, causing different temporal variations in I_0 and $\boldsymbol{G}$. I cannot derive these individual features of each event from the superposition analysis which simply averages out these features. The analysis of the GMDN data for deriving individual event features can be found elsewhere (Munakata et al., 2003; Kuwabara et al., 2004, 2009). The superposition analysis, on the other hand, allows us to discuss the average features of I_0 and $\boldsymbol{G}$ which reflect the average spatial distribution of GCRs behind IP-shock. This is my motivation of the superposition analyses presented below.

3.4.1 Conversion of temporal variations to spatial distributions of the GCR density and gradient

The temporal variations of the solar wind parameters and the GCR density and density gradient analyzed in the preceding sections represent spatial distributions of those parameters convected radially outward by the solar wind and observed at the fixed location of the earth. Due to the difference in the average solar wind velocity, however, even an identical spatial distribution may result in different temporal variations. In order to deduce average spatial distributions more accurately from the superposition analysis presented in the following subsections, I first convert the temporal variations to the spatial distributions. By assuming the spatial distribution of a quantity $Q(x, y, z)$ in steady state on the solar wind frame, the temporal variation of Q ($Q_E(t)$) at the earth ($x_E = 0, y_E = 0, z_E = 0$) is related to the spatial distribution of Q, as

$$Q_E(t) = Q(V_{\rm SW}(t)t, 0, 0) \tag{57}$$

where t is the time measured from the SSC onset at $t = 0$ and $V_{\rm SW}(t)$ is the solar wind velocity measured at the earth at t. Thus, the time t can be converted to the GSE coordinate x as

$$x = V_{\rm SW}(t)t. \tag{58}$$

It is noted, however, that the conversion by equation (58) may cause the following technical problem. According to equation (58), two separate times t_1 and t_2 correspond to $x_1 = V_{\rm SW}(t_1)t_1$ and $x_2 = V_{\rm SW}(t_2)t_2$, respectively, and, in case of $V_{\rm SW}(t_1) \leq V_{\rm SW}(t_2)$, we can keep t and x in the same order, i.e. $x_1 < x_2$ if $t_1 < t_2$. In case of $V_{\rm SW}(t_1) > V_{\rm SW}(t_2)$, on the other hand, we may get $x_1 > x_2$ even if $t_1 < t_2$. To avoid this problem and keep x and t in the same order, I make the conversion, as

$$x(t) = \sum_{k=0}^{t/\Delta t} V_{\rm SW}(k\Delta t)\Delta t \tag{59}$$

where Δt is set at $\Delta t = 1$ hour corresponding to the hourly count rate analyzed in this thesis. Note that $x > 0$ ($x < 0$) corresponds to $t > 0$ ($t < 0$) after (before) the SSC onset and x increases toward the sun (i.e. GSE-x direction) with $x = 0$ corresponding to the IP-shock arrival at the earth at $t = 0$. $x = 0.1$ AU roughly corresponds to $t \sim 9$ hours in the case of $V_{\rm SW} = 450$ km/s.

The calculated x by equation (59) may not give us a real spatial coordinate, because I only use the solar wind velocity $V_{\rm SW}$ observed at t at the earth which is assumed to be constant after t. The real $V_{\rm SW}$ and GCR spatial distributions actually vary even in the solar wind frame due to, for instance, the expansion of the CME during the propagation through the earth. Even so, the conversion gives us an estimation of the spatial scale of the GCR distribution in FD in the vicinity of the earth which is a main subject of the present thesis. Moreover, the conversion also works for correcting each event for the difference in the average solar wind speed. It is noted that I confirmed all conclusions derived in this thesis remaining essentially unchanged before and after the conversion.

3.4.2 Average features of the GCR density distribution

Figure 10 shows the superposed spatial distributions of the solar wind speed ($V_{\rm SW}$), IMF magnitude (B) and variance (σ_B^2), proton density (n_p) and temperature (T_p), GCR densities derived from the GMDN and NM data (I_0 and $I_0^{\rm NM}$), and exponent (γ) of the power-law rigidity spectrum of the density depression estimated from I_0 and $I_0^{\rm NM}$, each as a function of the GSE-x in AU on the horizontal axis which is calculated from equation (59). The left and right panels display the superpositions of the E- and W-events defined in Section 3.2, respectively. In each panel, black (green) point and error whose scales are shown on the left (right) vertical axis are derived from the average and dispersion of the superposed spatial distributions in every $\Delta x = 0.02$ AU on the horizontal axis. The gray (green) curve whose scale is shown on the left (right) vertical axis is the average of the intense events in which the maximum density depression in NM data exceeds 2 % (see Table 1). A range of -0.2 AU $< x <$ +1 AU is covered in this figure. In case of more than two IP-shocks are recorded within this range, I use only the data before (after) the following (previous) SSC onset for the superposition throughout this thesis, in order to minimize the interference between separate events without losing events for my superposition analysis.

Average spatial distributions of $I_0(x)$ and $I_0^{\rm NM}(x)$ in Figures 10d and 10e are normalized to the average over 0.06 AU in -0.06 AU $< x <$ 0 AU. Each of them generally shows an abrupt decrease at $x = 0$ AU followed by a gradual recovery continuing up to $x = 1$ AU, i.e. a well-known feature of the typical FD. Looking at this figure closer, I also find that the initial decreasing phase of $I_0(x)$ and $I_0^{\rm NM}(x)$ (the left panels of Figures 10d and 10e) in the E-events ends within 0 AU $< x <$ 0.1 AU, the sheath region behind IP-shock as indicated by the enhanced σ_B^2, n_p and T_p in Figures 10b and 10c. This is consistent with numerical calculations (e.g. Nishida, 1982) of the "propagating diffusive barrier" model mentioned in Section 1.2.1, indicating that the cosmic ray modulation by the compressed magnetic field sheath is a main cause of the GCR density depression in the E-events. The initial decreasing phase of $I_0(x)$ and $I_0^{\rm NM}(x)$ (the right panels of Figures 10d and 10e) in the W-events, on the other hand, spreads wider up to $x \sim 0.2$ AU with a slower decreasing rate than in the E-events. Since the earth in the W-events encounters the eastern flank of IP-shock, the slower decrease of GCR density in the magnetic sheath in the W-events can be attributed to a weaker compression of IMF in the eastern flank of IP-shock as discussed in Section 1.2.1 (Cane et al., 1994). This E-W asymmetry of GCR modulation in the sheath region is seen clearer in intense events displayed by gray curves in Figures 10d and 10e.

After the initial decreasing phase, $I_0(x)$ and $I_0^{\rm NM}(x)$ also show broad minima followed by gradual recoveries. This is due to an additional GCR modulation in the central CME region (or CME ejecta) behind the sheath region which is typically indicated by a broad pit of T_p in the right panel of Figure 10c. The magnetic flux rope (MFR) often formed in the CME ejecta excludes GCRs from penetrating into the MFR by its adiabatic expansion, sometimes causing prominent GCR decreases. The GCR density depression in FDs is generally caused by these two distinct modulations respectively in the sheath and central CME regions. The modulation in the central CME region is seen clearer in $I_0(x)$ and $I_0^{\rm NM}(x)$ in W-events (the right panels of Figures 10d and 10e) than in E-events in the left panel, because of the weaker modulation in the sheath region due to the E-W asymmetry mentioned above. The modulation is also seen in intense E-events displayed by gray curves in the left panel as broad minima extending over 0.1 AU $< x <$ 0.5 AU, but the density depression is much larger in the sheath region. The maximum depression of GCR density $I_0(x)$ by the GMDN in Figure 10d is slightly larger in E-events than in W-events in accord with the E-W asymmetry in the FD magnitude mentioned in Section 1.2.1, while the asymmetry is clearer in intense events (gray curves in Figure 10d). This is probably due to the larger E-W asymmetry of the GCR modulation in the sheath in intense IP-shocks. If we look at $I_0^{\rm NM}(x)$ by NMs in Figure 10e, however, there is no such clear E-W asymmetry seen in the maximum depression even in the intense events. This is due to that the relative contribution of the modulation in the central CME region to the total GCR modulation is larger in $\sim$ 10 GV GCRs monitored by NMs than in $\sim$ 60 GV GCRs observed by the GMDN.

The rigidity dependence of GCR density depression can be quantitatively evaluated from the comparison between $I_0(x)$ and $I_0^{\rm NM}(x)$ in Figures 10d and 10e. On an assumption of a power-law dependence (P^Γ) of the density depression on the GCR rigidity (P), the power-law index gamma

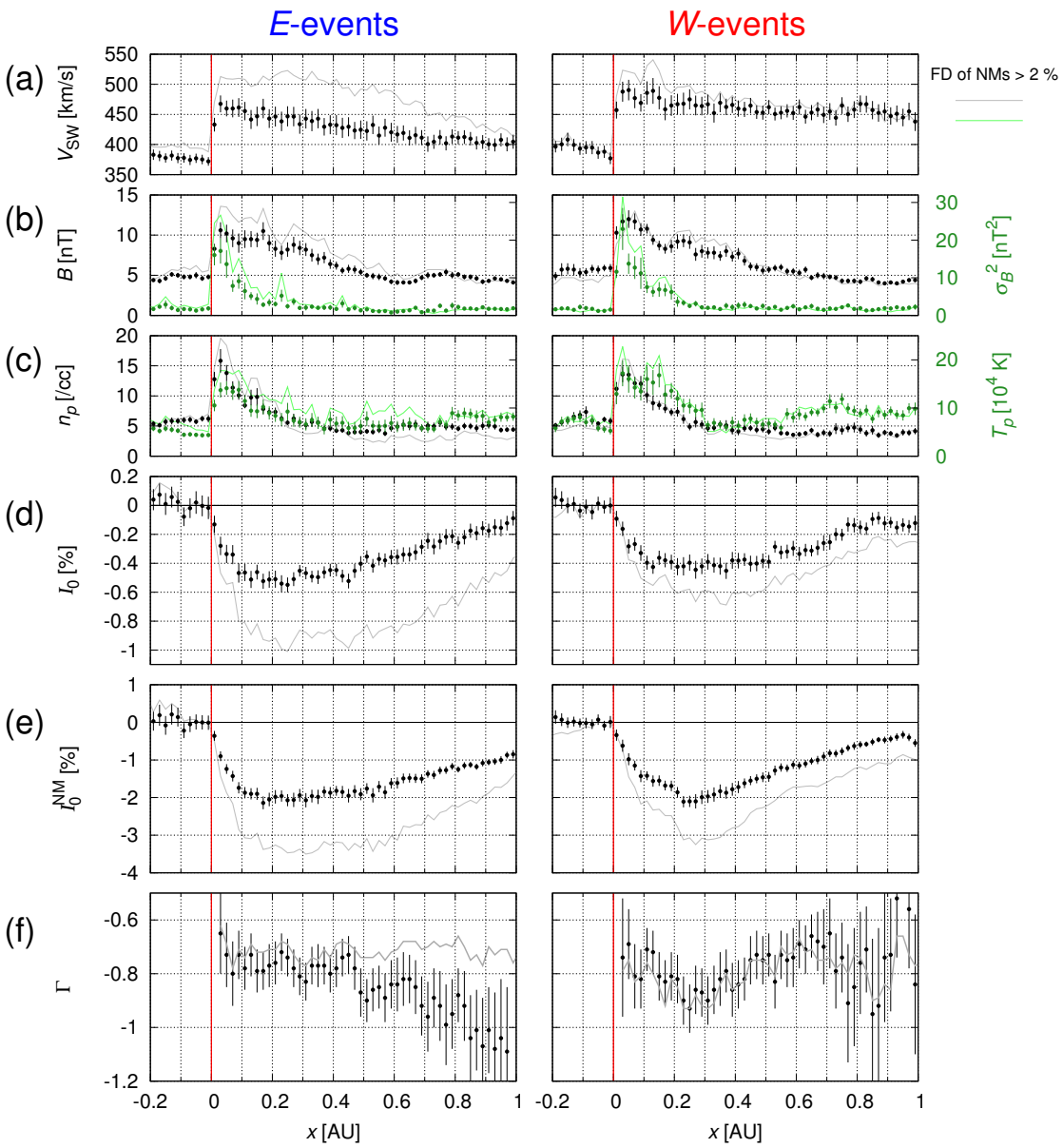

Figure 10: Averages of the superposed spatial distributions of the solar wind parameters and GCR density: (a) solar wind speed ($V_{\rm SW}$), (b) magnetic field magnitude (B) and variance (σ_B^2) measured by the ACE or WIND spacecraft, (c) solar wind proton density (n_p) and temperature (T_p), (d) GCR density (I_0) observed with the GMDN, (e) GCR density ($I_0^{\rm NM}$) observed with NMs, and (f) exponent (Γ) of the power-law rigidity spectrum of the GCR density depression, each as a function of GSE-x in AU measured from the SSC onset at $x = 0$ (or $t = 0$ in time t) indicated by a vertical red line. For the conversion from recorded time t to GSE-x, see the text. Black (green) point and error in panels (a-c), each plotted on the left (right) axis, are derived from the average and dispersion of the superposed distributions in every $\Delta x = 0.02$ AU on the horizontal axis. In panel (f), a black point is derived from the black points in panels (d) and (e) (see text), while an error bar is evaluated by an error propagation from errors in panels (d) and (e). Gray and green curves in each panel display the averages of the intense events in which the maximum density depressions in FDs derived from NM data exceed 2 %, each plotted on the left and right vertical axes, respectively. Left panels display the E-events, while right panels display the W-events (see Figure 6 and text). (Kozai et al., 2016)

can be given by the ratio $I_0(x)/I_0^{\rm NM}(x)$ as

$$\Gamma(x) = \frac{\ln\left(I_0(x)/I_0^{\rm NM}(x)\right)}{\ln\left(P_{\rm GMDN}/P_{\rm NM}\right)} \tag{60}$$

where $P_{\rm GMDN} = 60$ GV and $P_{\rm NM} = 10$ GV are representative median rigidities of primary GCRs observed with the GMDN and NMs, respectively. Figure 10f displays $\Gamma(x)$ as a function of x. The black points in Figure 10f indicate Γ derived from the black points in Figures 10d and 10e, while the gray curve in Figure 10f shows Γ derived from the gray curves in Figures 10d and 10e for intense FDs. It is seen that Γ varies in a range of -1.2 < Γ < -0.6 in accord with most of the previous studies reporting ~ 1 (Lockwood, 1960; Wada & Suda, 1980; Sakakibara et al., 1985, 1987; Morishita et al., 1990). The black points in E-events in the left panel of Figure 10f also show a rapid decrease with increasing x during the recovery phase of the FD in $x > 0.4$, implying that higher rigidity (60 GV) GCRs recover faster than lower rigidity (10 GV) GCRs. The Γ in intense E-events displayed by a gray curve in Figure 10f, on the other hand, shows no such rapid decrease in E-events, remaining at $\Gamma \sim -0.7$ up to $x = 1$. This is due to the faster and stronger shocks, as indicated by gray and green curves in Figures 10a-10c, preventing even high energy GCRs from refilling the density depleted region in FDs. The Γ in W-events (black points and a gray curve in the right panel of Figure 10f) also shows no rapid decrease, probably due to the longer duration of the enhanced solar wind velocity as shown in the right panel of Figure 10a, which is similar to the gray curve in the left panel. It is interesting to note that the Γ in W-events also shows a transit decrease to $\Gamma \sim -0.9$ in 0.2 AU $< x <$ 0.4 AU where T_p in the right panel of Figure 10c decreases and the modulation in the central CME region is observed in the right panel of Figures 10d and 10e. This implies that the modulation in the central CME region has a softer rigidity spectrum than the modulation in the sheath region. Due to this rigidity dependence, the density depression in the central CME region dominates the total depression in FD in $I_0^{\rm NM}(x)$, particularly in W-events. This is consistent with that the E-W asymmetry of the maximum density depression due to the modulation in the sheath region is seen only in $I_0(x)$ by the GMDN but not in $I_0^{\rm NM}(x)$ by NMs.

3.4.3 GCR density gradient in the ecliptic plane

Figure 11 shows the superposed GCR density and gradient derived from the GMDN data in the E- and W-events, together with the solar wind parameters, in the same manner as Figure 10. Before the SSC onset ($x < 0$), average G_x in Figure 11d has a negative offset of ~ -1 %/AU due to the radial density gradient in the steady state arising from the solar wind convection of the GCR particles (cf. Parker, 1965; Munakata et al., 2014). Following the SSC onset ($x > 0$), the negative G_x in Figure 11d shows a clear enhancement immediately behind IP-shock. This enhancement extends ~ 0.2 AU in W-events, while it extends ~ 0.1 AU in E-events. This E-W asymmetry of G_x corresponds to the longer initial decreasing phase of the density I_0 (Figure 11c) in the W-events discussed in the previous subsection. It is shown in Appendix B that G_x in Figure 11d is consistent with the spatial derivative of I_0 in Figure 11c ($dI_0(x)/dx$).

Average distribution of G_y in Figure 11e shows a broad negative (westward gradient) enhancement behind IP-shock in E-events while it shows a positive (eastward gradient) enhancement in W-events. The eastward (westward) gradient on the east (west) side of the central CME implies that the GCR density minimum is located around the longitudinal center behind IP-shock, in accord with the center-limb effect suggested by Yoshida & Akasofu (1965). This is also confirmed in the gray curve in Figure 11e, the superposition of the intense events in which the maximum density depressions in FDs derived from NM data exceed 2 %.

Figure 12 shows "bubble plots" representing the spatial distribution of G_y in all events. Solid circles plotted along a vertical line represent all G_y observed during an event as a function of GSE-x on the vertical axis while the horizontal axis represents the heliographic longitude (ϕ) of the location of the solar eruption associated with each event. Blue and red circles represent negative and positive G_y, respectively, and the diameter of each circle is proportional to $|G_y|$. The shaded area represents the heliographic region ($\phi < -45^\circ$ and $\phi > +45^\circ$) outside the central region on the sun, in which the CME events are excluded from the superposed epoch analysis

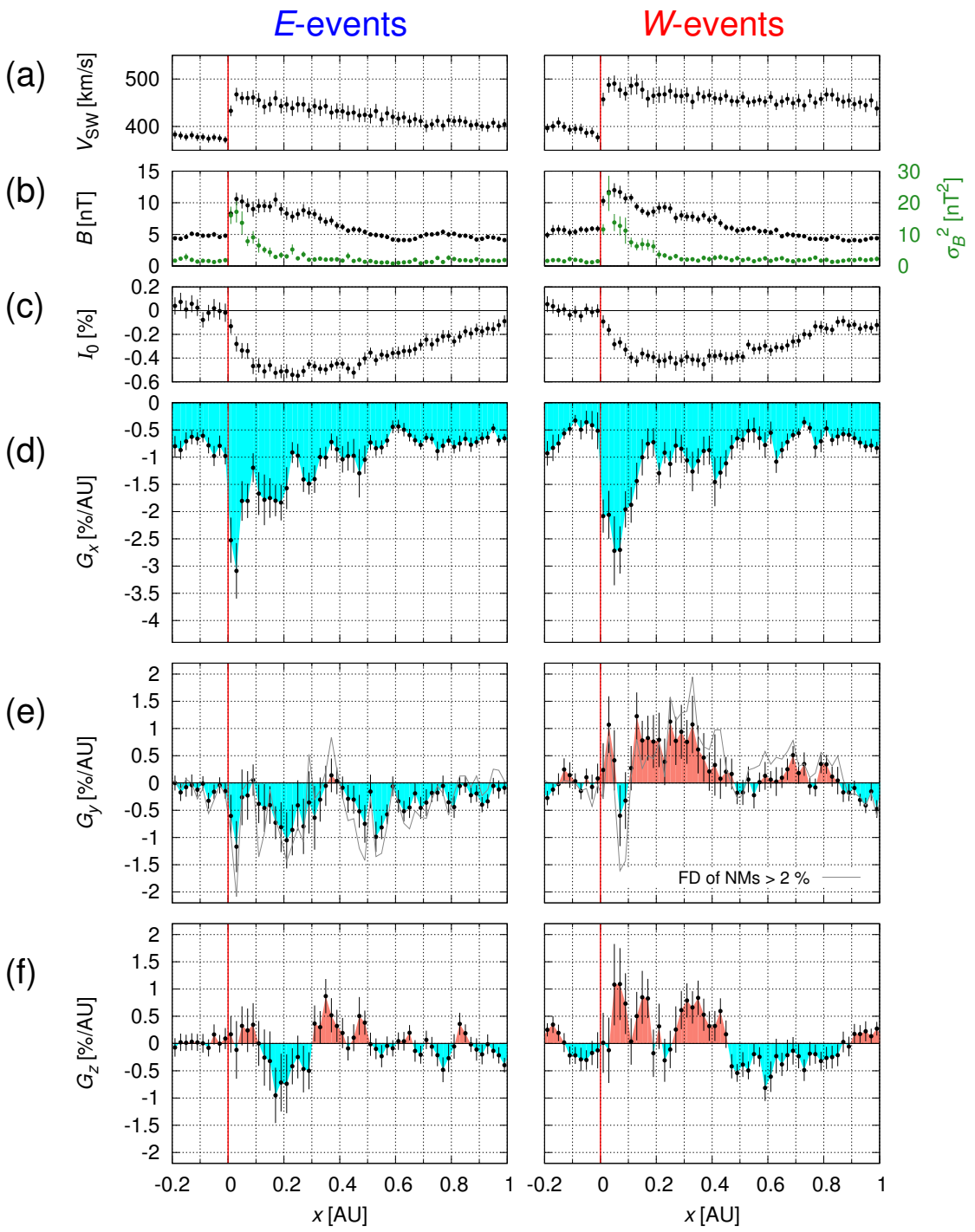

Figure 11: Averages of the superposed spatial distributions: (a-c) solar wind speed (V_{SW}), magnetic field magnitude (B) and variance (σ_B^2) and GCR density (I_0) in the same manner as Figures 10a, 10b and 10d, and (d-f) three GSE components of the GCR density gradient (G_x, G_y, G_z) derived from the GMDN data. The format is the same as Figure 10. (Kozai et al., 2016)

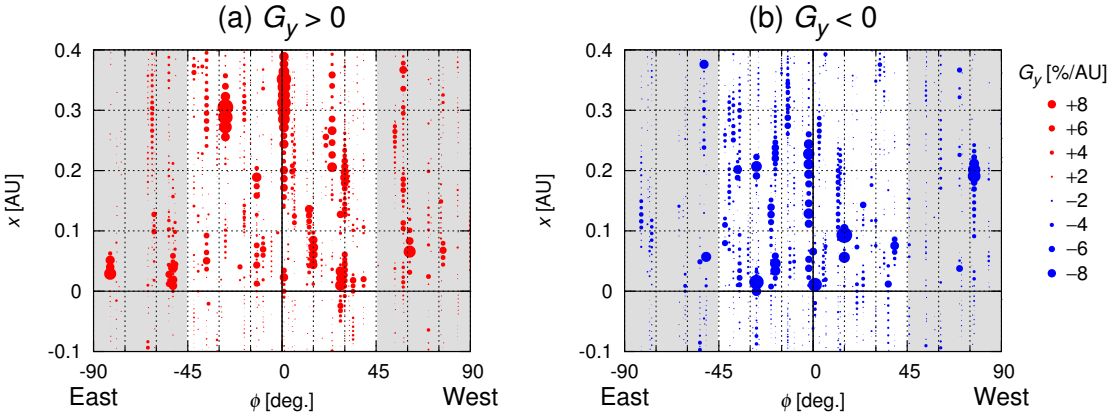

Figure 12: Spatial distribution of G_y classified according to the value of G_y: (a) distribution of positive G_y and (b) negative G_y. Different marks refer to different domains of G_y (see right of panel (b)). Solid circles along a vertical line display G_y in an event as a function of GSE-x on the vertical axis, while the horizontal axis represents the heliographic longitude (ϕ) of the solar eruption associated with each event. (Kozai et al., 2016)

in this thesis. The enhanced G_ys behind the shock front have both of the positive and negative signs in Figure 12a showing all events, but in Figures 12b and 12c showing positive and negative G_y separately, the positive G_y (red circles) is seen to be dominant in western ($\phi > 0°$) events while negative G_y (blue circles) is dominant in eastern ($\phi < 0°$) events. This asymmetry results in the enhancements with opposite signs in Figure 11e. The spatial extent of the enhancement, on the other hand, seems to be larger in G_y than in G_x, as seen in Figures 11d and 11e. It is interesting to note that G_y in Figure 11e shows simultaneous enhancements in 0 AU $< x <$ +0.1 AU with opposite signs in E- and W-events, which are possibly related to the sheath structure between IP-shock and the CME ejecta.

The north-south component of the density gradient, G_z in Figure 11f also shows a positive enhancement after the SSC onset particularly in the W-events, but this can be attributed to a north-south asymmetry of the density depression in FDs collected in this thesis. As shown in the next section, the S-events have a significantly deeper density depression than the N-events. This implies that the GCR density minima propagating radially outward from the CME eruptions on the sun were deeper when they passed the south of the earth, resulting in the positive G_z (northward gradient) enhancement in the right panel of Figure 11f. This may be the case also in the E-events, but the number of E-events is almost two times larger in the northern hemisphere (15 events) than in the southern hemisphere (7 events), as displayed by Figure 6a. This implies that the GCR density minimum region propagating radially outward from the CME eruption on the sun passed the north of the earth in most of the E-events, canceling out with the north-south asymmetry of the density depression mentioned above. The IMF sector polarity during FDs may also affect the G_z distribution as mentioned in subsection 3.3.2, but I have confirmed that the IMF sector dependence have only a minor effect on the average G_z distribution in Figure 11f, by performing the correction for the IMF sector dependence described in the next section.

3.4.4 GCR density gradient perpendicular to the ecliptic plane

Latitudinal (north-south) distribution of GCR density behind IP-shock has rarely been investigated by former works. This is partly because solar eruptions are limited in low- and mid-latitude regions on the sun (see Figres 6a and c), prohibiting reliable analyses of the latitudinal distribution from the GCR density observed at the earth's orbit. The three-dimensional gradient vector analyzed in this thesis, on the other hand, allows us to deduce the latitudinal density distribution as well as the distribution in the ecliptic plane. The north-south component of the density gradient, G_z is expected to be southward or negative (northward or positive) in the N-events

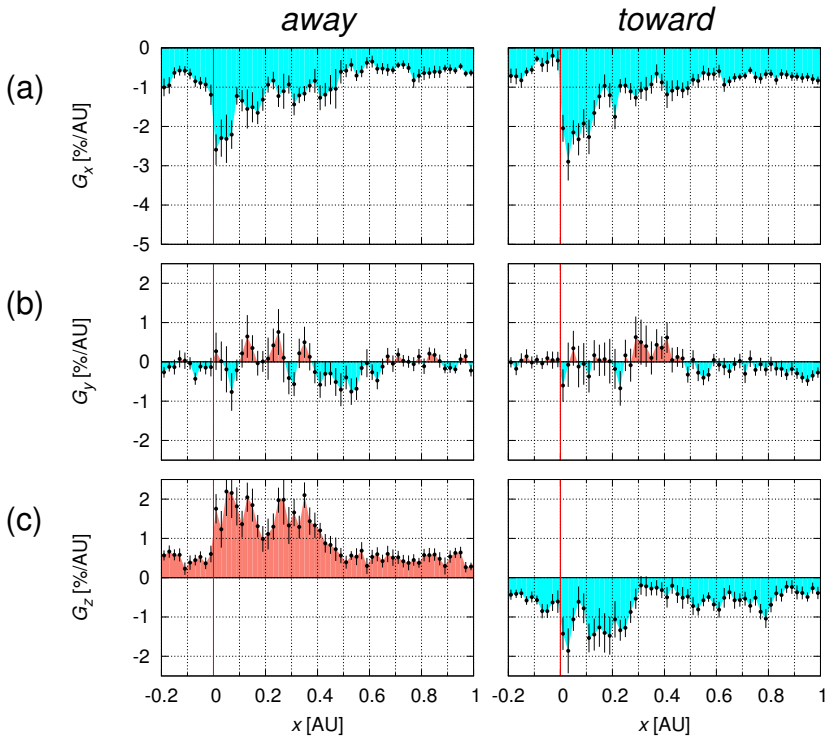

Figure 13: Averages of the superposed spatial distributions of (a) G_x, (b) G_y and (c) G_z in the same manner as Figure 11. The left panels display the average distributions in the *away* IMF sector while the right panels are in the *toward* IMF sector. For the superposition in this figure, I used only the central events, as well as Figures 10 and 11. (Kozai et al., 2016)

(S-events), if the density minimum region passes north (south) of the earth, propagating radially outward from the CME eruption in the northern (southern) hemisphere of the sun.

It is noted, however, that the sector polarity of the IMF (*away* or *toward*) also has to be taken into account when we analyze G_z, because the drift model of the large-scale GCR transport in the heliosphere predicts a persistent latitudinal gradient as mentioned in Section 1.2.2 which depends on the IMF sector polarity. The drift model predicts a spatial distribution of the GCR density having a local maximum close to the HCS in the "negative" polarity period of the solar polar magnetic field (also referred as the $A < 0$ epoch) when the IMF directs toward (away from) the sun above (below) the HCS (Kóta & Jokipii, 1982, 1983). All SSC events before 2012 in Table 1 are recorded in $A < 0$ epoch. The density distribution in $A > 0$ epoch (period from 2013 in Table 1) when the IMF directs away from (toward) the sun above (below) the HCS, on the other hand, is predicted to have a minimum close to the HCS. The drift model thus predicts positive (negative) G_z in *away* (*toward*) IMF sectors regardless of $A > 0$ or $A < 0$ epoch. This drift model prediction of G_z has been actually confirmed by previous analyses of the GMDN and NM data (Chen & Bieber, 1993; Okazaki et al., 2008; Fushishita et al., 2010a; Munakata et al., 2014; Kozai et al., 2014).

Figure 13c displays superposed G_z distributions of 45 central events in *away* and *toward* IMF sectors. In producing this figure, IMF sector polarity is designated referring to the hourly mean magnetic field $\boldsymbol{B}(t)$ in ACE or WIND data as described in subsection 3.3.1. The sector polarity is defined on an hourly basis in each event, so hourly G_zs in an event are separated into two IMF sectors, in case of the sector boundaries recorded during the event. It is clear in this figure that the average G_z is positive in the *away* sector (left panel of Figure 13c) while it is negative in the *toward* sector (right panel), in accord with the drift model prediction described above. Average distributions of G_x and G_y in Figures 13a and 13b, on the other hand, do not show such a significant dependence on the IMF sector polarity. It is also seen that the magnitude of G_z is enhanced behind IP-shock ($x > 0$), i.e. the positive (negative) G_z in the *away* (*toward*) sector is

enhanced up to 3-5 times of that ahead the shock ($x < 0$).

To correct G_z in the N- and S-events for the sector dependence mentioned above, I first calculate the average G_z in each IMF sector, respectively for the N- and S-events. I then calculate the average G_zs in the N- and S-events, as

$$G_z^{A+T}(N) = \frac{G_z^A(N) + G_z^T(N)}{2} \quad (61)$$

$$G_z^{A+T}(S) = \frac{G_z^A(S) + G_z^T(S)}{2} \quad (62)$$

where $G_z^A(N)$ and $G_z^T(N)$ ($G_z^A(S)$ and $G_z^T(S)$) are average G_zs in the *away* and *toward* sectors in the N-events (S-events), respectively. Black points in the left (right) panel of Figure 14f display the $G_z^{A+T}(N)$ ($G_z^{A+T}(S)$) distribution with errors calculated from standard errors of $G_z^A(N)$ and $G_z^T(N)$ ($G_z^A(S)$ and $G_z^T(S)$) in equations (61) and (62). Figures 14a-14e show the distributions of the solar wind speed ($V_{\rm SW}^{A+T}$), IMF magnitude (B^{A+T}) and variance ($(\sigma_B^2)^{A+T}$), GCR density I_0^{A+T} and ecliptic components (G_x^{A+T}, G_y^{A+T}) of the density gradient, all corrected for the IMF sector dependence in the same manner as equations (61) and (62).

It is clear in Figure 14f that the positive (northward) gradient is enhanced in the S-events. This is qualitatively consistent with a density minimum region propagating radially outward from the CME eruption on the sun. A negative G_z enhancement in the N-events shown by black points in the left panel of Figure 14f, on the other hand, is insignificant compared with the positive enhancement in the S-events. Durations or magnitudes of the enhancements in the solar wind speed (Figure 14a), IMF magnitude (Figure 14b) and GCR density depression (Figure 14c) are clearly shorter or smaller in the N-events than in the S-events, indicating that the N-events were weaker than the S-events. This may result in less significant negative enhancement of G_z in the N-events when compared with the positive enhancement in the S-events. In the intense events in which the maximum density depression in FDs derived from NM data exceed 2 % (gray curve in Figure 14f), we can see that in N-events the negative G_z enhancement behind IP-shock in 0 AU $< x <$ +0.2 AU is larger than the black points. I note that G_z in Figure 14f shows simultaneous enhancements in 0 AU $< x <$ +0.1 AU with opposite signs in N- and S-events, which are possibly related to the sheath structure between IP-shock and the CME ejecta as well as G_y in Figure 11e.

The GSE-y component of the density gradient, G_y in Figure 14e shows a positive enhancement in S-events, while the N-events are dominated by a negative G_y. This can be attributed to the east-west asymmetry of the N- and S-event numbers. In the central region of the southern hemisphere on the sun, 12 CMEs erupted from the western ($0^\circ \leq \phi \leq +45^\circ$) region while 7 CMEs erupted from the eastern ($-45^\circ \leq \phi < 0^\circ$) region, as seen in the event number in Figure 6a. This indicates that the CME eruptions associated with the S-events are dominated by those on the western side on the sun, which may cause the density minimum regions passing the west of the earth and the positive G_y enhancement in the right panel of Figure 14e. CME eruptions from the northern hemisphere on the sun, on the other hand, has a larger event number (15 events) in the eastern region than in the western region (11 events), possibly resulting in the negative G_y in the left panel of Figure 14e.

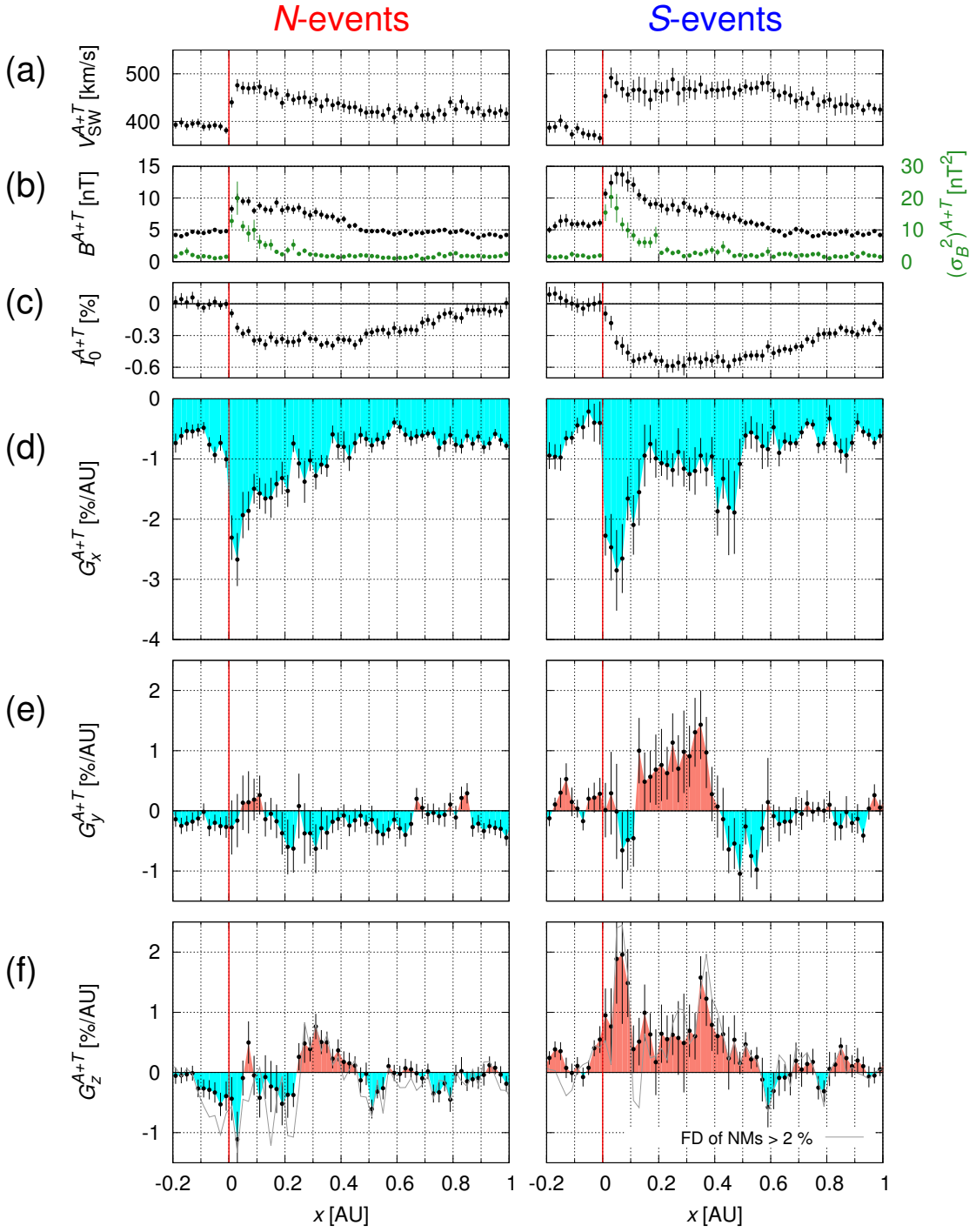

Figure 14: Averages of the superposed spatial distributions in the (left) N-events and (right) S-events: (a-c) solar wind speed ($V_{\rm SW}^{A+T}$), magnetic field magnitude (B^{A+T}) and variance $\left((\sigma_B^2)^{A+T}\right)$ and GCR density (I_0^{A+T}) in the same manner as Figures 10a, 10b and 10d, and (d-f) three GSE components of the GCR density gradient (G_x^{A+T}, G_y^{A+T}, G_z^{A+T}). Each distributions in this figure is corrected for the IMF sector polarity dependence in Figure 13 by equations (61) and (62) (see text). The format is the same as Figure 10. (Kozai et al., 2016)

3.5 Summary and discussion of the GCR depression behind IP-shocks

Most of the previous studies of FDs analyze the temporal variation of a single detector counting rate as monitoring the GCR density, or the isotropic intensity at the earth. Cosmic ray intensity observed with a ground-based detector, however, includes contributions not only from the density, but also from the GCR anisotropy simultaneously. Only a worldwide detector network, such as the GMDN, allows us to observe the cosmic ray density and anisotropy separately with a sufficient time resolution.

It has been shown in a series of papers that the GCR density gradient deduced from the anisotropy observed with the GMDN is useful to infer the three dimensional geometry of the cylinder-type depleted region in the MFR (Munakata et al., 2003, 2006; Kuwabara et al., 2004, 2009; Rockenbach et al., 2014). In this thesis, I present the superposition analysis of dozens of FDs in Table 1 observed since 2006 when the full-scale GMDN started operation. I particularly analyze the GCR density gradient deduced from the anisotropy together with the density in FDs recorded following the IP-shocks, each caused by an identified solar eruption. By analyzing the superposed density and gradient in FDs caused by eastern, western, northern and southern eruptions on the sun, i.e. the E-, W-, N- and S-events respectively, I deduced the average spatial distribution of GCRs in FDs.

I found two distinct modulations of GCR density in FDs. One is in the magnetic sheath region which extends over ~ 0.1 AU in GSE-x behind IP-shock. The density depression in the sheath region is larger in the western flank of IP-shock than in the eastern flank, because the stronger compressed IMF in the western flank shields more GCRs from outside as suggested by Haurwitz et al. (1965).

The other modulation is in the central CME region behind the sheath and causes the additional density depression in $x > 0.1$ AU. This is attributed to an adiabatic expansion of the MFR formed in the central region of CME. The density minimum at the longitudinal center behind IP-shock, which is caused by the CME ejecta or MFR, was confirmed from the negative and positive enhancements of G_y in the E- and W-events, respectively. The negative and positive G_z enhancements in the N- and S-events, indicating the density minimum at the latitudinal center behind IP-shock, are also seen when G_z is corrected for the asymmetry in the *away* and *toward* IMF sectors (that is, above and below the HCS) predicted by the drift model. I also note that the centered density minimum was seen not only in the central CME region but also in the sheath region.

By comparing the density depressions observed with the GMDN and NMs, I confirmed that the rigidity spectrum of the density depression is overall consistent with a soft power-law spectrum P^{Γ} with $\Gamma \sim -0.8$ as seen in Figure 10f. It was also found that the modulation in the central CME region has a softer rigidity spectrum than the modulation in the magnetic sheath. This may be related to a difference between GCR diffusion coefficients in the ordered magnetic field of the MFR and in the turbulent IMF in the sheath region. The rigidity spectrum getting softer during the recovery phase in E-events implies that the density depression recoveries faster in ~ 60 GV GCRs than in ~ 10 GV GCRs, while such a recovery is not seen in the W-events due to the longer duration of the solar wind speed enhancement. Previous studies (Bieber & Evenson, 1998; Munakata et al., 2003, 2006; Kuwabara et al., 2004, 2009; Rockenbach et al., 2014) analyzed the GMDN and NM data separately, but the combined analyses of these data set, as presented in the present thesis, can provide us with an important information on the rigidity dependence of GCR modulation in the space weather.

In addition to the asymmetry in the *away* and *toward* IMF sectors, G_z also shows negative and positive enhancements behind IP-shock as shown in Figure 13. An enhanced longitudinal component of IMF in the sheath behind IP-shock is expected to cause a latitudinal ∇B drift (Sarris et al., 1989) and possibly enhance the latitudinal density gradient which changes sign in *away* and *toward* IMF sectors as the observed G_z.

Average spatial distribution of the GCR density in FD presented in this thesis demonstrate that the observations of high energy GCR density and anisotropy with the GMDN and NMs provide us with good tools also for studying the space weather caused by IP-shock.

4 Solar cycle variations of the GCR anisotropy and density distribution

In this section, I analyze the GCR density distribution accompanying with the 11-year and 22-year cycle variation of the solar activity, called the space climate. In addition to the GMDN data analysis, I derive the long-term variation of the anisotropy also from data recorded by a single multi-directional MD at Nagoya, Japan for comparison, using traditional analysis methods described below.

4.1 Traditional analysis method

4.1.1 Harmonic analysis of the diurnal variation

As seen in equation (48), atmospheric muon intensity contains superposed contributions from the first order anisotropy and the density of GCRs. The harmonic analysis, which is one of the most commonly adopted traditional analysis methods, deduces only the components appear in the diurnal variation of $N_{i,j}(t)$, i.e. the diurnal anisotropy $(\xi_x^{\rm GEO}, \xi_y^{\rm GEO})$, by assuming that the GCR density I_0 and the anisotropy components $(\xi_x^{\rm GEO}, \xi_y^{\rm GEO}, \xi_z^{\rm GEO})$ vary only in a time scale longer than a day.

The fractional deviation $d_{i,j}(t)$ of the pressure corrected hourly muon count rate $N_{i,j}(t)$ at the universal time t from the 24-hours central moving average $\overline{N_{i,j}}(t)$ is given as

$$d_{i,j}(t) = \frac{N_{i,j}(t) - \overline{N_{i,j}}(t)}{\overline{N_{i,j}}(t)} \tag{63}$$

where

$$\overline{N_{i,j}}(t) = \frac{1}{24}\sum_{t-12}^{t+11} N_{i,j}(t) \tag{64}$$

is expected to represent the contributions from the density $I_0(t)$ and the z-component anisotropy $\xi_z^{\rm GEO}(t)$ because the diurnal variation should be averaged out to zero in $\overline{N_{i,j}}(t)$. I also check the difference between the maximum and minimum values of $d_{\rm McMurdo}(t)$, the fractional deviation derived by applying equation (63) to the McMurdo NM data, in every day and exclude the day with the difference exceeding 2.0 % from further analyses to avoid the influence of large cosmic ray events such as the FD, in which the assumption mentioned above is invalid. I confirmed that these excluded days include the majority of cosmic ray events reported so far (Cane et al., 1996; Jordan et al., 2011). From $d_{i,j}(t)$ in the remaining days, I obtain the monthly mean diurnal variation $D_{i,j}(t_{\rm hour})$ and its error as functions of the time of a day, as

$$D_{i,j}(t_{\rm hour}) = \frac{1}{n_k}\sum_k d_{i,j}(k; t_{\rm hour}), \tag{65}$$

$$\sigma\left(D_{i,j}(t_{\rm hour})\right) = \sqrt{\frac{\sum_k \left\{d_{i,j}(k; t_{\rm hour}) - D_{i,j}(t_{\rm hour})\right\}^2}{n_k(n_k-1)}} \tag{66}$$

where k denotes a remaining day in each month and $t_{\rm hour}$ (hour $= 1, 2, \cdots, 24$) denotes the universal time of the day. n_k is a number of the remaining days, k, in the month.

I derive the first order Fourier components $(a'_{i,j}, b'_{i,j})$ of $D_{i,j}(t_{\rm hour})$ and their errors, as

$$\begin{pmatrix} a'_{i,j} \\ b'_{i,j} \end{pmatrix} = \frac{\omega}{\pi}\sum_{\rm hour=1}^{24} D_{i,j}(t_{\rm hour}) \begin{pmatrix} \cos\omega t_{\rm hour} \\ \sin\omega t_{\rm hour} \end{pmatrix}, \tag{67}$$

$$\begin{pmatrix} \sigma(a'_{i,j}) \\ \sigma(b'_{i,j}) \end{pmatrix} = \frac{\omega}{\pi}\sqrt{\sum_{\rm hour=1}^{24} \sigma^2\left(D_{i,j}(t_{\rm hour})\right) \begin{pmatrix} \cos^2\omega t_{\rm hour} \\ \sin^2\omega t_{\rm hour} \end{pmatrix}}. \tag{68}$$

The universal time of a day, $t_{\rm hour}$, is related to the local solar time t_i at the i-th station, as

$$\omega t_{\rm hour} = \omega t_i - \phi_i^{\rm st} \tag{69}$$

where $\phi_i^{\rm st}$ is the geographic longitude of the i-th station. The Fourier components $(a'_{i,j}, b'_{i,j})$ in the universal time is related to the Fourier components $(a_{i,j}, b_{i,j})$ of $D_{i,j}(t_i)$ in the local solar time, as

$$\begin{aligned}
\begin{pmatrix} a'_{i,j} \\ b'_{i,j} \end{pmatrix} \cdot \begin{pmatrix} \cos\omega t_{\rm hour} \\ \sin\omega t_{\rm hour} \end{pmatrix} &= \begin{pmatrix} a'_{i,j} \\ b'_{i,j} \end{pmatrix} \cdot \begin{pmatrix} \cos(\omega t_i - \phi_i^{\rm st}) \\ \sin(\omega t_i - \phi_i^{\rm st}) \end{pmatrix} \\
&= \begin{pmatrix} a'_{i,j}\cos\phi_i^{\rm st} - b'_{i,j}\sin\phi_i^{\rm st} \\ a'_{i,j}\sin\phi_i^{\rm st} + b'_{i,j}\cos\phi_i^{\rm st} \end{pmatrix} \cdot \begin{pmatrix} \cos\omega t_i \\ \sin\omega t_i \end{pmatrix} \\
&= \begin{pmatrix} a_{i,j} \\ b_{i,j} \end{pmatrix} \cdot \begin{pmatrix} \cos\omega t_i \\ \sin\omega t_i \end{pmatrix}
\end{aligned} \tag{70}$$

The Fourier components in the solar local time and their errors are, therefore, derived as

$$\begin{pmatrix} a_{i,j} \\ b_{i,j} \end{pmatrix} = \begin{pmatrix} \cos\phi_i^{\rm st} & -\sin\phi_i^{\rm st} \\ \sin\phi_i^{\rm st} & \cos\phi_i^{\rm st} \end{pmatrix} \begin{pmatrix} a'_{i,j} \\ b'_{i,j} \end{pmatrix}, \tag{71}$$

$$\begin{pmatrix} \sigma^2(a_{i,j}) \\ \sigma^2(b_{i,j}) \end{pmatrix} = \begin{pmatrix} \cos^2\phi_i^{\rm st} & \sin^2\phi_i^{\rm st} \\ \sin^2\phi_i^{\rm st} & \cos^2\phi_i^{\rm st} \end{pmatrix} \begin{pmatrix} \sigma^2(a'_{i,j}) \\ \sigma^2(b'_{i,j}) \end{pmatrix}. \tag{72}$$

From equation (48), $D_{i,j}(t_i)$ in the local solar time is modeled as

$$\begin{aligned}
D_{i,j}^{\rm fit}(t_i) &= \xi_x^{\rm GEO}\left(c^1_{1i,j}\cos\omega t_i - s^1_{1i,j}\sin\omega t_i\right) \\
&\quad + \xi_y^{\rm GEO}\left(s^1_{1i,j}\cos\omega t_i + c^1_{1i,j}\sin\omega t_i\right) \\
&= a_{i,j}^{\rm fit}\cos\omega t_i + b_{i,j}^{\rm fit}\sin\omega t_i
\end{aligned} \tag{73}$$

where

$$\begin{pmatrix} a_{i,j}^{\rm fit} \\ b_{i,j}^{\rm fit} \end{pmatrix} = \begin{pmatrix} c^1_{1i,j} & s^1_{1i,j} \\ -s^1_{1i,j} & c^1_{1i,j} \end{pmatrix} \begin{pmatrix} \xi_x^{\rm GEO} \\ \xi_y^{\rm GEO} \end{pmatrix} \tag{74}$$

represent model functions of the Fourier components $(a_{i,j}, b_{i,j})$. It is noted that the diurnal variation of the atmospheric temperature also contribute to the monthly mean diurnal variation $D_{i,j}(t_i)$ and equation (74) have to be modified by adding the temperature effect, as

$$\begin{pmatrix} a_{i,j}^{\rm fit} \\ b_{i,j}^{\rm fit} \end{pmatrix} = \begin{pmatrix} c^1_{1i,j} & s^1_{1i,j} \\ -s^1_{1i,j} & c^1_{1i,j} \end{pmatrix} \begin{pmatrix} \xi_x^{\rm GEO} \\ \xi_y^{\rm GEO} \end{pmatrix} + \begin{pmatrix} a_i^{\rm com} \\ b_i^{\rm com} \end{pmatrix} \tag{75}$$

where $(a_i^{\rm com}, b_i^{\rm com})$ represents the temperature effect on the diurnal variation of muon intensity observed with the i-th detector, which is approximately common in all the directional channels (js) (Okazaki et al., 2008).

I define the residual $\chi^2_{\rm harm}$, as

$$\chi^2_{\rm harm} = \sum_{j=1}^{n_i} \left\{ \frac{\left(a_{i,j} - a_{i,j}^{\rm fit}\right)^2}{\sigma^2\left(a_{i,j}\right)} + \frac{\left(b_{i,j} - b_{i,j}^{\rm fit}\right)^2}{\sigma^2\left(b_{i,j}\right)} \right\} \tag{76}$$

where n_i is a number of directional channels in the i-th detector, which is set at $n_1 = 17$ for Nagoya MD ($i = 1$). The best-fit parameters $\xi_x^{\rm GEO}$, $\xi_y^{\rm GEO}$, $a_i^{\rm com}$ and $b_i^{\rm com}$ in equation (75) which minimize $\chi^2_{\rm harm}$ are derived by solving equations,

$$\frac{\partial(\chi^2_{\rm harm})}{\partial\xi_x^{\rm GEO}} = \frac{\partial(\chi^2_{\rm harm})}{\partial\xi_y^{\rm GEO}} = \frac{\partial(\chi^2_{\rm harm})}{\partial a_i^{\rm com}} = \frac{\partial(\chi^2_{\rm harm})}{\partial b_i^{\rm com}} = 0. \tag{77}$$

I perform this calculation for Nagoya MD data in every month.

4.1.2 Nagoya GG-component

The GG-component is a difference combination between intensities recorded in the north- and south-viewing channels of Nagoya MD corresponding to 56° north and 14° south asymptotic latitudes in free space (see Table 1 of Okazaki et al., 2008) and designed to represent the NS anisotropy ($\xi_z^{\rm GEO}$) normal to the ecliptic plane free from the atmospheric temperature effect (Nagashima et al., 1972; Mori & Nagashima, 1979). The GG-component is defined as

$$GG(t) = \{I_{\rm N2}(t) - I_{\rm S2}(t)\} + \{I_{\rm N2}(t) - I_{\rm E2}(t)\} \tag{78}$$

where $I_{\rm XX}(t)$ is the percent deviation of the pressure-corrected muon counting rate in the directional channel XX(= N2, S2, E2) of Nagoya MD from the monthly mean. Three directional channels (N2, S2, E2) used in equation (78) have a common zenith angle (49°) of the central viewing direction in the atmosphere, but the geomagnetic cut-off rigidities for these channels are different depending on the azimuth angle of each viewing direction. The GG-component in equation (78) is designed to minimize the temperature effect remaining in each of two differences due to the difference in the cut-off rigidities. From equation (48), $GG(t)$ is modeled as

$$\begin{aligned} GG(t) &= \xi_x^{\rm GEO}(t)\left(c^1_{1,GG}\cos\omega t_i - s^1_{1,GG}\sin\omega t_i\right) + \\ &\quad \xi_y^{\rm GEO}(t)\left(s^1_{1,GG}\cos\omega t_i + c^1_{1,GG}\sin\omega t_i\right) + \xi_z^{\rm GEO}(t)c^0_{1,GG} \end{aligned} \tag{79}$$

where

$$c^m_{n,GG} = 2c^m_{n,\rm N2} - c^m_{n,\rm S2} - c^m_{n,\rm E2} \tag{80}$$

$$s^m_{n,GG} = 2s^m_{n,\rm N2} - s^m_{n,\rm S2} - s^m_{n,\rm E2} \tag{81}$$

and $c^m_{n,\rm XX}$ and $s^m_{n,\rm XX}$ are the coupling coefficients calculated by equation (47) for the directional channel XX of Nagoya MD. The term of $I_0(t)$ is eliminated because of $c^0_{0,GG} = 0$. The daily mean NS anisotropy in space is calculated from the daily mean ($\overline{GG}^{\rm day}$) of $GG(t)$, as

$$\xi_z^{\rm GEO} = \overline{GG}^{\rm day}/c^0_{1,GG} \tag{82}$$

because the terms of the diurnal anisotropy ($\xi_x^{\rm GEO}, \xi_y^{\rm GEO}$) in equation (79) should be averaged out to zero in the daily mean if the diurnal anisotropy is constant over a day. The coupling coefficient $c^0_{1,GG}$ calculated from the differential coupling coefficients given by Fujimoto et al. (1984) is listed in Table 2. I note that the median rigidity of primary GCRs recorded in the GG-component is ∼80 GV and slightly higher than ∼60 GV for the entire Nagoya MD and the GMDN, because of the inclined directional channels (N2, S2, E2) responding to relatively higher rigidity GCRs.

Table 2: Coupling coefficient of the Nagoya GG-component in an unit of 10^4

	until	from		until	from
P_u [GV]	1979 Sep. 29	1979 Sep. 30	P_u [GV]	1979 Sep. 29	1979 Sep. 30
0.2E+02	-99	-101	0.7E+03	11176	10968
0.3E+02	-57	-35	0.8E+03	11323	11116
0.4E+02	688	675	0.9E+03	11437	11231
0.5E+02	1650	1591	0.1E+04	11529	11324
0.6E+02	2580	2485	0.2E+04	11949	11747
0.7E+02	3424	3301	0.3E+04	12088	11887
0.8E+02	4153	4010	0.4E+04	12159	11959
0.9E+02	4788	4629	0.5E+04	12201	12001
0.1E+03	5342	5170	0.6E+04	12229	12029
0.2E+03	8409	8199	0.7E+04	12250	12050
0.3E+03	9640	9426	0.8E+04	12265	12066
0.4E+03	10302	10090	0.9E+04	12277	12077
0.5E+03	10703	10493	0.1E+05	12286	12087
0.6E+03	10975	10765	∞	12368	12169

Coupling coefficient $c^0_{1,GG}$ for each upper limiting rigidity P_u is calculated on an assumption of the flat rigidity spectrum, $G(P)$ in equation (51). Differential coupling coefficients used for calculating $c^0_{1,GG}$ are given by Fujimoto et al. (1984).

4.2 Solar cycle variation of the 3D anisotropy

In this section, I analyze year-by-year variations of the 3D anisotropy in a period from 1992 to 2013, after the prototype GMDN started operation as a two-hemisphere network of Nagoya and Hobart MDs in 1992. Following Chen & Bieber (1993) who analyzed the solar cycle variation of the 3D anisotropy for the first time using the NM data, I average the 3D anisotropy observed with the GMDN and the NS anisotropy $\xi_z^{\rm GEO}$ derived from the GG-component over each IMF sector in every month designated as *away* (*toward*) if the daily polarity of the Stanford mean magnetic field of the sun (Wilcox Solar Observatory; WSO[7]), shifted 5 days later for a rough correction for the solar wind transit time between the sun and the earth, is positive (negative). In the harmonic analysis of the Nagoya MD data, the mean diurnal variation $D^T_{i,j}(t_{\rm hour})$ ($D^A_{i,j}(t_{\rm hour})$) is calculated by averaging $d_{i,j}(t)$ over *toward* (*away*) sector in each month. The monthly mean diurnal anisotropy in each IMF sector is then derived by equation (76). Three components ($\xi_x^{{\rm GEO}(T/A)}$, $\xi_y^{{\rm GEO}(T/A)}$, $\xi_z^{{\rm GEO}(T/A)}$) of the anisotropy in *toward*/*away* sector obtained from the GMDN and Nagoya MD are first converted to components ($\xi_x^{T/A}$, $\xi_y^{T/A}$, $\xi_z^{T/A}$) in the Geocentric Solar Ecliptic coordinate system (GSE), as

$$\xi_x^{T/A} \sim -\xi_x^{{\rm GEO}(T/A)} \tag{83}$$

$$\xi_y^{T/A} \sim -\xi_y^{{\rm GEO}(T/A)} \tag{84}$$

$$\xi_z^{T/A} = \xi_z^{{\rm GEO}(T/A)} / \cos\delta \tag{85}$$

where $\delta = 23.4^\circ$ ($\cos\delta = 0.918$) is the angle between the GSE-z axis and the GEO-z axis, i.e. the tilt angle of the earth's rotation axis from the normal line of the ecliptic plane.

From equation (26), the anisotropy components (ξ_x^w, ξ_y^w, ξ_z^w) in the solar wind frame is obtained by subtracting the contribution from the solar wind convection and the Compton-Getting effect arising from the earth's orbital motion around the sun, as

$$\xi_x^{w(T/A)} = \xi_x^{T/A} - (2+\gamma)V_{\rm SW}^{T/A}/c \tag{86}$$

$$\xi_y^{w(T/A)} = \xi_y^{T/A} + (2+\gamma)V_E/c \tag{87}$$

$$\xi_z^{w(T/A)} = \xi_z^{T/A} \tag{88}$$

where $V_{\rm SW}^{T/A}$ is the radial component of the solar wind velocity in the OMNI data[8] (King & Papitashvili, 2005) and $V_E = 30$ km/s. I then calculate parallel and perpendicular components

[7] http://wso.stanford.edu/

[8] http://omniweb.gsfc.nasa.gov/

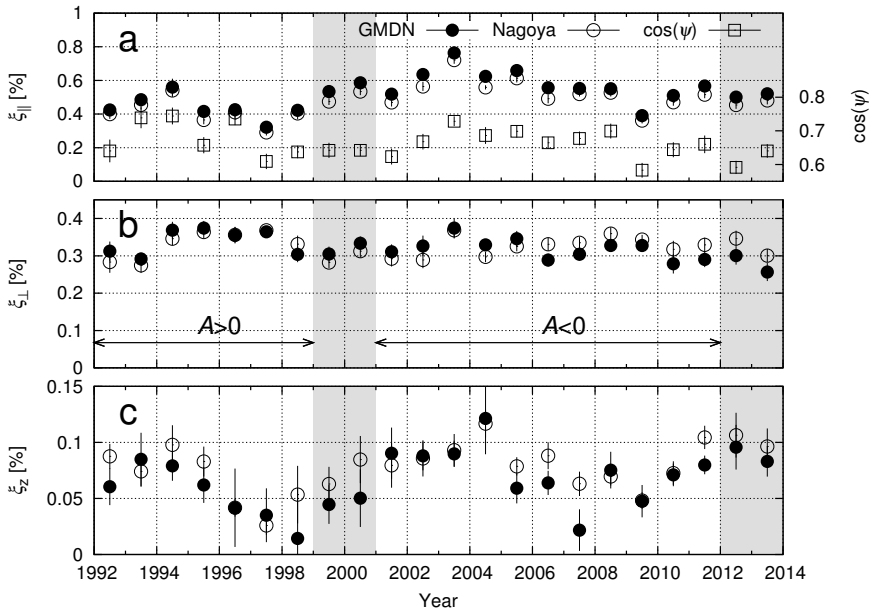

Figure 15: Long-term variations of three components of the anisotropy vector in the solar wind frame. Panels (a) to (c) display $\xi_\parallel$ (on the left vertical axis), $\xi_\perp$, and ξ_z as defined in equations (91) to (93), respectively, each as a function of year on the horizontal axis. Solid and open circles in each panel represent anisotropies derived from the GMDN and Nagoya data, respectively, while open squares in panel (a) display $\cos\psi$ on the right vertical axis. In each panel, yearly mean value and its error are deduced from the average and dispersion of monthly mean values, respectively. Gray vertical stripes indicate periods when the polarity reversal of the solar polar magnetic field (referred as $A > 0$ or $A < 0$ in the middle panel) is in progress (Kozai et al., 2014).

of the ecliptic anisotropy, as

$$\xi_\parallel^{T/A} = \xi_x^{w(T/A)} b_x^{T/A} + \xi_y^{w(T/A)} b_y^{T/A} \tag{89}$$

$$\xi_\perp^{T/A} = -\xi_x^{w(T/A)} b_y^{T/A} + \xi_y^{w(T/A)} b_x^{T/A} \tag{90}$$

where $b_x^{T/A}$ and $b_y^{T/A}$ are GSE components of a unit vector pointing away from the sun along the IMF and calculated from the mean IMF in the OMNI data. Note that positive $\xi_\parallel^{T/A}$ and $\xi_\perp^{T/A}$ correspond to the GCR streaming inward to the inner heliosphere parallel and perpendicular to IMF, respectively. I finally obtain monthly mean components of the anisotropy in the solar wind frame, as

$$\xi_\parallel = (\xi_\parallel^T + \xi_\parallel^A)/2 \tag{91}$$

$$\xi_\perp = (\xi_\perp^T + \xi_\perp^A)/2 \tag{92}$$

$$\xi_z = (\xi_z^T - \xi_z^A)/2. \tag{93}$$

If the radial density gradient G_r is always positive with the GCR density increasing away from the sun, the NS anisotropy produced from $\boldsymbol{B} \times \boldsymbol{G}$ streaming (the fourth term of the right hand side in equation (26)) reverses its orientation according to the sector polarity of the IMF vector $\boldsymbol{B}$. The definition of ξ_z in equation (93) corresponds to the NS anisotropy (ξ_z^T) in the *toward* sector on the assumption that the anisotropy vector, when averaged over one month, is symmetric with respect to the HCS (heliospheric current sheet) and the NS anisotropy lies in an opposite direction with the same magnitude above and below the HCS, as

$$\xi_z^A = -\xi_z^T. \tag{94}$$

Note that the positive ξ_z corresponds to the southward GCR streaming perpendicular to the ecliptic plane in the *toward* IMF sector. I perform calculations of $\xi_\parallel$, $\xi_\perp$, and ξ_z described above

in every month and deduce the yearly mean value and its error of each anisotropy component from the mean and dispersion of 12 monthly values, respectively.

For the following discussions of yearly mean parameter, I also assign the polarity of the solar polar magnetic field for each year referring to the "Solar Polar Field Strength" available at the WSO web-site where the average polar field strength is given in every Carrington Rotation. I assign the polarity of a year as $A > 0$ ($A < 0$) when the average polar field in the year directs away from the sun in the northern (southern) hemisphere. I regard a year as a period of the polarity reversal in progress when the year contains Carrington Rotations with the polar field pointing *away* or *toward* in both hemispheres.

Figure 15 shows the temporal variations of the yearly mean $\xi_\parallel$, $\xi_\perp$ and ξ_z as defined in equations (91) to (93) from top to bottom panels. Each panel shows that the temporal variations of the anisotropy components derived from the GMDN (solid circle) and Nagoya (open circle) data are fairly consistent with each other as far as the year to year variation is concerned. I can see that the temporal variation of $\xi_\parallel$ has two components. One is a 22-year variation resulting in a slightly larger $\xi_\parallel$ in $A < 0$ epoch (2001-2011) than in $A > 0$ epoch (1992-1998) as reported by Chen & Bieber (1993). The other is a variation correlated with $\cos\psi$, shown by open squares in Figure 15a, where ψ is the IMF spiral angle derived from OMNI data (see equation (12)). ξ_z deduced from the GMDN (solid circles), on the other hand, shows an 11-year cycle with minima in 1998 and 2007 around the solar activity minima, while $\xi_\perp$ shows no significant solar cycle variation.

4.3 Solar cycle variation of modulation parameters

I derive the modulation parameters, i.e. the spatial gradients of GCR density and mean free paths of the pitch angle scattering of GCRs in the turbulent magnetic field, from the 3D anisotropy following the analysis method developed by Chen & Bieber (1993). The longitudinal component of the density gradient, G_y can be assumed to be $G_y \sim 0$ as far as we discuss mean values averaged over the solar rotation period, ~ 27 days. Based on this assumption and equation (54), three components ($\xi_\parallel$, $\xi_\perp$, ξ_z) of the anisotropy vector derived by equations (91) to (93) are related to the modulation parameters, as

$$\xi_\parallel = \lambda_\parallel G_r \cos\psi \tag{95}$$

$$\xi_\perp = \lambda_\perp G_r \sin\psi - R_L G_z \tag{96}$$

$$\xi_z = R_L G_r \sin\psi + \lambda_\perp G_z. \tag{97}$$

where G_r and G_z are the radial and latitudinal components of the density gradient. Note that G_z represents the latitudinal density gradient in *toward* sector, being positive when the GCR density increases with increasing latitude, and changes its sign in *away* sector due to the assumed symmetry (cf. equation (94)) above and below the HCS. The bidirectional latitudinal density gradient $G_{|z|}$, which is defined to be positive (negative) when the density increases away from (toward) the HCS, is given by G_z, as

$$G_{|z|} = -\mathrm{sgn}(A) G_z \tag{98}$$

where A represents the polarity of the solar dipole magnetic moment and

$$\begin{aligned} \mathrm{sgn}(A) &= +1, \text{ for } A > 0 \text{ epoch}, \\ &= -1, \text{ for } A < 0 \text{ epoch}. \end{aligned}$$

Equations (95)-(97) include four unknown modulation parameters, $\lambda_\parallel$, $\lambda_\perp$, G_r and G_z, while we have only three components ($\xi_\parallel$, $\xi_\perp$, ξ_z) of the observed anisotropy. I therefore assume

$$\lambda_\perp / \lambda_\parallel = \alpha = 0.01 \tag{99}$$

and derive three remaining parameters, $\lambda_\parallel$, G_r and G_z. Chen & Bieber (1993) and Bieber & Chen (1991) also adopted the same constant value of α as one of representative values. From (95), we get

$$G_r = \xi_\parallel / \left(\lambda_\parallel \cos\psi\right). \tag{100}$$

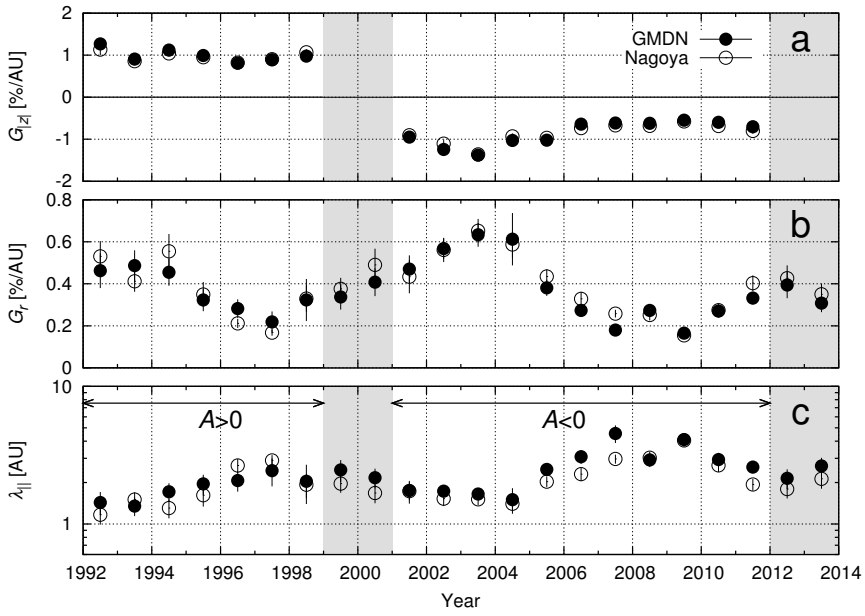

Figure 16: Long-term variations of modulation parameters derived from the 3D anisotropy in the solar wind frame. Each panel displays the yearly mean (a)$G_{|z|}$, (b)G_r and (c)$\lambda_\parallel$ as a function of year. Solid and open circles in each panel represent parameters derived from the GMDN and Nagoya data, respectively. In each panel, yearly mean value and its error are deduced from the average and dispersion of monthly mean values. Gray vertical stripes indicate periods when the polarity reversal of the solar polar magnetic field (referred as $A > 0$ or $A < 0$ in the bottom panel) is in progress. (Kozai et al., 2014)

Introducing this into (96), we get

$$G_z = \left(\alpha\xi_\parallel \tan\psi - \xi_\perp\right)/R_L. \tag{101}$$

From (95), on the other hand, we also get

$$\lambda_\parallel = \xi_\parallel/\left(G_r \cos\psi\right). \tag{102}$$

Introducing (101) and (102) into (97), we get a quadratic equation for G_r, as

$$R_L \sin\psi G_r^2 - \xi_z G_r - \alpha\xi_\parallel \left(\xi_\perp - \alpha\xi_\parallel \tan\psi\right)/\left(R_L \cos\psi\right) = 0 \tag{103}$$

which has a solution for positive G_r, as

$$G_r = \left\{\xi_z + \sqrt{\xi_z^2 + 4\alpha\xi_\parallel \tan\psi \left(\xi_\perp - \alpha\xi_\parallel \tan\psi\right)}\right\}/\left(2R_L \sin\psi\right). \tag{104}$$

I first calculate $G_{|z|}$ and G_r from equations (101) and (104), respectively, for every month. I then deduce the yearly mean and its error of each parameter from the mean and dispersion of 12 monthly values, respectively. I do not use equation (102) for calculating monthly mean $\lambda_\parallel$, because G_r becomes close to zero in some months resulting in an extremely large $\lambda_\parallel$ and large error of yearly mean $\lambda_\parallel$. This problem occurs particularly in the analysis of NM data performed in Section 4.5. I instead derive yearly mean $\lambda_\parallel$ from yearly mean G_r and $\cos\psi$ in equation (102) and deduce the error by propagating from errors of yearly mean G_r and $\cos\psi$. For R_L, I use gyro-radii of 60 GV GCRs in the monthly mean IMF with the magnitude calculated from the OMNI data.

Figure 16 displays temporal variations of modulation parameters, $G_{|z|}$, G_r and $\lambda_\parallel$ obtained from the GMDN (solid circle) and Nagoya (open circle) data from top to bottom panels. The variations with 11-year and 22-year solar cycles are clearly seen in this figure. First, significant 11-year variations are seen in both G_r and $\lambda_\parallel$ which change in a clear anti-correlation. Second,

$G_{|z|}$ is positive in $A > 0$ epoch indicating the local minimum of the density on the HCS, while it is negative in $A < 0$ epoch indicating the maximum in accord with the prediction of the drift model by Kóta & Jokipii (1983).

4.4 Comparison between the north-south (NS) anisotropies

I now discuss about the NS anisotropy, because an accurate observation of this anisotropy is crucial for obtaining a reliable 3D anisotropy and modulation parameters.

4.4.1 Previous works

I first briefly describe the previous works on the NS anisotropy. This anisotropy had been derived from NM and Nagoya MD data in two different ways. Chen & Bieber (1993) derived this anisotropy from the difference between count rates in a pair of NMs which are located near the north and south geomagnetic poles observing intensities of GCRs arriving from the north and south pole orientations, respectively. The NS anisotropy derived in this way is very sensitive to the stability of operations of two independent detectors and can be easily affected by unexpected changes of instrumental and/or environmental origins. The second method uses the diurnal variation in the sidereal time. Due to the 23.4° inclination of earth's rotation axis from the ecliptic normal, the NS anisotropy normal to the ecliptic plane can be also observed as a diurnal variation of count rate in sidereal time with the maximum phase at ∼06:00 or ∼18:00 local sidereal time (Swinson, 1969). A possible drawback of this method is that the expected amplitude of the sidereal diurnal variation (∼ 0.03 %) is roughly ten times smaller than that of the solar diurnal variation (∼ 0.4 %). The small signal in sidereal time can be easily influenced by the solar diurnal anisotropy changing during a year. Another difficulty is that one can obtain only the yearly mean anisotropy, because the influence from the solar diurnal variation, even if it is stationary through a year, can be cancelled in sidereal time only when the diurnal variation is averaged over at least one year. This makes it difficult to deduce a reliable error of the yearly mean anisotropy. Mori & Nagashima (1979) proposed the third method to derive the NS anisotropy from the GG-component of Nagoya MD, as described in detail in Section 4.1.2. The NS anisotropy depends on the sector polarity of the IMF in a manner described by equation (94). Based on this dependence, Laurenza et al. (2003) showed that the GG-component can be used for inferring reliable sector polarity. By using the GMDN which is capable of observing the NS anisotropy on an hourly basis, Okazaki et al. (2008) reported for the first time that the NS anisotropy deduced from the GG-component is consistent with the anisotropy observed with the GMDN for a year between March 2006 and March 2007.

4.4.2 NS anisotropies derived from Naogya GG and GMDN data

Figure 17 shows histograms of hourly (a and b) and daily (c and d) mean $\xi_z^{\rm GEO}$s observed by the GG-component (a and c) and GMDN (b and d) in 2006-2013, which are classified according to the IMF sectors designated as *toward* (blue histograms) if $B_x > B_y$ and *away* (red histograms) if $B_x < B_y$ by using the GSE-x, y components (B_x, B_y) of the IMF vector in the OMNI data. The hourly $\xi_z^{\rm GEO}$ observed by the GG-component is derived by applying equation (82) to the hourly $GG(t)$. The blue and red vertical dashed lines represent averages of the blue and red histograms, respectively. I define "T/A separation" following Okazaki et al. (2008) as

$$(T - A)/\sqrt{\sigma_T \sigma_A}$$

where T (A) and σ_T (σ_A) are the average and standard errors of each histogram in the *toward* (*away*) sector, respectively. It is noted that I used the standard errors as σ_T (σ_A), while Okazaki et al. (2008) used standard deviation, resulting in larger T/A separations than those in Okazaki et al. (2008). Table 3 lists $T-A$, $\sqrt{\sigma_T \sigma_A}$, T/A separation and "success rate" (Mori & Nagashima, 1979; Laurenza et al., 2003). The success rate is a ratio of the number of hours (days) when the sign of the observed $\xi_z^{\rm GEO}$ is positive (negative) in the *toward* (*away*) IMF sector to the total number of hours (days) and is introduced as a parameter indicating to what extent we

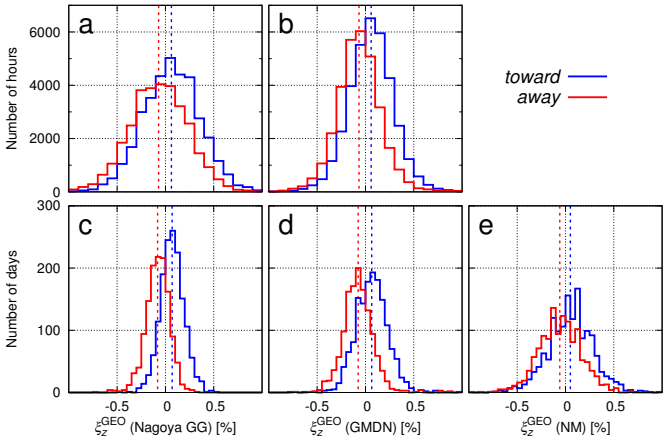

Figure 17: Histograms of the NS anisotropy. Each panel displays the histograms of $\xi_z^{\rm GEO}$ on hourly (a and b) and daily (c, d, e) bases derived from the Nagoya GG-component (a and c), the GMDN (b and d) and NM (Thule-McMurdo) (e) data in 2006-2013. Blue and red histograms in each panel represent distributions of $\xi_z^{\rm GEO}$ in *toward* and *away* IMF sectors, respectively, while blue and red vertical dashed lines represent averages of the blue and red histograms, respectively. (Kozai et al., 2014)

Table 3: $T-A$, $\sqrt{\sigma_T\sigma_A}$, T/A separation, and success rate (Kozai et al., 2014)

		Nagoya GG	GMDN	NMs
$T-A$ (%)	daily	0.1504	0.1398	0.1090
	hourly	0.1324	0.1258	-
$\sqrt{\sigma_T\sigma_A}$ (%)	daily	0.0033	0.0044	0.0062
	hourly	0.0016	0.0013	-
T/A separation	daily	46.2	31.5	17.8
	hourly	81.2	96.6	-
success rate (%)	daily	73.5	68.7	59.6
	hourly	58.2	62.0	-

Difference $(T-A)$ between average $\xi_z^{\rm GEO}$s in *toward* (T) and *away* (A) IMF sectors, geometric mean $(\sqrt{\sigma_T\sigma_A})$ of the standard errors of $\xi_z^{\rm GEO}$s in T and A sectors, "T/A separation" $(=(T-A)/\sqrt{\sigma_T\sigma_A})$ and "success rate" (see text) derived from Nagoya GG-component, GMDN, and NM (Thule-McMurdo) data in 2006-2013 on daily and hourly bases.

can infer the IMF sector polarity from the sign of the observed ξ_z. Although I use the success rate together with T/A separation for the following comparison, it is noted that a low success rate doesn't necessarily imply anything wrong in the observed ξ_z. The IMF sector polarity sensed by high energy GCRs should be regarded as the polarity averaged over a spatial scale comparable to the Larmor radii of GCRs which span ~ 0.1 AU. It is natural to expect that the IMF polarity averaged over such a large scale doesn't always follow the single-point measurement of the polarity by a satellite.

In Table 3, it is seen that the daily mean $\xi_z^{\rm GEO}$ by the GMDN shows smaller T/A separation and success rate than $\xi_z^{\rm GEO}$ deduced from the GG-component. The hourly $\xi_z^{\rm GEO}$ by the GMDN, on the other hand, has larger T/A separation and success rate than the GG-component. The hourly $\xi_z^{\rm GEO}$ by the GG-component has significantly larger dispersion in Figure 17a which reduce the T/A separation and success rate, partly due to the contribution from diurnal anisotropy as expected from equation (79). The NS anisotropy by the GMDN shows similar success rate on both daily and hourly bases, indicating that the NS anisotropy is successfully observed by the GMDN, free from the contribution from the ecliptic anisotropy even on hourly basis.

4.4.3 NS anisotropy observed with neutron monitors (NMs)

I also examine the rigidity dependence of the NS anisotropy by analyzing NM data together with the GG and GMDN data from 2006 to 2013. NMs have median responses to ~ 17 GV GCRs

(Yasue et al., 1982), while the GMDN and GG-component have median responses to ∼60 GV and ∼ 80 GV, respectively. Bieber & Pomerantz (1986) and Chen & Bieber (1993) defined the NS anisotropy measured on the ground as

$$\xi_z^G \equiv \frac{f_{\rm N} - f_{\rm S}}{f_{\rm N} + f_{\rm S}} \tag{105}$$

where $f_{\rm N}$ ($f_{\rm S}$) denotes the intensity of cosmic rays measured at the northward-viewing (southward-viewing) station. The ground-based NS anisotropy is thus derived on a daily basis from the daily mean count rates, $n_{\rm N}$ and $n_{\rm S}$, recorded by the NMs located near the north and south geographical poles, respectively, as

$$\xi_z^G = \frac{an_{\rm N} - n_{\rm S}}{an_{\rm N} + n_{\rm S}} = \frac{aR - 1}{aR + 1} \tag{106}$$

where $R = n_{\rm N}/n_{\rm S}$ and a is a normalization constant determined by the relative efficiencies of the north and south polar NMs. The constant a can be estimated for each month (Chen & Bieber, 1993), as

$$a \sim \frac{2}{R^T + R^A} = \frac{1}{\overline{R}} \tag{107}$$

where R^T (R^A) is the R averaged over *toward* (*away*) sectors in the month and $\overline{R} = (R^T + R^A)/2$. Inserting equation (107) to equation (106), the ground-based NS anisotropy is derived on a daily basis, as

$$\xi_z^G = \frac{R - \overline{R}}{R + \overline{R}} = \frac{\Delta R}{2\overline{R} + \Delta R} \sim \frac{\Delta R}{2\overline{R}} = \frac{R}{R^T + R^A} - \frac{1}{2} \tag{108}$$

where $\Delta R = R - \overline{R}$ and the terms of order $(\Delta R)^2$ and higher are neglected.

From equation (48), on the other hand, the daily mean cosmic ray intensities $f_{\rm N}$ and $f_{\rm S}$ are related to the NS anisotropy in space, $\xi_z^{\rm GEO}$, as

$$f_{\rm N} = c_{0{\rm N}}^0 I_0 + c_{1{\rm N}}^0 \xi_z^{\rm GEO} \tag{109}$$

$$f_{\rm S} = c_{0{\rm S}}^0 I_0 + c_{1{\rm S}}^0 \xi_z^{\rm GEO} \tag{110}$$

where $c_{n{\rm N}}^m$ ($c_{n{\rm S}}^m$) is the coupling coefficient of the north (south) polar NM, derived from equation (47). The terms of the diurnal anisotropy, $\xi_x^{\rm GEO}$ and $\xi_y^{\rm GEO}$, are neglected by assuming that the anisotropy is almost constant over a day. By approximating $I_0 \sim 1$ and inserting equations (109) and (110) to equation (105), we obtain

$$\xi_z^G = \frac{(c_{0{\rm N}}^0 - c_{0{\rm S}}^0) + (c_{1{\rm N}}^0 - c_{1{\rm S}}^0)\xi_z^{\rm GEO}}{(c_{0{\rm N}}^0 + c_{0{\rm S}}^0) + (c_{1{\rm N}}^0 + c_{1{\rm S}}^0)\xi_z^{\rm GEO}} \sim \frac{c_{1{\rm N}}^0 - c_{1{\rm S}}^0}{c_{0{\rm N}}^0 + c_{0{\rm S}}^0}\xi_z^{\rm GEO} \tag{111}$$

where I assume $|c_{0{\rm N}}^0 - c_{0{\rm S}}^0| << |(c_{1{\rm N}}^0 - c_{1{\rm S}}^0)\xi_z^{\rm GEO}|$ and $|c_{0{\rm N}}^0 + c_{0{\rm S}}^0| >> |(c_{1{\rm N}}^0 + c_{1{\rm S}}^0)\xi_z^{\rm GEO}|$, which are valid for the north and south polar NMs. The NS anisotropy is thus derived from the ground-based anisotropy obtained by equation (108), as

$$\xi_z^{\rm GEO} = b_{\rm NS}\xi_z^G \tag{112}$$

where $b_{\rm NS}$ is a constant calculated from coupling coefficients as

$$b_{\rm NS} = \frac{c_{0{\rm N}}^0 + c_{0{\rm S}}^0}{c_{1{\rm N}}^0 - c_{1{\rm S}}^0}. \tag{113}$$

In this section, I use Thule and McMurdo NMs as the north and south polar NMs, respectively. I also use Alert NM in Canada[9] as the north polar NM in the next Section, for a period in which the Thule NM data are unavailable. The differential coupling coefficients of Thule, McMurdo, and Alert NMs are given by Yasue et al. (1982) for both of the solar minimum and maximum periods. Table 4 lists the constant, $b_{\rm NS}$, calculated with $G(P)$ in equation (51) for each upper

[9]http://center.stelab.nagoya-u.ac.jp/WDCCR/

Table 4: Constant $b_{\rm NS}$ for the derivation of the NS anisotropy

	Thule/McMurdo		Alert/McMurdo	
P_u [GV]	solar min.	solar max.	solar min.	solar max.
0.13E+01	1.1600	1.2000	1.0980	1.2000
0.16E+01	1.1324	1.1613	1.0791	1.1250
0.20E+01	1.1135	1.1392	1.0697	1.1125
0.25E+01	1.0971	1.1099	1.0581	1.0761
0.32E+01	1.0852	1.0918	1.0483	1.0554
0.40E+01	1.0765	1.0775	1.0419	1.0447
0.50E+01	1.0680	1.0669	1.0360	1.0363
0.63E+01	1.0623	1.0597	1.0322	1.0312
0.79E+01	1.0569	1.0542	1.0287	1.0274
0.10E+02	1.0520	1.0496	1.0255	1.0241
0.13E+02	1.0488	1.0463	1.0231	1.0216
0.16E+02	1.0472	1.0448	1.0222	1.0208
0.20E+02	1.0468	1.0447	1.0226	1.0215
0.25E+02	1.0472	1.0454	1.0238	1.0230
0.32E+02	1.0481	1.0467	1.0255	1.0251
0.40E+02	1.0493	1.0482	1.0275	1.0273
0.50E+02	1.0507	1.0500	1.0295	1.0298
0.63E+02	1.0522	1.0518	1.0314	1.0321
0.79E+02	1.0535	1.0534	1.0331	1.0341
0.10E+03	1.0547	1.0549	1.0347	1.0359
0.13E+03	1.0557	1.0562	1.0359	1.0375
0.16E+03	1.0567	1.0574	1.0371	1.0390
0.20E+03	1.0575	1.0584	1.0381	1.0402
0.25E+03	1.0583	1.0594	1.0390	1.0413
0.32E+03	1.0590	1.0602	1.0398	1.0423
0.40E+03	1.0596	1.0609	1.0406	1.0432
0.50E+03	1.0602	1.0615	1.0412	1.0439
0.63E+03	1.0607	1.0621	1.0417	1.0446
0.79E+03	1.0611	1.0626	1.0422	1.0453
0.10E+04	1.0615	1.0631	1.0425	1.0457
∞	1.0634	1.0662	1.0449	1.0494

Constant $b_{\rm NS}$ (see text) for each set of the NMs, Thule/McMurdo or Alert/McMurdo, in the solar minimum and maximum periods. In this thesis, Thule NM is mainly used for the north polar NM, while Alert NM is also used for the period in which the Thule NM data are unavailable. $b_{\rm NS}$ is calculated for each upper limiting rigidity P_u on an assumption of the flat rigidity spectrum, $G(P)$ in equation (51). Differential coupling coefficients used for calculating $b_{\rm NS}$ are given by Yasue et al. (1982).

limiting rigidity, P_u. The constant $b_{\rm NS}$ used in this section is derived by averaging those for the solar minimum and maximum periods with $P_u = \infty$, that is, averaging the second and the third columns of the bottom row of Table 4, as

$$b_{\rm NS} = (1.0634 + 1.0662)/2 = 1.0648. \tag{114}$$

The T/A separation and success rate of this $\xi_z^{\rm GEO}$ represents those parameters for ∼17 GV GCRs. The result of this analysis is presented in Figure 17e and Table 3. It is seen that $T - A$ by NMs is smaller, i.e. the NS anisotropy is smaller than that obtained from the GMDN and GG-component. $T - A$ and the T/A separation are the smallest in NM data at ∼17 GV and the largest in the GG-component at ∼80 GV, with the anisotropy in the GMDN at ∼60 GV in between, suggesting that the NS anisotropy increases with increasing rigidity (Yasue, 1980).

4.5 Long-term variation over 44 years and rigidity dependence of the modulation parameters

I confirmed in Section 4.2 that the 3D anisotropy derived by the combination of the harmonic analysis and the GG-component of Nagoya MD is fairly consistent with that observed with the GMDN as far as yearly mean values are concerned. Based on this, I extend in this section the analysis period back to 1970s when only the observation with the Nagoya MD was available, and derive the long-term variation of the 3D anisotropy and modulation parameters over 44 years ($\sim$4 solar activity cycles). I also derive the anisotropy of $\sim$ 17 GV GCRs during the same period, by extending the analysis of NM data by Chen & Bieber (1993) to the most recent period. By comparing anisotropies derived from Nagoya MD and NMs whose median rigidities differ by a factor of about 3.5 from each other, I discuss the rigidity dependences of the anisotropy and the modulation parameters.

4.5.1 Previous works

I briefly introduce the previous works on the rigidity dependences below. The flat rigidity spectrum (with the upper limiting rigidity) of the diurnal anisotropy assumed in equation (51) has been also assumed in many analyses based on the equilibrium between the inward diffusion flow and the outward solar wind convection which is independent of the rigidity. Munakata et al. (1997) treated the upper limiting rigidity P_u as a free parameter in their analyses of the diurnal anisotropy observed with multi-directional MDs. They found P_u changing between 100 and 300 GV in a clear correlation with the solar activity (Munakata et al., 2002). Hall et al. (1997) assumed a power-law rigidity spectrum, $\propto P^\nu$, with both ν and P_u used as free parameters in their analyses of the NM and MD data and reported the temporal variation of each parameter in solar activity and solar magnetic cycles.

All these works take account of the rigidity dependence of the amplitude varying as a function of time, but they still assume the phase of the space harmonic vector (i.e. $(\xi_x^{\rm GEO}, \xi_y^{\rm GEO})$ in equation (75)) independent of rigidity. In other words, they assumed a common rigidity spectrum for two ecliptic components, parallel and perpendicular to the IMF. Bieber & Chen (1991), on the other hand, also reported that the magnitude of the observed phase variation in $A > 0$ solar minimum increases with GCR rigidity (Agrawal, 1983). This rigidity dependent feature of the observed phase variation cannot be reproduced properly, as long as one rigidity spectrum common for two ecliptic components is assumed. This observed feature has been confirmed by other papers (e.g. Oh et al., 2010), but its physical origin is still left unknown.

The rigidity spectrum of the NS anisotropy has also been studied. Yasue (1980) analyzed the sidereal diurnal variation observed by NMs and MDs during 5 years between 1969 and 1973 and found that observations were reproduced best by the average rigidity spectrum with $\nu = 0.3$ and $P_u = 200$ GV. This was the first experimental indication that the rigidity spectrum of the NS anisotropy has a positive spectral index. Hall et al. (1994) also applied the same method to NM and MD data observed between 1957 and 1985 and found the average spectrum with $\nu = 0.5$ and $P_u = 400$ GV, again with a positive ν. This suggests that each of two ecliptic components may also have a spectrum with non-zero ν.

In this thesis, I do not intend to determine each rigidity spectrum quantitatively by, for instance, calculating both ν and P_u as free parameters in the best-fit calculation in every year. In such best-fit calculations, we often see a significant anti-correlation between the best-fit ν and P_u (Hall et al., 1994, 1997). A large P_u with a small (or negative) ν often returns similar χ^2-value as a small P_u with large (or positive) ν does, increasing the systematic error of each best-fit value. I instead examine the rigidity spectrum qualitatively based on the ratio between parameters derived from NM and Nagoya MD data with a common assumption of the spectrum with fixed values of $\nu = 0$ and $P_u = 100$ GV, respectively, as done in Chen & Bieber (1993). If the ratio is close to one, the spectrum is consistent with the assumption. If the ratio is significantly larger (smaller) than one, on the other hand, we can conclude that the spectrum is harder (softer) than the assumed one. In this way, I can make a qualitative but reliable examination of the rigidity dependence of each parameter.

4.5.2 Data analysis

Nagoya MD data In this section, I set P_u in equation (51) at $P_u = 100$ GV. The NS anisotropy $\xi_z^{\rm GEO}$ of 60 GV GCRs is derived from the GG-component using equation (82) with the coupling coefficient c^1_{1GG} calculated on an assumption of $P_u = 100$ GV.

The upper limiting rigidity of the Compton-Getting anisotropy arising from the earth's orbital motion around the sun is infinite and much higher than 100 GV. This anisotropy is given in the GSE coordinate system, as

$$\begin{pmatrix} \xi_x^{\rm CG} \\ \xi_y^{\rm CG} \end{pmatrix} = \begin{pmatrix} 0 \\ -(2+\gamma)V_E/c \end{pmatrix} \tag{115}$$

where γ and V_E are set at 2.7 and 30 km/s, respectively. The harmonic components of the j-th directional channel of Nagoya MD are then given as

$$\begin{pmatrix} a_j^{\rm CG} \\ b_j^{\rm CG} \end{pmatrix} = \begin{pmatrix} c_{1j}^{\rm 1CG} & s_{1j}^{\rm 1CG} \\ -s_{1j}^{\rm 1CG} & c_{1j}^{\rm 1CG} \end{pmatrix} \begin{pmatrix} \xi_x^{\rm CG(GEO)} \\ \xi_y^{\rm CG(GEO)} \end{pmatrix} \tag{116}$$

where $\xi_x^{\rm CG(GEO)}$ and $\xi_y^{\rm CG(GEO)}$ are the space anisotropy components in the GEO coordinate system transformed from $\xi_x^{\rm CG}$ and $\xi_y^{\rm CG}$. Coupling coefficients $c_{1j}^{\rm 1CG}$ and $s_{1j}^{\rm 1CG}$ in equation (116) are calculated from equation (47) using $G(P)$ with $P_u = \infty$ in equation (51). I subtract $(a_j^{\rm CG}, b_j^{\rm CG})$ from the harmonics (a_j, b_j) in equation (71) observed with the j-th directional channel of Nagoya MD. I then best-fit the model function (75) using equation (76) and obtain the diurnal anisotropy in free space, $(\xi_x^{\rm GEO}, \xi_y^{\rm GEO})$ corrected for the Compton-Getting anisotropy.

In Section 4.2, the Compton-Getting anisotropy $(\xi_x^{\rm CG}, \xi_y^{\rm CG})$ was subtracted from the space harmonics (ξ_x, ξ_y) in equations (86) and (87), because the upper limiting rigidity ($P_u = 10^5$ GV) was commonly set for both of $(\xi_x^{\rm CG}, \xi_y^{\rm CG})$ and the space harmonics (ξ_x, ξ_y) corrected for the Compton-Getting anisotropy. In this section, on the other hand, P_u is set at 100 GV only for the anisotropy corrected for the Compton-Getting anisotropy, differently from $P_u = \infty$ for $(\xi_x^{\rm CG}, \xi_y^{\rm CG})$, and it is required to correct the Compton-Getting anisotropy $(a_j^{\rm CG}, b_j^{\rm CG})$ in the ground-based harmonics (a_j, b_j) observed with each directional channel (j). The difference of the upper limiting rigidity ($P_u = 10^5$ GV and 100 GV) between the former sections (4.2 to 4.4) and the present section causes differences of magnitudes of the anisotropy $(\xi_\parallel, \xi_\perp, \xi_z)$ and modulation parameters $(G_{|z|}, G_r, \lambda_\parallel)$. I note, however, that the differences of the magnitudes are time-independent and the solar cycle variation of each parameter discussed in this thesis is not affected by the assumption of P_u. Results derived with different P_us will be also shown and discussed in Appendix C.

Figure 18 displays sample comparisons between the best-fit and the observed yearly mean harmonic vectors for Nagoya MD in 2002 and 1976 when the solar activity were close to the maximum and minimum, respectively. It is clear that the amplitude of the derived space harmonic vector indicated in each panel is significantly larger in 2002 around the solar maximum period than that in 1976 causing an "expansion" of the pattern drawn by lines connecting heads of harmonic vectors observed by 17 directional channels. It is also clear that the phase of the derived space harmonic vector is about 4 hours earlier in 1976 than in 2002, due to the 22-year variation of the diurnal anisotropy.

Figure 19 displays a long-term variation of the common vector $(a_{\rm com}, b_{\rm com})$, which is introduced to represent the atmospheric temperature effect in equation (75). The mean amplitude of the common vector is small (0.039 ± 0.002 %), while the phase is almost stable around $\sim$ 06:00 local time in an agreement with the average temperature effect reported from muon observations (e.g. Mori et al., 1988). It is also seen in Figure 19 that the common vector shows no notable long-term variations in correlation with the solar activity- or magnetic-cycle.

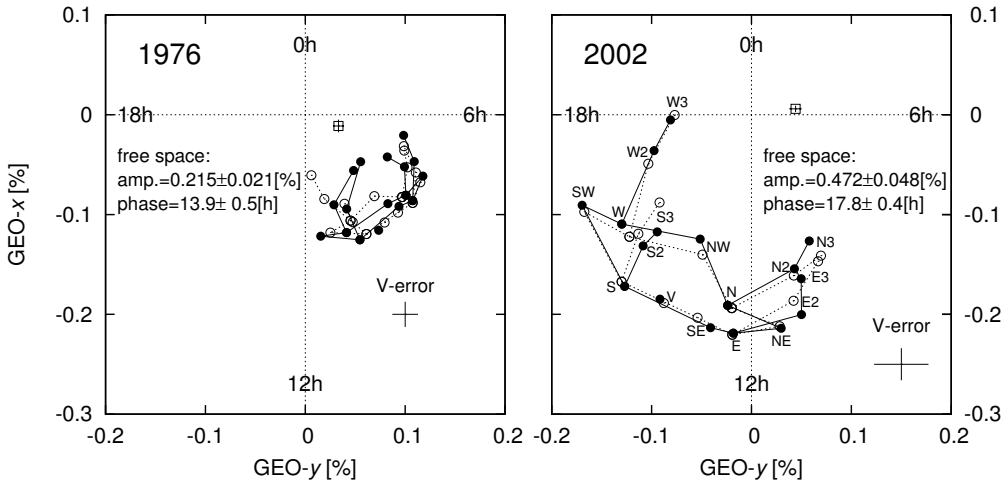

Figure 18: Yearly mean harmonic dials of the diurnal anisotropy observed by the Nagoya MD in 1976 (left) around $A > 0$ solar activity minimum and in 2002 (right) around $A < 0$ solar activity maximum. Solid circles display the harmonic vector (a_j, b_j) observed by the j-th directional channel with a_j and b_j plotted on the vertical (GEO-x) and horizontal (GEO-y) axes, respectively, while open circles display the best-fit vectors. The phases of the diurnal anisotropy with $x > 0$ and $y = 0$, $x = 0$ and $y > 0$, $x < 0$ and $y = 0$, and $x = 0$ and $y < 0$ are 00:00, 06:00, 12:00, 18:00 in the local solar time, respectively. To demonstrate the relative configuration of the observed (best-fit) harmonic vectors in 17 directional channels, the head of each vector is connected with each other by solid (dotted) thin lines (see directional channels indicated in the right panel). An open square with an error cross in each panel displays the common vector representing the atmospheric temperature effect. Amplitude and phase of the best-fit harmonic vector in free space are indicated in each panel. For reference, the cross in the bottom-right corner in each panel represents errors of a_j and b_j in vertical (V) channel, deduced from the dispersion of monthly values. (Munakata et al., 2014)

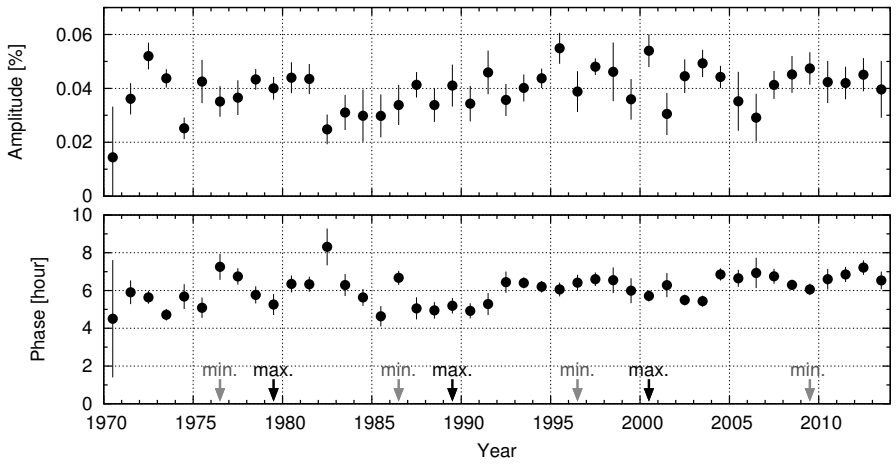

Figure 19: Long-term variation of the common vector $(a_i^{\rm com}, b_i^{\rm com})$ in equation (75). Yearly mean amplitude in % and phase (denoted by the local solar time of the maximum intensity) in hour of the common vector are displayed in the upper and lower panels, respectively, each as a function of year on the horizontal axis. The common vector is introduced as a free parameter representing the atmospheric temperature effect on the diurnal anisotropy observed with the Nagoya MD (see text). Yearly mean and error are deduced from the mean and dispersion of monthly mean values, respectively. (Munakata et al., 2014)

NM data I derive the diurnal anisotropy of $\sim$ 17 GV GCRs from Swarthmore/Newark NM data[10]. A fractional deviation from the 24-hours central moving average, $d_{\rm Newark}(t)$, is calculated from the neutron count rate using equation (63). I then obtain the monthly mean diurnal variation ($D_{\rm Newark}(t_{\rm hour})$) and the first harmonic components ($a_{\rm Newark}, b_{\rm Newark}$) in the local solar time in the same manner as Section 4.1.1. The expected harmonic components arising from the Compton-Getting anisotropy are given as

$$\left(\begin{array}{c} a^{\rm CG}_{\rm Newark} \\ b^{\rm CG}_{\rm Newark} \end{array} \right) = \left(\begin{array}{cc} c^{\rm 1CG}_{\rm 1Newark} & s^{\rm 1CG}_{\rm 1Newark} \\ -s^{\rm 1CG}_{\rm 1Newark} & c^{\rm 1CG}_{\rm 1Newark} \end{array} \right) \left(\begin{array}{c} \xi^{\rm CG(GEO)}_x \\ \xi^{\rm CG(GEO)}_y \end{array} \right) \tag{117}$$

similarly to equation (116). The first harmonic components ($a_{\rm Newark}, b_{\rm Newark}$) corrected for the Compton-Getting anisotropy by subtracting ($a^{\rm CG}_{\rm Newark}, b^{\rm CG}_{\rm Newark}$) are related to the space harmonics ($\xi^{\rm GEO}_x, \xi^{\rm GEO}_y$), as

$$\left(\begin{array}{c} a_{\rm Newark} \\ b_{\rm Newark} \end{array} \right) = \left(\begin{array}{cc} c^{1}_{\rm 1Newark} & s^{1}_{\rm 1Newark} \\ -s^{1}_{\rm 1Newark} & c^{1}_{\rm 1Newark} \end{array} \right) \left(\begin{array}{c} \xi^{\rm GEO}_x \\ \xi^{\rm GEO}_y \end{array} \right). \tag{118}$$

The coupling coefficients of Swarthmore/Newark NM, $c^m_{n\rm Newark}$ and $s^m_{n\rm Newark}$ in equations (117) and (118), are calculated by equation (47) with the same $G(P)$ used in the analysis of Nagoya MD data and the differential coupling coefficients given by Yasue et al. (1982). Equation (118) has a different form from equation (75) by the common vector ($a^{\rm com}_i, b^{\rm com}_i$), because the NM count rate is thought to be almost free from the influence of the atmospheric temperature variation. The space harmonics at $\sim$ 17 GV GCRs are given as

$$\left(\begin{array}{c} \xi^{\rm GEO}_x \\ \xi^{\rm GEO}_y \end{array} \right) = \left(\begin{array}{cc} c^{1}_{\rm 1Newark} & s^{1}_{\rm 1Newark} \\ -s^{1}_{\rm 1Newark} & c^{1}_{\rm 1Newark} \end{array} \right)^{-1} \left(\begin{array}{c} a_{\rm Newark} \\ b_{\rm Newark} \end{array} \right). \tag{119}$$

From equations (85), (93), (108), and (112), the NS anisotropy ξ_z of $\sim$ 17 GV GCRs is derived as

$$\xi_z = \frac{b_{\rm NS}}{2\cos\delta} \frac{R^T - R^A}{R^T + R^A}. \tag{120}$$

I use Thule and McMurdo NMs for the north and south polar NMs, respectively, again. For a period between 1976 and 1978 in which Thule NM data are unavailable, I use Alert NM data instead of the Thule NM data. The constant $b_{\rm NS}$ of Thule/McMurdo (Alert/McMurdo) NMs is calculated by averaging those for the solar minimum and maximum periods with $P_u = 100$ GV, i.e. averaging the second and the third columns (the fourth and the fifth columns) of the row of $P_u = 100$ GV in Talbe 4, as

$$\begin{aligned} b_{\rm NS} &= (1.0547 + 1.0549)/2 = 1.0548 \\ (b_{\rm NS} &= (1.0347 + 1.0359)/2 = 1.0353)\,. \end{aligned} \tag{121}$$

I confirmed that the anisotropy components derived from NM data in this section are consistent with those in Chen & Bieber (1993), which analyzed the same NM data in a similar manner during an overlapping period between 1970 and 1988 (Appendix D).

4.5.3 Anisotropy components

Figure 20 displays temporal variations of the amplitude (upper panel) and phase (lower panel) of the yearly mean harmonic vector in free-space. The amplitude is $\sim$ 4 % on the average while the phase stays around 18:00 local solar time in both of the MD (solid circles) and NM (open circles) data, in an agreement with the co-rotation anisotropy described in Section 1.1.2 which indicates the equilibrium between the diffusion and convection flows of GCRs. It is clearly seen that the phase in the lower panel shows a prominent 22-year variation, with minima occurring in 1976 and 1997 around $A > 0$ solar minima. This phase variation is about $\sim$ 2 hours in NM

[10] http://neutronm.bartol.udel.edu/

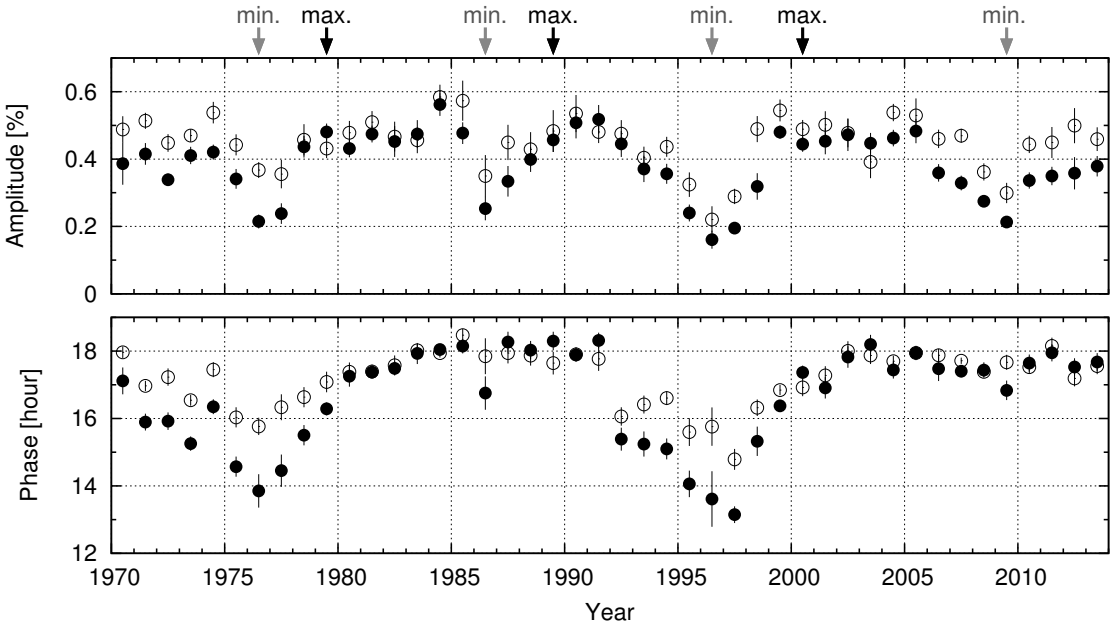

Figure 20: Diurnal anisotropy in free-space. Yearly mean amplitude in % and phase (denoted by the local solar time of the maximum intensity) in hour of the diurnal anisotropy are displayed in the upper and lower panels, respectively, each as a function of year on the horizontal axis. The solid and open circles display the anisotropy obtained from Nagoya MD data at 60 GV and from NM data at 17 GV, respectively. The diurnal anisotropy in this figure is corrected for the Compton-Getting effect arising from the earth's orbital motion around the sun (see text). Yearly mean and error are deduced from the mean and dispersion of monthly mean values, respectively. The black and gray arrows above the upper panel indicate the solar maximum and minimum years. (Munakata et al., 2014)

data, while it is almost double ($\sim$ 4 hours) in Nagoya MD data. The amplitude of the diurnal anisotropy in the upper panel is smaller (larger) around the solar minimum (maximum) period in both the NM and Nagoya MD data.

In order to calculate the 3D anisotropy in each IMF sector, I identify the sector polarity (*toward* or *away*) of each day referring to the polarity of the Stanford Mean Magnetic Field of the sun provided by the WSO, as described in Sections 4.2 and 4.3. For the period prior to 1975 when the data are not available on the WSO web-site, I identify the polarity by the OMNI magnetic field data following the analysis by Bieber & Chen (1991). Because of serious gaps in the OMNI data particularly in 1980's and 1990's, I give it up to use the OMNI IMF data for an entire period of this analysis. By analyzing a period when both the Stanford Mean Magnetic Field and the OMNI data are available, I confirmed that the daily sector polarities identified by these two methods are quite consistent with each other.

The polarity of the solar polar magnetic field is also assigned in the same way as Sections 4.2 and 4.3, referring to the Solar Polar Field Strength by WSO. For a period prior to 1975 when the WSO data are unavailable, I follow the assignment by Chen & Bieber (1993).

The anisotropy components ($\xi_x^{\mathrm{GEO}(T/A)}, \xi_y^{\mathrm{GEO}(T/A)}, \xi_z^{\mathrm{GEO}(T/A)}$) in the GEO coordinate system in each IMF sector is transformed to the GSE coordinate system by equations (83) to (85) and corrected for the solar wind convection by equation (86). Figure 21 shows $\xi_\parallel$, $\xi_\perp$ and ξ_z calculated from equations (91) to (93), each as a function of year. It is seen that three components of the anisotropy derived from Nagoya MD data (solid circles) are all positive throughout the entire period in this figure. A clear 22-year variation seen in $\xi_\parallel$ in Figure 21a indicates that this component anisotropy is responsible for the phase variation in Figure 20 as discovered in Chen & Bieber (1993) and Bieber & Chen (1991). No such clear signature of 22-year variation is seen in either $\xi_\perp$ or ξ_z displayed in figures 21b and 21c.

There is a close correlation between the variation of the $\xi_\parallel$ values obtained for NMs at 17 GV

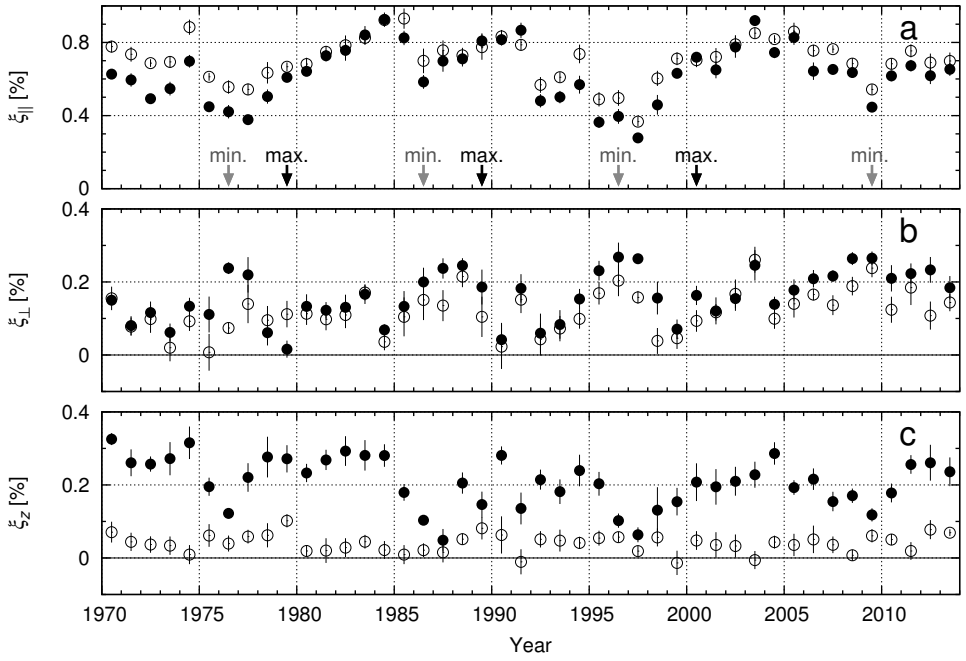

Figure 21: Three components of the anisotropy in the solar wind frame. Each panel from top to bottom displays the yearly mean $\xi_\parallel$, $\xi_\perp$ and ξ_z in % as a function of year. Solid circles display the anisotropy components derived from Nagoya MD data at 60 GV, while open circles show the anisotropy derived from NM data at 17 GV. Yearly mean and error are deduced from the mean and dispersion of monthly mean values, respectively. (Munakata et al., 2014)

and for Nagoya MD at 60 GV (open and solid circles in Figure 21a, respectively), indicating a weak rigidity dependence of this anisotropy component. A scatter plot of $\xi_\parallel$ for NMs and that for Nagoya MD on the x and y axes, respectively, yields a correlation coefficient r=0.92 and a slope (ratio) of $y/x = \beta$ =0.89±0.05, which suggests that $\xi_\parallel$ remains nearly constant despite the factor of 3.5 difference between the rigidity ranges monitored by NM and Nagoya MD. On the other hand, I find β =0.77±0.07 for $A > 0$ which is significantly smaller than the value of β =0.94±0.005 found for the $A < 0$ epochs, showing that the rigidity spectrum of $\xi_\parallel$ is softer in the $A > 0$ epochs. I also see a remarkable correlation between $\xi_\perp$ for NMs and that for Nagoya MD with $r = 0.75$, while the β values turn out to be 1.65±0.35 (1.26±0.14) in $A > 0$ ($A < 0$) epochs, which indicates that $\xi_\perp$ increases with increasing P_m. The most significant difference between NM and Nagoya MD data is seen in the magnitude of ξ_z shown in Figure 21c. For this component, I obtain β =4.45±0.61 (6.08±0.96) for the $A > 0$ ($A < 0$) epochs, which implies that ξ_z increases with increasing rigidity. The correlation between NM and Nagoya MD data is, however, quite poor ($r = 0.20$) for this component. These features appearing in Figure 21 are qualitatively consistent with $\xi_\perp$ and ξ_z increasing with rigidity. The ratios β for the three anisotropy components are listed in the column of "P_u=100 GV" in Table 5 in Appendix C.

I cannot derive any quantitative conclusions about the rigidity spectrum of the anisotropy from the present analysis which assumes a priori a flat spectrum with the upper limiting rigidity P_u fixed at 100 GV. Each value of ratios (βs) described above, for instance, changes for different value of P_u. The rigidity dependences of $\xi_\parallel$, $\xi_\perp$ and ξ_z relative to each other, however, remain unchanged even for different value of P_u (see Appendix C). I will discuss the physical origin of these rigidity dependences in the next section.

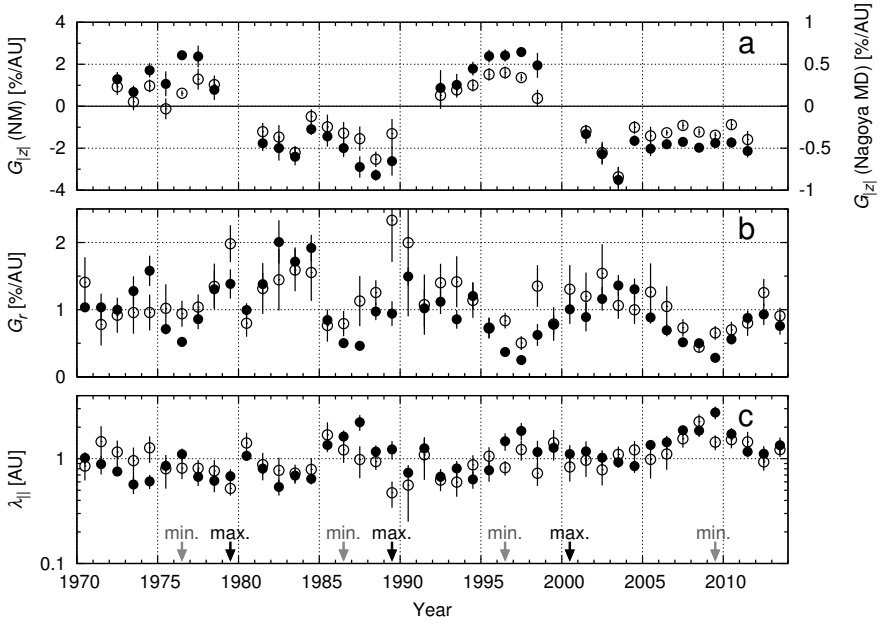

Figure 22: Modulation parameters derived from the three dimensional anisotropy. Each panel from top to bottom displays the yearly mean $G_{|z|}$, G_r and $\lambda_{\|}$, each as a function of year. Solid circles display parameters derived from Nagoya MD data at 60 GV, while open circles show parameters derived from NM data at 17 GV. Note that the bidirectional latitudinal density gradient ($G_{|z|}$) in the top panel is defined to be positive (negative) when the spatial distribution of GCR density has a local minimum (maximum) on the HCS. $G_{|z|}$ and G_r in the top and middle panels are plotted on the vertical axis in linear scales, while $\lambda_{\|}$ in the bottom panel is plotted in a logarithmic scale. Yearly mean and error are deduced from the mean and dispersion of monthly mean values, respectively. Because of the definition in equation (98), $G_{|z|}$ is not available in a year when the polarity reversal is in progress. (Munakata et al., 2014)

4.5.4 Modulation parameters

For R_L for Nagoya MD and NM data, I use gyro-radii of 60 GV and 17 GV GCRs, respectively, in the monthly mean IMF with the magnitude calculated from the OMNI data as described in Section 4.3.

Figure 22 shows the temporal variations of the calculated modulation parameters, $G_{|z|}$, G_r and $\lambda_{\|}$. Clearly seen in Figure 22a is that the bidirectional latitudinal density gradient ($G_{|z|}$) is positive (indicating the local minimum of density on the HCS) in $A > 0$ epoch, while it is negative (indicating the local maximum of density on the HCS) in $A < 0$ epoch, in accord with the drift model prediction (Kóta & Jokipii, 1983). There is no clear signature of an 11-year variation in $G_{|z|}$. The 22-year variation of $G_{|z|}$ appears cleaner and statistically more significant with relatively smaller errors in Nagoya MD data than in NM data. The mean $G_{|z|}$ derived from Nagoya MD (NM) data is 0.42±0.05 (0.86±0.14) %/AU in $A > 0$, while it is -0.52±0.04 (-1.47±0.15) %/AU, indicating that the magnitude of $G_{|z|}$ is larger in $A < 0$ than in $A > 0$ in both Nagoya MD and NM data.

The radial density gradient (G_r) in Figure 22b, on the other hand, varies with $\sim$ 11-year solar activity cycle with maxima (minima) in solar maximum (minimum) periods (Chen & Bieber, 1993; Bieber & Chen, 1991; Bieber & Pomerantz, 1986), but there is no significant difference seen between mean G_rs in $A > 0$ and $A < 0$ epochs. The mean G_r deduced from Nagoya MD (NM) data is 0.89±0.11 (1.04±0.08) %/AU in $A > 0$ epoch, while it is 0.99±0.12 (1.13±0.10) %/AU in $A < 0$ epoch. It is noted that there is a poor correlation between temporal variations of $G_{|z|}$ and G_r in both NM and muon data.

The parallel mean free path ($\lambda_{\|}$) in Figure 22c also changes with the solar activity cycle with minima (maxima) in solar maximum (minimum) periods. The mean $\lambda_{\|}$ deduced from Nagoya MD (NM) data is 0.90±0.10 (0.89±0.06) AU in $A > 0$, while it is 1.32±0.13 (1.14±0.10) AU in $A < 0$. This indicates that the mean $\lambda_{\|}$ is systematically larger in $A < 0$ than in $A > 0$ at 2 or 3

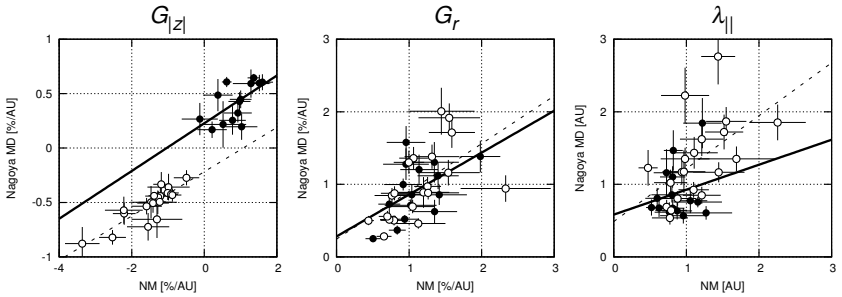

Figure 23: Correlation plots between modulation parameters derived from NM data at 17 GV and Nagoya MD data at 60 GV. The left, middle and right panels show correlations of $G_{|z|}$, G_r and $\lambda_{\parallel}$, respectively. Each panel displays the parameter in Figure 22 derived from Nagoya MD data at 60 GV on the vertical axis as a function of the parameter derived from NM data at 17 GV in the same year on the horizontal axis. Solid and open circles in each panel display parameters in $A > 0$ and $A < 0$ epochs, respectively. Data points in years when the polarity reversal is in progress are omitted in this figure. (Munakata et al., 2014)

sigma level. It is also interesting that $\lambda_{\parallel}$s in NM and Nagoya MD data appear like persistently increasing toward maxima in 2008 and 2009 during the last three solar activity cycles, while G_rs look like decreasing. The parallel mean free path ($\lambda_{\parallel}$) deduced from NM data (open circles) shows peaks in 1985 and 2008 in $A < 0$ solar minimum epochs, while it shows smaller peaks in 1974 and 1997 in $A > 0$ solar minimum epochs. This is qualitatively consistent with results reported in Chen & Bieber (1993). In $\lambda_{\parallel}$ deduced from Nagoya MD data (solid circles), on the other hand, the 11-year variation is more prominent with maxima in every solar minimum in 1976, 1987, 1997 and 2009, but no clear 22-year variation is visible in this figure. I will discuss long-term variations of G_r and $\lambda_{\parallel}$ in more detail in the next subsection.

I now discuss the rigidity dependence of each modulation parameter. Figure 23 shows the correlation between the parameters derived from NM data at 17 GV and from Nagoya MD data at 60 GV. In $A > 0$ ($A < 0$) epoch, $G_{|z|}$ from NM and Nagoya MD data in the left panel shows a good correlation with r of 0.63 (0.86), while the average ratio ($\beta = y/x$) of $G_{|z|}$ from Nagoya MD data to that from NM data is 0.48±0.10 (0.35±0.05) in $A > 0$ ($A < 0$) epoch indicating that $G_{|z|}$ decreases with increasing P_m. Also similar but weaker correlations are seen in G_r and $\lambda_{\parallel}$ in the middle and right panels with the average r of 0.53 (0.58) and 0.21 (0.54), respectively, while βs of G_r and $\lambda_{\parallel}$ are 0.85±0.12 (0.87±0.13) and 1.00±0.13 (1.16±0.15), respectively, indicating that these parameters are almost independent of P_m. Note that β of $G_{|z|}$ is significantly smaller than β of G_r indicating the softer rigidity dependence of $G_{|z|}$ than that of G_r, when P_u is fixed at 100 GV. The ratio βs derived from different P_u are listed in Table 5 in Appendix C.

I finally discuss the physical origin of the rigidity dependences of anisotropy components presented in the preceding section. As expressed in equations (95)-(97), $\xi_{\perp}$ and ξ_z include contributions from the diamagnetic drift added to the perpendicular diffusion, while $\xi_{\parallel}$ results solely from the parallel diffusion. By using G_r, $G_{|z|}$ and $\lambda_{\parallel}$ on an assumption of $\lambda_{\perp} = \alpha\lambda_{\parallel} = 0.01\lambda_{\parallel}$, I calculate individual contributions from the diffusion and drift to each of $\xi_{\perp}$ and ξ_z. I find that the average diffusion contribution ($\lambda_{\perp} G_r \sin\psi$) to $\xi_{\perp}$ is significantly smaller than the average drift contribution ($-R_L G_z$) in both NM and Nagoya MD data, hence $\xi_{\perp}$ is mainly arising from the drift effect. The average ratio of $|\lambda_{\perp} G_r \sin\psi|$ to $|-R_L G_z|$ contributing to $\xi_{\perp}$ is 0.08±0.02 in NM data, while the ratio is 0.07±0.02 in Nagoya MD data indicating that the average contribution from the diffusion to $\xi_{\perp}$ is less than 10 % in both NM and Nagoya MD data independent of P_m. The average ratio of the diffusion ($|\lambda_{\perp} G_z|$) to the drift ($|R_L G_r \sin\psi|$) contributing to ξ_z is also small as 0.03±0.01 in Nagoya MD data. The ratio in NM data, on the other hand, is 0.19±0.03 and significantly larger than the ratio in Nagoya MD data, indicating that the relative contribution of the diffusion to ξ_z increases with decreasing P_m. This is due to the rigidity dependence of $G_{|z|}$, which is softer than that of G_r as discussed above. Since there is only a poor correlation between temporal variations of $G_{|z|}$ and G_r in Figure 22, this may explain the poor correlation between ξ_zs by NM and Nagoya MD data which is shown in the bottom panel of Figure 21 and discussed in the preceding section.

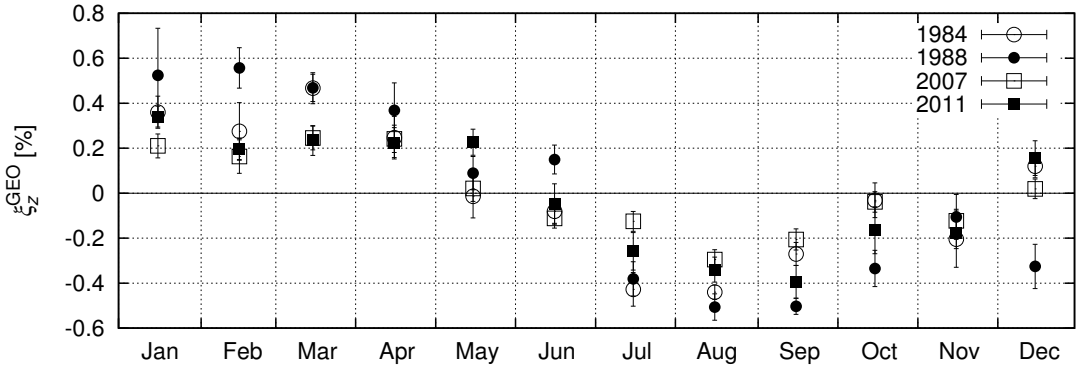

Figure 24: Seasonal variations of the monthly mean NS anisotropies in 1984 (open circle), 1988 (solid circle), 2007 (open square), and 2011 (solid square), as a function of the month indicated by the labels below the horizontal axis.

4.6 Summary and discussion of the solar cycle variation

In Sections 4.1 to 4.4, I compared the 3D anisotropy and modulation parameters (i.e. mean free path and density gradient of GCRs) derived from the GMDN and Nagoya MD data during 1992 - 2013. By analyzing the distribution of the NS anisotropy separately in *toward* and *away* IMF sectors, I confirmed that the hourly mean NS anisotropy by the GG-component shows a large spread due to the local time dependent contribution from the ecliptic anisotropy. The NS anisotropy by the GMDN, on the other hand, shows similar success rate on both daily and hourly bases, indicating that the NS anisotropy is successfully observed by the GMDN, free from the contribution of the ecliptic anisotropy. I also find that the NS anisotropy increases with increasing rigidity in accord with Yasue (1980). I found three NS anisotropies observed with NMs in ~ 17 GV, with GMDN in ~ 60 GV, and with GG-component in ~ 80 GV increasing in this order.

I confirmed that the solar cycle variations of the 3D anisotropy and modulation parameters derived from the GMDN and Nagoya MD data are consistent with each other as far as yearly mean values are concerned. This fact is important particularly for the NS anisotropy derived from the GMDN data, because the GG-component has been the only reliable reference of the NS anisotropy in the rigidity region 50 – 100 GV. A seasonal variation of the GG-component which indicates a contribution from the co-rotation anisotropy was also found. Figure 24 shows monthly mean NS anisotropies in the years 1984, 1988, 2007, and 2011, around which phases of the diurnal anisotropies are almost constant for several years at $\sim$ 18:00 local solar time in an agreement with the co-rotation anisotropy, as seen in the bottom panel of Figure 20. In Figure 24, the monthly mean NS anisotropy $\xi_z^{\rm GEO}$ is calculated as

$$\xi_z^{\rm GEO} = \left(\xi_z^{{\rm GEO}(T)} + \xi_z^{{\rm GEO}(A)}\right)/2 \tag{122}$$

where $\xi_z^{{\rm GEO}(T)}$ ($\xi_z^{{\rm GEO}(A)}$) is the NS anisotropy derived from the GG-component by equation (82) and averaged over the *toward* (*away*) IMF sectors in each month. This NS anisotropy represents the portion of the anisotropy common for both of the IMF sectors, while the NS anisotropy derived in equation (93) represents the difference between the sectors. The coupling coefficient $c^0_{1,GG}$ in equation (82) is derived by assuming the upper limiting rigidity $P_u = 100$ GV, i.e. given by the row of $P_u = 100$ GV in Table 2. We can see a seasonal variation of the NS anisotropy with a maximum around the spring (February in 1988 and March in 1984, 2007, and 2011) and a minimum around the fall (August in 1984, 1988, and 2007 and September in 2011). This is roughly consistent with the GEO-z (parallel to the earth's rotation axis) component of the co-rotation (anti-parallel to the earth's orbital motion, i.e. GSE-y) anisotropy, which has a positive (northward) maximum in March and a negative (southward) maximum in September if it is constant for a year.

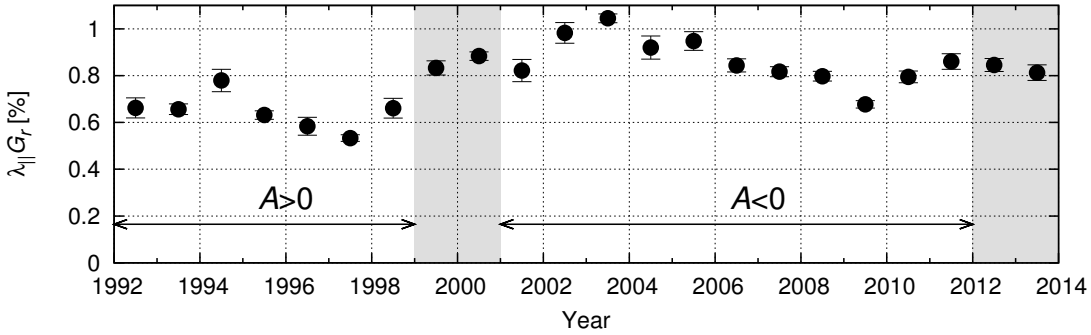

Figure 25: Long-term variation of $\lambda_{\parallel}G_r$ derived from the GMDN data. Yearly mean value and its error are deduced from the average and dispersion of monthly mean values. Gray vertical stripes indicate periods when the polarity reversal of the solar polar magnetic field (referred as $A > 0$ or $A < 0$) is in progress. (Kozai et al., 2014)

I find that the bi-directional latitudinal gradient $G_{|z|}$ shows a clear 22-year variation being positive (negative) in $A > 0$ ($A < 0$) epochs indicating the local minimum (maximum) of the GCR density on the HCS, in accord with the prediction of the drift model (Kóta & Jokipii, 1983). On the other hand, G_r and $\lambda_{\parallel}$ show significant 11-year variations in an anti-correlation with each other, in accord with the force-field model represented by equation (14), i.e. the radial convection-diffusion equilibrium without drift effect. The north-south anisotropy (ξ_z) also shows an 11-year cycle variation in a positive correlation with solar activity.

The ecliptic component of the anisotropy ($\xi_{\parallel}$) parallel to the IMF shows a 22-year variation being slightly larger in $A < 0$ epoch (2001-2011) than in $A > 0$ epoch (1992-1998) as reported by Chen & Bieber (1993). This variation of $\xi_{\parallel}$ is responsible to the well known 22-year variation of the phase of the diurnal variation (Thambyahpillai & Elliot, 1953). I find that the variation of $\xi_{\parallel}$ also shows a correlation with the $\cos\psi$ which is governed by the solar wind velocity. This is reasonable because $\xi_{\parallel}$ is proportional to $\cos\psi$ as given in equation (95). Figure 25 shows yearly variation of $\xi_{\parallel}/\cos\psi$, i.e. $\lambda_{\parallel}G_r$ by the GMDN. In this figure, the 22-year variation is seen more clearly than in Figure 15 showing $\xi_{\parallel}$ (Chen & Bieber, 1993). For an accurate analysis of the solar cycle variation of the anisotropy, therefore, it is necessary to correct the observed variation of $\xi_{\parallel}$ for variations of $\cos\psi$ and the solar wind velocity which vary without any clear 11-year or 22-year periodicities.

After confirming that the combination analysis of the diurnal variation and GG-component of Nagoya MD provides a reliable 3D anisotropy being consistent with the GMDN observations on yearly basis, I analyzed the long-term variations of the anisotropy and modulation parameters over 44 years in Section 4.5 by expanding the analysis period back to 1970's when Nagoya MD started the operation. The solar cycle variations of the anisotropy and modulation parameters, mentioned above, are confirmed by this analysis covering 4 solar activity cycles.

By also analyzing the data recorded during the same period by NMs (Swarthmore/Newark, Alert/Thule and McMurdo) which have median responses to ~ 17 GV primary GCRs, I examined the rigidity dependences of the anisotropy and modulation parameters. Figure 26 shows the temporal variation of $\lambda_{\parallel}G_r = \xi_{\parallel}/\cos\psi$. Clearly seen is that the mean magnitude of $\lambda_{\parallel}G_r$ is significantly smaller in $A > 0$ (solid circles) than in $A < 0$ periods (open circles). The mean magnitude of $\lambda_{\parallel}G_r$ derived from Nagoya MD data and that from and NM data in $A < 0$ epoch are 1.07±0.03 and 1.14±0.02, respectively, being fairly consistent with each other, while the mean magnitudes in $A > 0$ periods are 0.68±0.04 % and 0.89±0.05 %, respectively. I also note that the ratio of $\lambda_{\parallel}G_r$ for Nagoya MD to that for NM data is smaller in $A > 0$ than in $A < 0$ periods, indicating the softer rigidity spectrum of this component for $A > 0$ than for $A < 0$. This larger decrease of $\lambda_{\parallel}G_r$ in $A > 0$ epoch in Nagoya MD data than in NM data is responsible to the larger phase shift of the diurnal anisotropy in $A > 0$ solar minimum epoch in Nagoya MD data. The harder rigidity spectrum of $\xi_{\perp}$ than that of $\xi_{\parallel}$ mentioned previously is also partly responsible to

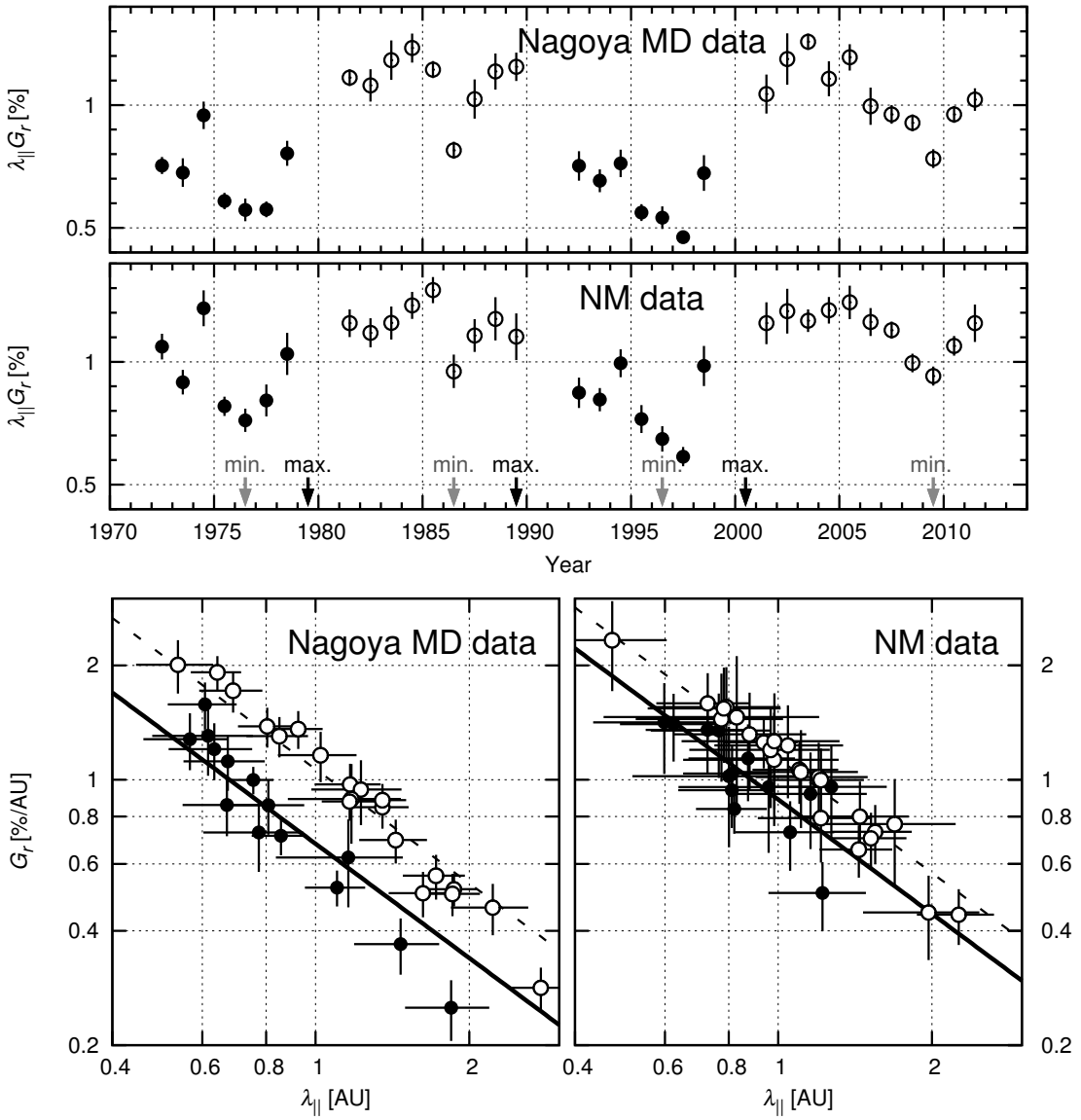

Figure 26: Temporal variation of $\lambda_\parallel G_r$ and the correlation between G_r and $\lambda_\parallel$. Upper two panels display yearly mean $\lambda_\parallel G_r$ calculated from $\xi_\parallel / \cos\psi$, each as a function of year. Top panel shows $\lambda_\parallel G_r$ deduced from Nagoya MD data, while middle panel shows $\lambda_\parallel G_r$ deduced from NM data. Yearly mean values in $A > 0$ ($A < 0$) epoch are displayed by solid (open) circles, each with an error deduced from the dispersion of monthly values in each year. Data points in years when the polarity reversal is in progress are omitted in this figure. Bottom two panels are scatter plots between G_r and $\lambda_\parallel$ in logarithmic scales derived from Nagoya MD data (left) and NM data (right). In each panel, yearly mean G_r on the vertical (y) axis is plotted as a function of $\lambda_\parallel$ on the horizontal (x) axis. Solid and dashed straight lines display the functions $y = c/x$ with a constant parameter c best-fit to data in $A > 0$ and $A < 0$ epochs, respectively. (Munakata et al., 2014)

the larger phase shift in Nagoya MD data in $A > 0$ minimum epochs. Hall et al. (1997) used the NM and Nagoya MD data for analyzing the rigidity spectrum of the diurnal anisotropy and obtained the average $G(P)$ proportional to $P^{-0.1\pm0.2}$ with $P_u = 100 \pm 25$ GV. Although their spectrum seems to be consistent with $G(P)$ assumed in this thesis, such a common spectrum for $\xi_\parallel$ and $\xi_\perp$ cannot reproduce the observed feature that the phase shift observed by Nagoya MD in $A > 0$ solar minimum epoch is significantly larger than that by NM.

The average ratio between $\xi_\parallel$s in Nagoya MD and that in NM data is roughly consistent with a rigidity independent spectrum, while the rigidity spectrum of $\xi_\parallel$ is systematically softer in $A > 0$ than in $A < 0$. On the other hand, $\xi_\perp$ and ξ_z derived from Nagoya MD data are significantly larger than those from NM data, indicating that these components increase with P_m. According to equations (95)-(97), $\xi_\perp$ and ξ_z include contributions from the diamagnetic drift added to perpendicular diffusion, while $\xi_\parallel$ is caused by the parallel diffusion alone. It is reasonable, therefore, to expect that the observed harder rigidity spectra of $\xi_\perp$ and ξ_z are due to effects from the drift. Based on numerical simulations of particle propagation in turbulent magnetic field, Minnie et al. (2007) has shown that drifts are suppressed by magnetic turbulence, but the suppression sets in at lower turbulence amplitudes for low-energy than for high-energy cosmic rays. This may give a possible explanation for why the contribution of drift streaming results in a harder rigidity spectrum. If this is the case, we may well need two different spectra, representing diffusion and drift, combined in $\xi_\perp$ and ξ_z, to reproduce the correct rigidity dependence of the diurnal anisotropy in space.

Equations (95)-(97) also imply that the drift contribution to $\xi_\perp$ is proportional to $G_{|z|}$, while the drift contribution to ξ_z is proportional to G_r. By comparing G_r and $G_{|z|}$ derived from NM and Nagoya MD data, I find that the rigidity dependences of G_r and ξ_z are harder than those of $G_{|z|}$ and $\xi_\perp$ (Yasue, 1980; Hall et al., 1994).

The 11-year variation is evident in the radial density gradient (G_r) in Figure 22, while we cannot identify a clear 22-year variation which should make the 22-year variation of $\lambda_\parallel G_r$ in the drift model prediction (Levy, 1976; Erdös & Kóta, 1980; Kóta & Jokipii, 1983; Potgieter & Moraal, 1985). The mean G_r deduced from Nagoya MD (NM) data is 0.89±0.11 (1.04±0.08) %/AU in $A > 0$ epoch, while it is 0.99±0.12 (1.13±0.10) %/AU in $A < 0$ epoch. The mean parallel mean free path ($\lambda_\parallel$), on the other hand, turns out to be significantly larger in the $A < 0$ than in the $A > 0$ epochs, in the both Nagoya MD and NM data. I find that the mean $\lambda_\parallel$ deduced from Nagoya MD (NM) data is 0.90±0.10 (0.89±0.06) AU in $A > 0$, while it is 1.32±0.13 (1.14±0.10) AU in $A < 0$. Chen & Bieber (1993) suggested that the 22-year variation of $\lambda_\parallel$ is responsible for the reduction of $\lambda_\parallel G_r$ in $A > 0$ and for the 22-year variation of the diurnal anisotropy. The two bottom panels of Figure 26 show the correlation between G_r and $\lambda_\parallel$ (both in logarithmic scale) on the vertical (y) and horizontal (x) axes, respectively. Since $\lambda_\parallel$ on the x-axis is deduced from $\lambda_\parallel G_r$ divided by G_r on the y-axis, data points in this scatter plot align on a straight line when $\lambda_\parallel G_r$ is constant during the analysis period. Solid and dashed straight lines in each panel display functions of $y = c/x$ best-fitting to data in $A > 0$ and $A < 0$ epochs, respectively, each with the intercept c as a best-fit parameter. It is seen that, for the Nagoya MD data (left panel) the best-fit c for $A > 0$ data (solid circles) is about 64 % of that for the $A < 0$ data (open circles). This is consistent with the lower $\lambda_\parallel$ value derived from Nagoya MD data for $A > 0$ epochs which is 68 % (=0.90/1.32) of that in $A < 0$ epoch, indicating that the 22-year variation of $\lambda_\parallel G_r$ in the left panel is due to the 22-year variation of $\lambda_\parallel$ on the horizontal axis.

However, I also find in Figure 22 that $\lambda_\parallel$s (G_rs) from NM and Nagoya MD data appear to persistently increase (decrease) during the last three solar activity cycles reaching maximum (minimum) in 2008-2009. Figure 27 displays the mean G_r and $\lambda_\parallel$ in $A > 0$ and $A < 0$ epochs, each as a functions of time. It is clear particularly in the Nagoya MD data (left panels) that there are long-term trends indicated by a best-fit solid line in each panel. The solar magnetic field was unusually weak around this last solar minimum (2009), which resulted in the weakest magnetic field (McComas et al., 2008) and a record-high GCR flux (Mewaldt et al., 2010). The larger $\lambda_\parallel$ (smaller G_r) in the last solar minimum is likely the result of the weaker solar minimum. This trend enhances the difference between $A > 0$ and $A < 0$ means of $\lambda_\parallel$, while it reduces the difference between means of G_r as seen in Figure 27. The simple means of G_r or $\lambda_\parallel$ in all $A > 0$

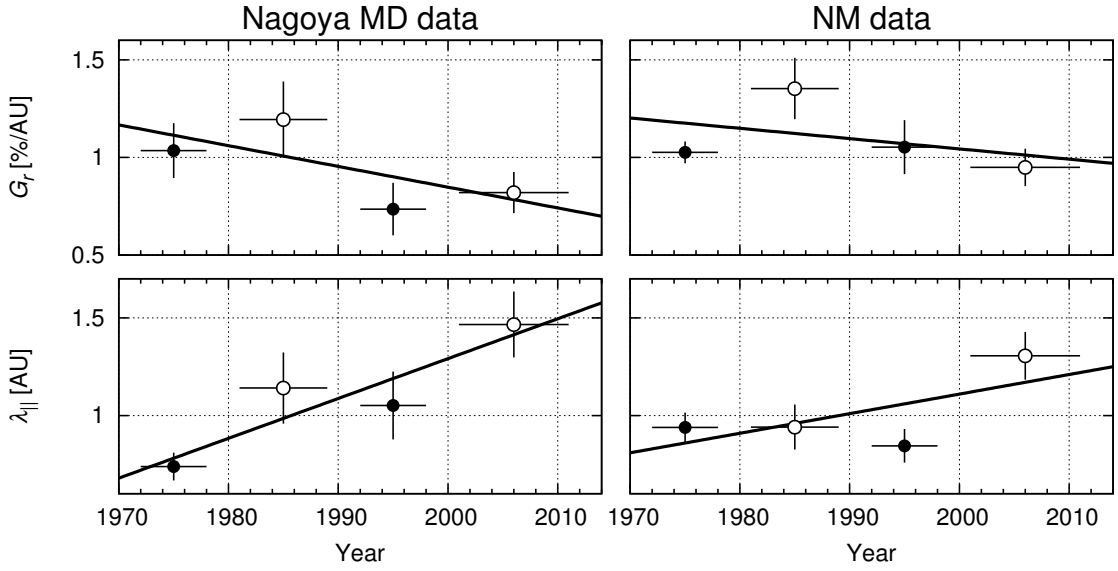

Figure 27: Long-term trends of mean G_r and $\lambda_{\parallel}$ in each solar magnetic polarity epoch. Left (right) two panels display means derived from Nagoya MD (NM) data. Means in $A > 0$ and $A < 0$ epochs are plotted by solid and open circles, respectively, at the central year of each epoch. The vertical error is deduced from the dispersion of yearly means in each epoch, while the horizontal bar indicates the period included in each epoch. Solid straight line in each panel displays the linear long-term trend best-fit to four data points. (Munakata et al., 2014)

and $A < 0$ epochs are, therefore, seriously biased by these long term trends. If we look at the deviation of each data point from the solid line in the Nagoya MD data, we find that G_r and $\lambda_{\parallel}$ are both larger (smaller) in $A < 0$ ($A > 0$) epoch, although only at one sigma level.

The dynamic range of $\lambda_{\parallel}$ (or G_r) due to the 11-year variation in the lower panels of Figure 26 is close to an order of magnitude and much larger than the 22-year variation. Small signature of its 22-year variation can be easily masked by the 11-year variation with much larger amplitude. Also simple means of $\lambda_{\parallel}$ and G_r in $A > 0$ and $A < 0$ epochs may be seriously biased by their long term trends as seen above.

5 Summary and conclusions

The traditional analyses of single MD or NM data described in Secion 4.1 provide the GCR anisotropy separately from the isotropic intensity (or GCR density) only on a daily or longer time basis, by assuming the GCR density and anisotropy almost constant over a day. Only a worldwide detector network allows us to separately observe the GCR density and anisotropy on a shorter time basis. In this thesis, I analyzed hourly variations of the GCR density distribution by analyzing the Global Muon Detector Network (GMDN) data.

The high temporal resolution of the three-dimensional (3D) anisotropy observed with the GMDN allows us to infer the spatial structure of the GCR depleted region formed behind the interplanetary shock (IP-shock) which causes a short-term density decrease (called Forbush Decreases; FDs) on its arrival at the earth. By analyzing FDs following the IP-shocks generated by the solar eruptions (such as coronal mass ejections; CMEs) from various heliographic locations on the sun, I derived the 3D average distribution of GCRs in the depleted region for the first time. An east-west asymmetric distribution, which has been predicted by a magnetic configuration model of the shock, was confirmed with the observed density gradient suggesting a density minimum in an expanding CME propagating radially outward from the eruption location on the sun. The FDs observed simultaneously by the neutron monitors (NMs) and the GMDN, which are sensitive to $\sim$ 10 GV and $\sim$ 60 GV GCRs, respectively, showed a soft rigidity spectrum of the FD.

I also analyzed year-to-year variations of the 3D anisotropy using the GMDN for the first time. In former works analyzing a single detector or a pair of detectors data in a traditional way, diurnal and NS anisotropies were derived on a daily basis from separate analyses. The GMDN, on the other hand, provides us with the anisotropy in three dimensions from a single analysis on an hourly basis. I confirmed that the NS anisotropy is more accurately derived from the analysis of the GMDN data than from the traditional analyses, while results obtained from two analyses are fairly consistent with each other as far as the yearly mean value is concerned.

The first order anisotropy observed with the GMDN from 1992 to 2013 shows a variation in a correlation with the solar activities. I found that the anisotropy component parallel to the IMF in the ecliptic plane shows a 22-year cycle variation which is responsible to the well-known 22-year variation of the phase of the diurnal anisotropy. The north-south density gradient normal to the ecliptic plane indicates a local density maximum on the heliospheric current sheet (HCS) in $A < 0$ epoch while it indicates a local minimum along the HCS in $A > 0$ epoch, in agreement with the drift model prediction. The radial density gradient, on the other hand, does not show a clear 22-year variation predicted by the drift model, while it shows a significant 11-year variation. The parallel mean free path of the pitch angle scattering of GCRs also shows a significant 11-year variation out of phase with the radial gradient, in accord with the force-field model of the GCR modulation based on the equilibrium between the radial diffusion and solar wind convection without drift effect. The mean free path has an average magnitude of $\sim$ 1 AU for $\sim$ 60 GV GCRs which is also comparable to the numerical simulation of the pitch angle scattering.

In addition to the GMDN data, I also analyzed GCR anisotropies observed with a single MD at Nagoya and NMs over 44 years from early 1970's to 2013. The 3D anisotropy is derived from the observed diurnal anisotropy combined with the NS anisotropy deduced from the GG-component. From the long-term variation over 4 solar activity cycles, I found a small 22-year variation of the radial gradient, which is masked by a larger 11-year variation and by a persistent long-term trend over the last several solar cycles. It was also found that the anisotropy parallel to the IMF, i.e. the parallel diffusion streaming of GCRs, has a flat rigidity spectrum, while the perpendicular anisotropy mainly arising from the drift streaming has a harder spectrum.

Acknowledgement

First of all, I'm very grateful to Prof. Kazuoki Munakata for his kind guidance over my study and student life. In the doctoral thesis examination, I was provided with helpful advises by Prof. Toru Takeshita, Prof. Yoji Hasegawa, Prof. Chihiro Kato, and Prof. Munetoshi Tokumaru in Nagoya University. I'm very thanful to them.

I really appreciate Dr. Takao Kuwabara for his kindly instructing me in the cosmic ray data analysis and MD observation system. Dr. Akira Fushishita and Mr. Naoto Morishida also gave me many advises over the data analysis, observation system, and student life. I'm very thankful to them. I'm also grateful to Prof. Shinichi Yasue for his lectures on the observation system.

I'm very thankful to the GMDN collaborators for their kind helps for my GMDN data analysis and paper submissions. I'm specially thankful to Prof. Marcus L. Duldig, Prof. John E. Humble, and Mr. Keith Bolton for their hospitality and support for my work with the Hobart MD. I also would like to appreciate Prof. Hala K. Al Jassar, Prof. Madan M. Sharma, Dr. Djenane Khalil, and other staffs of Kuwait University for their kindly supporting my works with the Kuwait MD.

During my participation to the International Cosmic Ray Conference (ICRC) at Rio de Janeiro, Brazil, Prof. Alisson Dal Lago, Prof. Nelson J. Schuch, and Dr. Marlos Rockenbach gave me warm hospitalities. I'm very thankful to them. I also appreciate Dr. Rafael Rodrigues Mendonça and Dr. Carlos Roberto Braga for their friendly hospitalities during the ICRC and discussions during their stay in Shinshu University.

I would like to thank Prof. Paul Evenson for his advises and discussions on the cosmic ray experiments during the ICRC and his visit to Shinshu University. On the interpretations of the observed GCR anisotropy, I received many advises from Prof. József Kóta of the University of Arizona. I appreciate him. I would like to thank Prof. Manabu Shinohara in NIT, Kagoshima College for his advises on analyses of the IP-shock events.

The cosmic ray detectors used in this research have been kept in operation also by other people which include Mr. Morikazu Koyama in Shinshu University and many staffs of Nagoya University, the University of Tokyo, University of Delaware, and so on. I would like to appreciate all of them. I also appreciate my student colleagues in Shinshu University; Mr. Yuu Mizoguchi, Mr. Tomoaki Masakawa, Mr. Akimasa Ishizaki, Mr. Takaaki Nakajima, Mr. Takenori Niwa, Mr. Yoshiaki Nakamura, and so on.

Finally I'm very grateful to my parents for their patient supports to my long student life.

Appendix

A GMDN data analysis

The term of $I_0(t)$ in equation (48) is approximately rewritten by including the rigidity dependence (Kuwabara, 2005), as

$$I_0(t)c^0_{0i,j} = I^{\rm com}_{0i}(t) + I^r_0(t)\frac{P_{mi,j}}{P_{m1,1}} \tag{123}$$

where $I^{\rm com}_{0i}(t)$ is the rigidity-independent portion of the density and $I^r_0(t)$ represents the rigidity dependence. $P_{mi,j}$ is the median primary rigidity of the j-th directional channel of the i-th detector, defined by equation (38), while $P_{m1,1}$ denotes that of the vertical channel ($j = 1$) of Nagoya MD ($i = 1$). I write down $I^{\rm com}_{0i}(t)$ as depending on the station, i, because it possibly includes a contribution from the atmospheric temperature variation, which is approximately common for all the directional channels (js) of the i-th detector (Appendix B of Okazaki et al., 2008). The coupling coefficient $c^0_{0i,j}$ is omitted because of $c^0_{0i,j} = 1$ for the upper limiting rigidity set at $P_u = 10^5$ GV. The model function (48) of fractional deviation of the pressure corrected muon count rate is rewritten as

$$\begin{aligned} I^{fit}_{i,j}(t) = I^{\rm com}_{0i}(t) + I^r_0(t)\frac{P_{mi,j}}{P_{m1,1}} + \xi^{\rm GEO}_x(t)\left(c^1_{1i,j}\cos\omega t_i - s^1_{1i,j}\sin\omega t_i\right) + \\ \xi^{\rm GEO}_y(t)\left(s^1_{1i,j}\cos\omega t_i + c^1_{1i,j}\sin\omega t_i\right) + \xi^{\rm GEO}_z(t)c^0_{1i,j}. \end{aligned} \tag{124}$$

A.1 V-subtraction method

This analysis method deriving a "day-by-day" variation of the anisotropy was first developed by Okazaki et al. (2008). In order to correct the temperature effect, I subtract a fractional deviation ($I_{i,1}$) of the vertical channel count rate from that ($I_{i,j}$) of the j-th directional channel in each detector, i, as

$$\Delta I_{i,j}(t) = I_{i,j}(t) - I_{i,1}(t). \tag{125}$$

The model function of $\Delta I_{i,j}(t)$ is given as

$$\begin{aligned} \Delta I^{fit}_{i,j}(t) = I^r_0(t)\frac{\Delta P_{mi,j}}{P_{m1,1}} + \xi^{\rm GEO}_x(t)\left(\Delta c^1_{1i,j}\cos\omega t_i - \Delta s^1_{1i,j}\sin\omega t_i\right) + \\ \xi^{\rm GEO}_y(t)\left(\Delta s^1_{1i,j}\cos\omega t_i + \Delta c^1_{1i,j}\sin\omega t_i\right) + \xi^{\rm GEO}_z(t)\Delta c^0_{1i,j} \end{aligned} \tag{126}$$

where

$$\Delta P_{mi,j} = P_{mi,j} - P_{mi,1}, \tag{127}$$
$$\Delta c^m_{ni,j} = c^m_{ni,j} - c^m_{ni,1}, \tag{128}$$
$$\Delta s^m_{ni,j} = s^m_{ni,j} - s^m_{ni,1}. \tag{129}$$

I define the residual $\chi^2_{\rm V}$, as

$$\chi^2_{\rm V} = \sum_{i=1}^{4}\sum_{j=1}^{n_i}\frac{\left(\Delta I_{i,j} - \Delta I^{fit}_{i,j}\right)^2}{\sigma^2(\Delta I_{i,j})} \tag{130}$$

where n_i is a number of directional channels in the i-th detector and

$$\sigma^2(\Delta I_{i,j}) = \sigma^2(I_{i,j}) + \sigma^2(I_{i,1}). \tag{131}$$

From equation (48), the statistical error $\sigma(I_{i,j})$ is derived from the muon count rate $N_{i,j}$ of the j-th directional channel of the i-th detector, as

$$\sigma(I_{i,j}) = \frac{\sqrt{N_{i,j}}}{\langle N_{i,j}\rangle} \sim \frac{1}{\sqrt{N_{i,j}}}. \tag{132}$$

The best-fit parameters, I_0^r, $\xi_x^{\rm GEO}$, $\xi_y^{\rm GEO}$, and $\xi_z^{\rm GEO}$, which minimize the residual $\chi^2_{\rm V}$ are derived on an hourly basis by solving equations,

$$\frac{\partial(\chi^2_{\rm V})}{\partial I_0^r} = \frac{\partial(\chi^2_{\rm V})}{\partial \xi_x^{\rm GEO}} = \frac{\partial(\chi^2_{\rm V})}{\partial \xi_y^{\rm GEO}} = \frac{\partial(\chi^2_{\rm V})}{\partial \xi_z^{\rm GEO}} = 0. \tag{133}$$

This analysis method, V-subtraction method, has a drawback that the obtained anisotropy has a large statistical error due to the subtraction of count rates in equation (125), as represented by equation (131), insufficiently for deriving an accurate anisotropy on an hourly basis. I therefore extract only the "day-by-day" variations by taking 24 hours trailing moving averages of the obtained parameters, as

$$\overline{I_0^r}(t) = \frac{1}{24}\sum_{\tau=t-23}^{t} I_0^r(\tau), \tag{134}$$

$$\overline{\xi^{\rm GEO}_{x,y,z}}(t) = \frac{1}{24}\sum_{\tau=t-23}^{t} \xi^{\rm GEO}_{x,y,z}(\tau). \tag{135}$$

A.2 Normalization method

This analysis method was first developed by Kuwabara et al. (2004) and Okazaki et al. (2008) added some modifications by combining the V-subtraction analysis. I normalize the fractional deviation ($I_{i,j}(t)$) of muon count rate to the 24 hours trailing moving average of the vertical channel count rate in Nagoya MD, $I_{1,1}(t)$, as

$$I^{\rm nor}_{i,j}(t) = \frac{\overline{I_{1,1}}(t)}{\overline{I_{i,j}}(t)} I_{i,j}(t) \tag{136}$$

where

$$\overline{I_{i,j}}(t) = \frac{1}{24}\sum_{\tau=t-23}^{t} I_{i,j}(\tau). \tag{137}$$

For the hours when the Nagoya MD data is unavailable, I use the 24 hours moving average $\overline{I_{1,3}}(t)$ of the vertical channel of São Martinho da Serra MD ($i = 3$), instead of $\overline{I_{1,1}}(t)$. The best-fit function (124) for $I^{\rm nor}_{i,j}(t)$ is written by replacing $I^{\rm com}_{0i}(t)$ with $I^{\rm com}_0(t)$ common for all detectors, as

$$\begin{aligned} I^{\rm nor(fit)}_{i,j}(t) &= I^{\rm com}_0(t) + I^r_0(t)\frac{P_{mi,j}}{P_{m1,1}} + \xi^{\rm GEO}_x(t)\left(c^1_{1i,j}\cos\omega t_i - s^1_{1i,j}\sin\omega t_i\right) + \\ &\quad \xi^{\rm GEO}_y(t)\left(s^1_{1i,j}\cos\omega t_i + c^1_{1i,j}\sin\omega t_i\right) + \xi^{\rm GEO}_z(t)c^0_{1i,j} \end{aligned} \tag{138}$$

because the contribution $I^{\rm com}_{0i}(t)$ from the day-by-day temperature variation in each station (i) is normalized to that of Nagoya or São Martinho da Serra station. It is noted that the contribution from the hourly temperature variation is assumed to be negligible, and the contributions from day-by-day variations of the density and NS anisotropy ($I_0(t)$ and $\xi_z^{\rm GEO}(t)$) are also eliminated by this normalization. I define the residual $\chi^2_{\rm nor}$, as

$$\chi^2_{\rm nor} = \sum_{i=1}^{4}\sum_{j=1}^{n_i} \frac{\left(I^{\rm nor}_{i,j} - I^{\rm nor(fit)}_{i,j}\right)^2}{\sigma^2(I_{i,j})}. \tag{139}$$

The best-fit parameters, $I^{\rm com}_0$, I^r_0, $\xi_x^{\rm GEO}$, $\xi_y^{\rm GEO}$, and $\xi_z^{\rm GEO}$, which minimize the residual $\chi^2_{\rm nor}$ are derived on an hourly basis by solving equations,

$$\frac{\partial(\chi^2_{\rm nor})}{\partial I^{\rm com}_0} = \frac{\partial(\chi^2_{\rm nor})}{\partial I^r_0} = \frac{\partial(\chi^2_{\rm nor})}{\partial \xi_x^{\rm GEO}} = \frac{\partial(\chi^2_{\rm nor})}{\partial \xi_y^{\rm GEO}} = \frac{\partial(\chi^2_{\rm nor})}{\partial \xi_z^{\rm GEO}} = 0. \tag{140}$$

I extract only the "high-frequency" variation of each parameter by removing 24 hours trailing moving average from the obtained parameter, as

$$\delta I_0^r(t) = I_0^r(t) - \frac{1}{24}\sum_{\tau=t-23}^{t} I_0^r(\tau), \tag{141}$$

$$\delta \xi_{x,y,z}^{\rm GEO}(t) = \xi_{x,y,z}^{\rm GEO}(t) - \frac{1}{24}\sum_{\tau=t-23}^{t} \xi_{x,y,z}^{\rm GEO}(\tau). \tag{142}$$

A.3 Derivation of GCR anisotropy and density

A combination analysis of the V-subtraction method and the normalization method (Okazaki et al., 2008) allows us to deduce properly the hourly variations of the rigidity dependent density $I_0^r(t)$ and the anisotropy $\boldsymbol{\xi}^{\rm GEO}(t)$, by combining the "high-frequency" variations derived by equations (141) and (142) with the "day-by-day" variations derived by equations (134) and (135), as

$$I_0^r(t) = \overline{I_0^r}(t) + \delta I_0^r(t), \tag{143}$$

$$\xi_{x,y,z}^{\rm GEO}(t) = \overline{\xi_{x,y,z}^{\rm GEO}}(t) + \delta \xi_{x,y,z}^{\rm GEO}(t). \tag{144}$$

The hourly variation of the density, $I_0(t)$, cannot be deduced from this analysis method because the rigidity-independent portion of the density, that is, the first term of the right hand side in equation (123), is eliminated in the best-fit function (126) in the V-subtraction analysis.

I introduce a new analysis method, therefore, to deduce the density variation $I_0(t)$. The fractional deviation $I_{i,j}(t)$ of the muon count rate is subtracted by the contributions from $I_0^r(t)$ and $\boldsymbol{\xi}^{\rm GEO}(t)$ obtained in the combination analysis, as

$$I_{i,j}^{\rm cor}(t) = I_{i,j}(t) - \Big\{ I_0^r(t)\frac{P_{mi,j}}{P_{m1,1}} + \xi_x^{\rm GEO}(t)\left(c_{1i,j}^1 \cos\omega t_i - s_{1i,j}^1 \sin\omega t_i\right) + \xi_y^{\rm GEO}(t)\left(s_{1i,j}^1 \cos\omega t_i + c_{1i,j}^1 \sin\omega t_i\right) + \xi_z^{\rm GEO}(t) c_{1i,j}^0 \Big\}. \tag{145}$$

From equation (124), this represents the rigidity-independent portion of the density, $I_{0i}^{\rm com}(t)$, containing the atmospheric temperature effect in the i-th station. I derive the rigidity-independent portion of the density, $I_0^{\rm com}(t)$, free from the temperature variation by taking a weighted average,

$$I_0^{\rm com} = \frac{\sum_{i=1}^{4}\sum_{j=1}^{n_i} w_{i,j} I_{i,j}^{\rm cor}}{\sum_{i=1}^{4}\sum_{j=1}^{n_i} w_{i,j}} \tag{146}$$

where $w_{i,j} = 1/\sigma^2(I_{i,j})$. The temperature effect on $I_0^{\rm com}$ is simply assumed to be almost averaged out in this average over all stations of the GMDN. A density variation of the GCRs with rigidity $P = P_{m1,1} \sim 60$ GV is derived as

$$I_0(t) = I_0^{\rm com}(t) + I_0^r(t). \tag{147}$$

By using the Global Forecast System (GFS) model[11] for the vertical distribution of high altitude atmospheric temperature, one year GMDN data in 2009 was corrected for the temperature effect on an hourly basis (Dr. V. Yanke, private communication). Figure 28 displays a histogram of the difference between the densities (panel (a)) or the anisotropy components (panels (b) to (d)) before and after the correction, that is,

$$\Delta I_0 = I_0 - I_0^{\rm GFS}, \tag{148}$$

$$\Delta \xi_{x,y,z}^{\rm GEO} = \xi_{x,y,z}^{\rm GEO} - \xi_{x,y,z}^{\rm GEO(GFS)} \tag{149}$$

where $I_0^{\rm GFS}$ ($\xi_{x,y,z}^{\rm GEO(GFS)}$) denotes the GCR density (anisotropy components) derived from the fractional deviation ($I_{i,j}(t)$) from each monthly average of the muon count rate corrected for the

[11] http://www.emc.ncep.noaa.gov

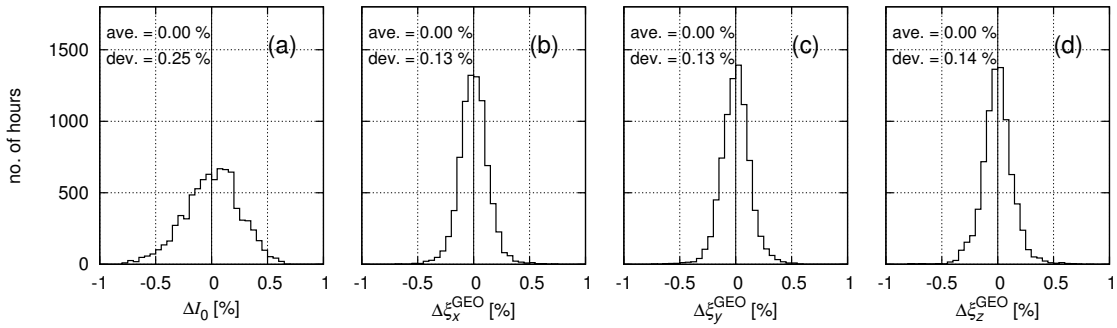

Figure 28: Histograms of the differences (ΔI_0 and $\Delta\xi^{\rm GEO}_{x,y,z}$) between (a) the densities (I_0 and $I_0^{\rm GFS}$) and (b-d) the anisotropy components ($\xi_{x,y,z}$ and $\xi^{\rm GEO(GFS)}_{x,y,z}$) derived from the GMDN data ($I_{i,j}(t)$s) in 2009 before and after the correction for the atmospheric temperature effect using the GFS model.

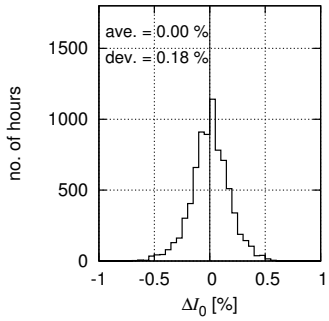

Figure 29: A histogram of the difference (ΔI_0) between fractional deviations of the densities (I_0 and $I_0^{\rm GFS}$) from the averages over each 5-days period in 2009.

atmospheric temperature by using the GFS model. Averages and deviations of the histograms are also indicated in this figure. All the histograms in Figure 28 show Gaussian-like distributions, with averages at 0.00 %, indicating that the atmospheric temperature effect should be almost averaged out to zero and contained in standard errors of the superposed density and density gradient distributions in Section 3. This should be also the case for the long-term analysis of the GMDN in Section 4. Figure 29 displays a histogram of the difference (ΔI_0) between fractional deviations of the densities (I_0 and $I_0^{\rm GFS}$) from the averages over each 5-days period in 2009, for a comparison with the superposition analysis in Section 3 in which I also take the fractional deviation of the density from the 5-days average.

I derive $I_0(t)$ and $\xi^{\rm GEO}_{x,y,z}(t)$ from $I_{i,j}(t)$ uncorrected for the temperature effect in this thesis, while another reliable correction analysis of $I_{i,j}(t)$ using the vertical distribution model of the atmospheric temperature is also under development.

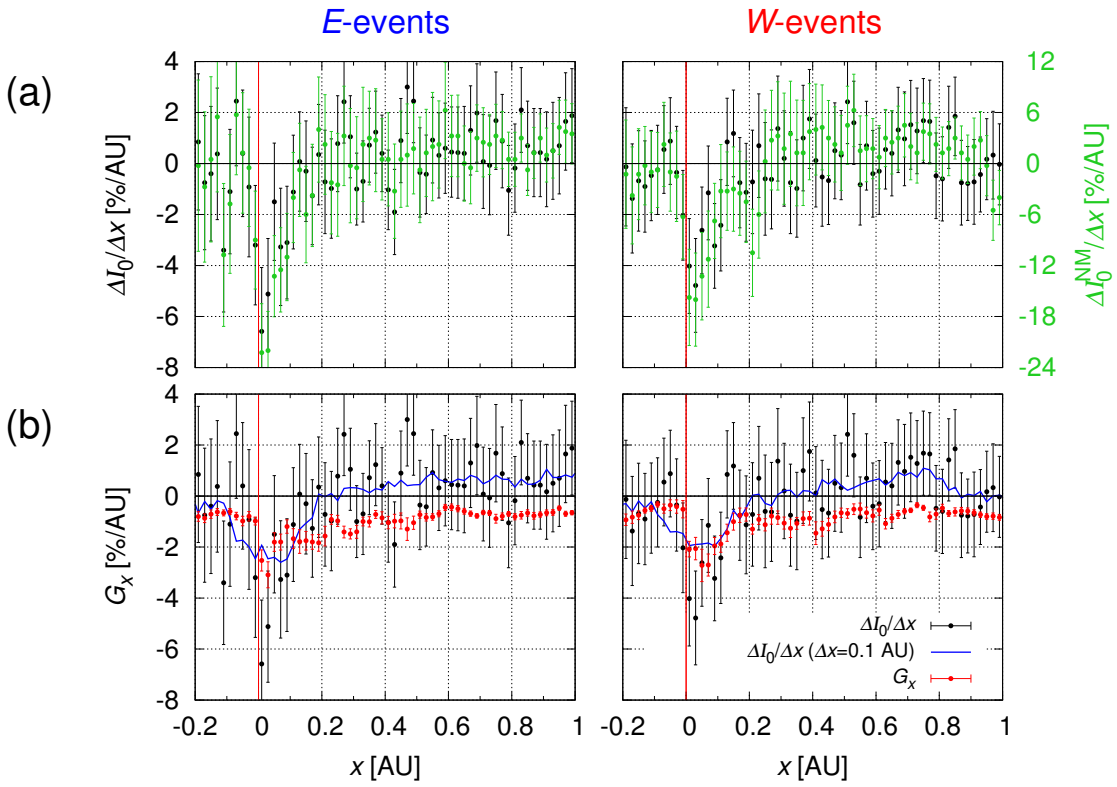

Figure 30: GSE-x component of the density gradient in (left) E- and (right) W- events inferred from the density distributions observed with the GMDN. Black points in panels (a) and (b) represent the gradient calculated with $\Delta x = 0.02$ AU, while a blue curve in panel (b) is the gradient with $\Delta x = 0.1$ AU (see text). A green point in panel (a) is the density gradient inferred from the density distributions observed with NMs, calculated with $\Delta x = 0.02$ AU. Red pints in panel (b) is the same as the black points in Figure 11d, an average of the superposed gradient derived from the anisotropy.

B GCR density gradient inferred from the temporal variation of GCR density

In section 3, I discussed a structure of the GCR depleted region behind IP-shock using the density gradient derived from the first order anisotropy, for the first time. It is thus important to confirm the consistency between the gradient and the density which has been analyzed by most of the former works. In this Appendix, I infer the GSE-x component of the density gradient, G_x, from the observed temporal variation of the density and compare it with G_x derived from the anisotropy.

I calculate the density gradient $\Delta I_0(x)/\Delta x$ from the superposed $I_0(x)$ shown by black points in Figure 10d, as

$$\frac{\Delta I_0(x)}{\Delta x} = \frac{I_0(x+\Delta x) - I_0(x-\Delta x)}{2\Delta x} \tag{150}$$

where Δx is set at $\Delta x = 0.02$ AU as an ad hoc choice. Black points in Figures 30a and 30b display $\Delta I_0(x)/\Delta x$ derived from $I_0(x)$ observed with the GMDN, while green points in Figure 30a show $\Delta I_0^{\rm NM}(x)/\Delta x$, the density gradient inferred from the density distribution ($I_0^{\rm NM}(x)$) observed with NMs, which is displayed by black points in Figure 10e. It is seen that $\Delta I_0(x)/\Delta x$ and $\Delta I_0^{\rm NM}(x)/\Delta x$ are in a good agreement with similar negative enhancements in similar GSE-x range (0 AU $< x <$ +0.2 AU). The magnitude of the enhancement is three times larger in $\Delta I_0^{\rm NM}(x)/\Delta x$ than in $\Delta I_0(x)/\Delta x$.

Red points in Figure 30b are the GSE-x component (G_x) of the density gradient derived from the anisotropy, same as black points in Figure 11d. We cannot confirm a consistency between $\Delta I_0(x)/\Delta x$ and G_x in Figure 30b due to the large fluctuation of $\Delta I_0(x)/\Delta x$, but a negative enhancement of $\Delta I_0(x)/\Delta x$ in 0 AU $< x <$ +0.2 AU seems to be roughly comparable with G_x.

It is noted that the density gradient, or the anisotropy, should be regarded as reflecting a global spatial structure over $\sim$ 0.1 AU comparable to the Larmor radius ($\sim$ 0.2 AU) of $\sim$ 60 GV GCRs in the IMF of $B = 7$ nT. I change, therefore, the spatial interval Δx in equation (150) to $\Delta x = 0.1$ AU. A blue curve in Figure 30b represents $\Delta I_0(x)/\Delta x$ derived from equation (150) with $\Delta x = 0.1$ AU. Magnitude of the negative enhancement in the blue curve is fairly consistent with G_x (black points), indicating that the density gradient derived from the anisotropy reflects a global structure over a spatial scale comparable to the Larmor radius. We also see some differences between $\Delta I_0(x)/\Delta x$ and G_x, e.g. $\Delta I_0(x)/\Delta x$ (blue curve) shows a negative enhancement starting before the SSC onset ($x < 0$ AU), but this is obviously an artificial effect of the central derivative with a large Δx in equation (150). G_x deduced from the anisotropy (red points), on the other hand, shows the enhancement immediately after the SSC onset.

It is also noted that the red points show a negative off-set of ~ -1 %/AU which is not seen in the black points and blue curves derived from the density variation. This indicates the radial density gradient expected from the equilibrium between the radial diffusion and the solar wind convection (see Section 1.1.1), which appears in the first-order anisotropy while does not appear in the density variation.

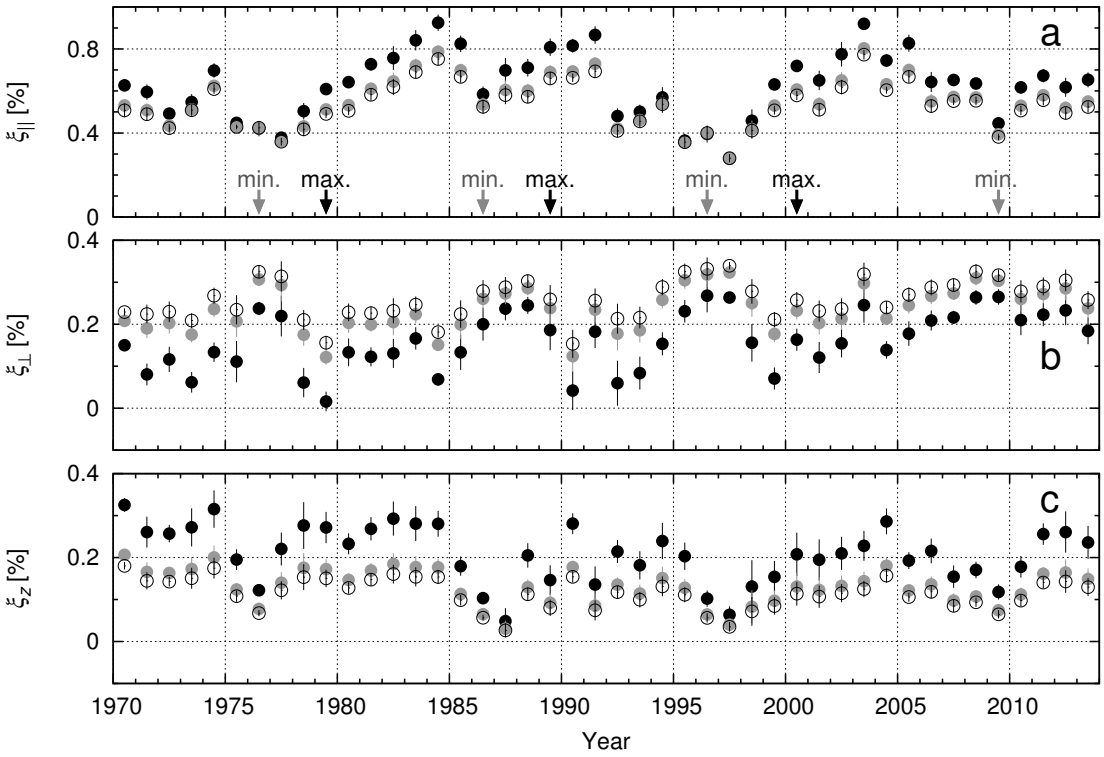

Figure 31: Three components of the free-space anisotropy derived from Nagoya MD data by assuming P_u =100, 200, 300 GV. Solid black, solid gray and open circles represent the components obtained with P_u =100, 200, 300 GV, respectively. (Munakata et al., 2014)

C Dependence on the upper limiting rigidity

In this section, I show how β (the ratio between anisotropies and modulation parameters derived from NM and Nagoya MD data; see Section 4.5) depends on the upper limiting rigidity (P_u) assumed and that our major conclusions on the rigidity dependence derived from β are not affected by changing P_u. Figures 31 and 32 display anisotropy components derived from Nagoya MD and NM data, respectively, with three different P_us. I choose this range of P_u between 100 and 300 GV referring to the solar cycle variation of P_u reported in Munakata et al. (1997). As seen in Figure 32, the anisotropy derived from NM data is almost insensitive to changing P_u as pointed by Bieber & Chen (1991), while the anisotropy derived from Nagoya MD data changes significantly. The increase of P_u with the same spectral index (ν) results in the reduction of the amplitude of the free space anisotropy due to the correlation between these parameters. The increase of P_u also results in the phase of the diurnal anisotropy in free space shifting to earlier hours, due to the reduced average deflection of GCR orbits in the geomagnetic field. Features of anisotropy components in Figure 31 changing with P_u are interpreted in terms of these natures of the free space anisotropy. Table 5 lists average β for three P_us. Firstly, the average $\beta_{\xi_\parallel}$ close to (or slightly smaller than) one for all P_us indicate $\xi_\parallel$ being similar in NM and Nagoya MD data, while it is significantly smaller in $A > 0$ than in $A < 0$ for each P_u. Secondly, the average $\beta_{\xi_\perp}$ and β_{ξ_z} are both significantly larger than one indicating harder rigidity spectra of $\xi_\perp$ and ξ_z than that of $\xi_\parallel$. The average β_{ξ_z} is always larger than the average $\beta_{\xi_\perp}$. Third, the average $\beta_{G_{|z|}}$ and β_{G_r} are significantly smaller than one for all P_us.

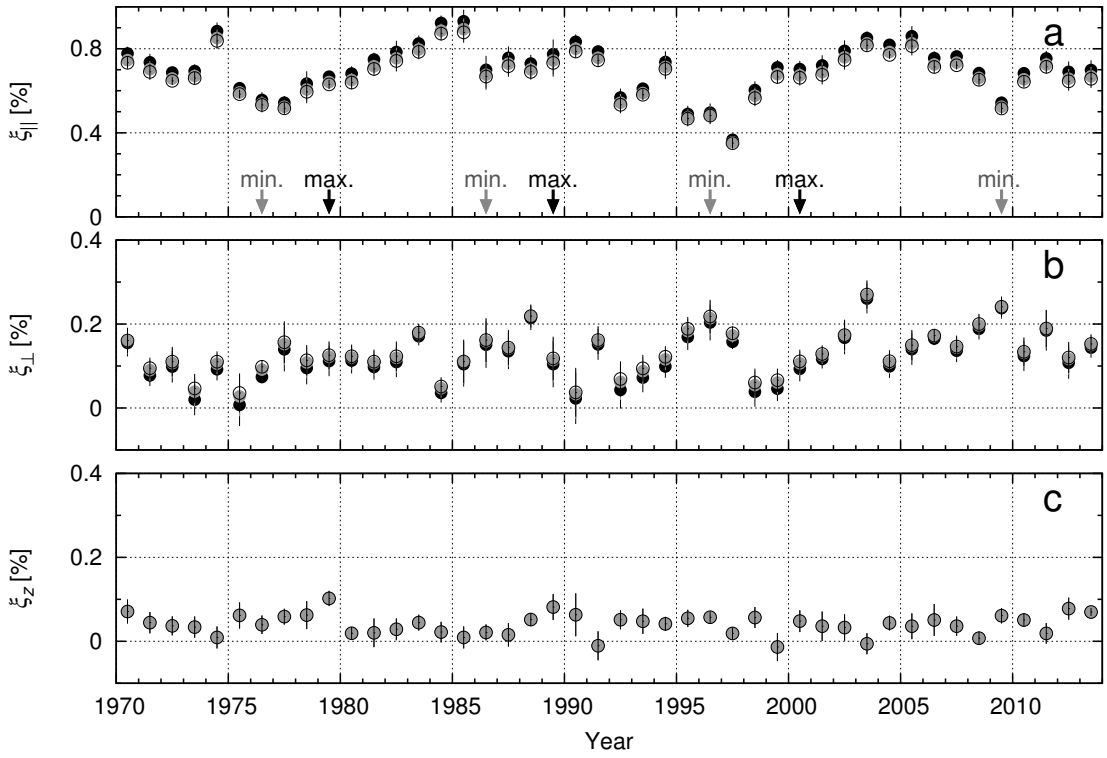

Figure 32: Three components of free-space anisotropy derived from NM data by assuming P_u =100, 200, 300 GV. Solid black, solid gray and open circles represent the components for P_u =100, 200, 300 GV, respectively. (Munakata et al., 2014)

Table 5: Average β values obtained with three different P_us in equation (51). (Munakata et al., 2014)

	polarity	$P_u = 100$GV	$P_u = 200$GV	$P_u = 300$GV
$\beta_{\xi_\parallel}$	$A > 0$	0.77±0.07	0.74±0.06	0.75±0.06
	$A < 0$	0.94±0.05	0.84±0.04	0.82±0.04
	average	0.89±0.05	0.81±0.04	0.79±0.04
$\beta_{\xi_\perp}$	$A > 0$	1.65±0.35	2.24±0.34	2.36±0.33
	$A < 0$	1.26±0.14	1.59±0.14	1.70±0.14
	average	1.35±0.14	1.80±0.13	1.93±0.13
β_{ξ_z}	$A > 0$	4.45±0.61	2.81±0.39	2.45±0.34
	$A < 0$	6.08±0.96	3.82±0.61	3.32±0.53
	average	5.22±0.55	3.29±0.35	2.86±0.31
$\beta_{G_{\vert z\vert}}$	$A > 0$	0.48±0.10	0.68±0.09	0.72±0.09
	$A < 0$	0.35±0.05	0.46±0.05	0.49±0.06
	average	0.39±0.05	0.53±0.05	0.57±0.05
β_{G_r}	$A > 0$	0.85±0.12	0.56±0.08	0.50±0.07
	$A < 0$	0.87±0.13	0.58±0.09	0.52±0.08
	average	0.86±0.08	0.57±0.05	0.51±0.05
$\beta_{\lambda_\parallel}$	$A > 0$	1.00±0.13	1.44±0.18	1.62±0.20
	$A < 0$	1.16±0.15	1.53±0.19	1.65±0.21
	average	1.08±0.09	1.47±0.12	1.61±0.13

The β value is the ratio of the parameter derived from Nagoya MD data at 60 GV to that derived from NM data at 17 GV (see text). Average β values in $A > 0$ and $A < 0$ epochs and in the total period consisting of all $A > 0$ and $A < 0$ epochs are listed. Average value and error are deduced from the average and dispersion of yearly mean values.

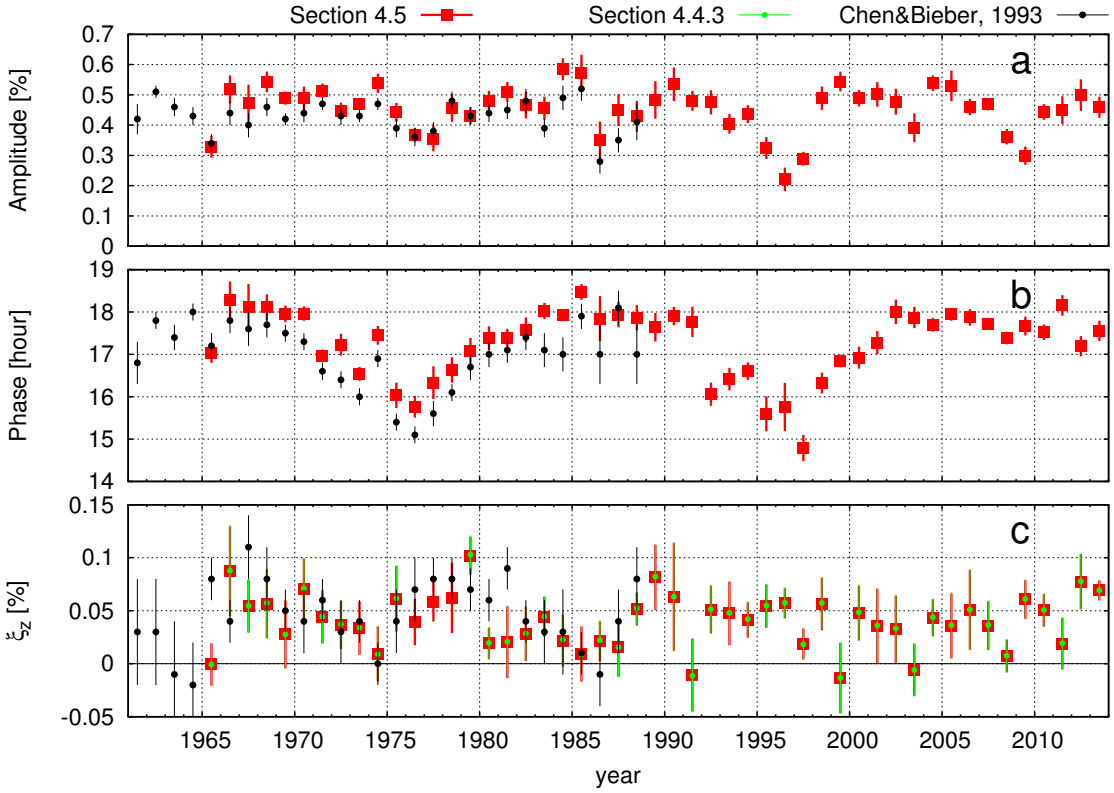

Figure 33: (a) Amplitude and (b) phase of the diurnal anisotropy and (c) the NS anisotropy, each derived from NM data. Red squares display yearly means of the monthly diurnal and NS anisotropies derived by equations (119) and (120) in Section 4.5, respectively, i.e. the same as open circles in Figures 20 and 21c. A green point in the panel (c) represents an yearly mean of the NS anisotropy derived in Section 4.4.3. Daily mean NS anisotropy derived by equation (108) in Section 4.4.3 is averaged over each IMF sectors in every month and I calculated ξ_z in equation (93) and its yearly means shown by the green points. The anisotropy components listed by table 2 of Chen & Bieber (1993) are also plotted with black points.

D Comparison of the anisotropy components derived from NM data

In Section 4.5, I deduced the diurnal and NS anisotropies from NM data every month and obtained yearly means of them, in the same manner as Chen & Bieber (1993). I also deduced the NS anisotropy on a daily basis in Section 4.4.3. This analysis using equation (108) is based on the analysis method of Chen & Bieber (1993), while they derived only the 27-days or yearly averages of the NS anisotropy and this analysis method deriving the daily NS anisotropy was performed for the first time by this thesis. In this section, I compare the diurnal and NS anisotropies derived in this thesis with those derived by Chen & Bieber (1993), which are listed in table 2 of the paper.

Red squares display yearly means of the monthly diurnal and NS anisotropies derived by equations (119) and (120) in Section 4.5, respectively, i.e. the same as open circles in Figures 20 and 21c. The period displayed by red squares is expanded to 1960's from which the NM data are available in the web page of Bartol Research Institute[12]. The black points display those derived by Chen & Bieber (1993). In the panels (a) and (b), we can see that the amplitude and phase are slightly larger and later, respectively, in the red squares than in the black points. Major part of

[12]http://neutronm.bartol.udel.edu/

this difference is assigned to a contribution from the Compton-Getting anisotropy arising from the earth's orbital motion around the sun. I derived the diurnal anisotropy in free space, red squares in Figures 33a and 33b, by equation (119) in which the harmonics $(a_{\rm Newark}, b_{\rm Newark})$ measured on the ground has already been corrected for the Compton-Getting anisotropy by subtracting $(a^{\rm CG}_{\rm Newark}, b^{\rm CG}_{\rm Newark})$ derived in equation (117). The black points in Figure 33 derived by Chen & Bieber (1993) are, on the other hand, not corrected for the Compton-Getting anisotropy. They subtracted the Compton-Getting anisotropy after deriving the free space harmonics. The correction for the Compton-Getting anisotropy shifts the uncorrected diurnal anisotropy toward the direction of 18:00 local solar time with a magnitude of ~ 0.05 %, causing an enlargement and a delay of the amplitude and the phase, respectively, when the uncorrected diurnal anisotropy points the phase between 12:00 and 18:00 local solar time, in agreement with the difference between the red squares and the black points in Figures 33a and 33b.

In Figure 33c displaying the yearly mean NS anisotropy defined by equation (93), most of the red squares derived in Section 4.5 are consistent with black points derived by Chen & Bieber (1993) within the error bars, which are calculated from the dispersions of the monthly (or 27-days) mean NS anisotropies in this thesis (or Chen & Bieber, 1993). A portion of the difference between the red squares and the black points is attributed to the difference of the time interval (a month or 27 days) in which the mean anisotropies are calculated by equation (93). The another portion is due to the difference of the data set used to identify the IMF sector polarity, i.e. the solar mean magnetic field provided by WSO is mainly used in this thesis while the Svalgaard's inferred magnetic polarity is used in Chen & Bieber (1993). These differences also contribute to the diurnal anisotropy in Figures 33a and 33b. It is noted that the difference between the red squares and the black points in Figure 33c is almost comparable to the error of each early mean value.

Green points in Figure 33c display the NS anisotropy obtained in Section 4.4.3. Daily mean NS anisotropy derived by equation (108) is averaged over each IMF sectors in every month and I calculated ξ_z in equation (93) and its yearly means. This NS anisotropy is not calculated for a period between 1976 and 1978 because of the lack of Thule NM data. We can see that the NS anisotropy deduced in Section 4.4.3 (green points) is fairly consistent with that derived in Section 4.5 (red squares). It is noted that the green points are derived from equation (108) with the coupling coefficient $b_{\rm NS} = 1.0648$ in equation (114) on an assumption of the upper limiting rigidity $P_u = \infty$, while the red squares and black points in all panels are derived from the coupling coefficients for $P_u = 100$ GV, obtained in equation (122) as $b_{\rm NS} = 1.0548$ for the NS anisotropy. The difference of $b_{\rm NS}$ is, however, only a order of 1 % and invisible in Figure 33c.

References

Agrawal, S. P. 1983, Solar cycle variations of cosmic ray intensity and large-scale structure of the heliosphere, Space Sci. Rev., 34, 127-135.

Ahluwalia, H. S. 1988, Is threre a twenty year wave in the diurnal anisotropy of cosmic rays?, Geophys. Res. Lett., 15, 287-290.

Alfvén, H., 1942, Existence of electromagnetic-hydrodynamic waves, Nature, 150, 405-406.

Amenomori, M., and Tibet ASγ Collaboration, 2004, Observation by an air-shower array in Tibet of the Multi-TeV cosmic-ray anisotropy due to terrestrial orbital motion around the sun, Phys. Rev. Lett., 93:061101, 1-4.

Barnden, L. R., 1973a, Forbush decreases 1966-1972; Their solar and interplanetary associations and their anisotropies, proc. 13th ICRC, 2, 1271-1276.

Barnden, L. R., 1973b, The large-scale magnetic field configuration associated with Forbush decreases, proc. 13th ICRC, 2, 1277-1282.

Bercovitch, M., 1963, Day to day study of the diurnal variation of cosmic-ray intensity, J. Geophys. Res., 68, 4366-4368.

Bieber, J. W., and M. A. Pomerantz, 1986, Solar cycle variation of cosmic-ray north-south anisotropy and radial gradient, Astrophys. J., 303, 843-848.

Bieber, J. W., P. Evenson, and W. Matthaeus, 1987, Magnetic helicity of the IMF and the solar modulation of cosmic rays, Geophys. Res. Lett., 14, 864-867.

Bieber, J. W., and J. Chen, 1991, Cosmic-ray diurnal anisotropy, 1936-1988: Implications for drift and modulation theories, Astrophys. J., 372, 301-313.

Bieber, J. W., W. H. Matthaeus, and C. W. Smith., 1994, Proton and electron mean free paths: the Palmer consensus revisited, Astrophys. J., 420, 294-306.

Bieber, J. W., and P. Evenson, 1998, CME geometry in relation to cosmic ray anisotropy, Geophys. Res. Lett., 25, 2955-2958.

Bieber, J. W., W. H. Matthaeus, and A. Shalchi, 2004, Nonlinear guiding center theory of perpendicular diffusion: general properties and comparison with observation, Geophys. Res. Lett., 31:L10805, 1-4.

Biermann, L., 1957, Solar corpuscular radiation and the interplanetary gas, Observatory, 77, 109-110.

Burlaga, L., E. Sittler, F. Mariani, R. Schwenn, 1981, Magnetic loop behind an interplanetary shock: Voyager, Helios, and IMF 8 observations, J. Geophys. Res., 86, 6673-6684.

Cane, H. V., 1988, The large-scale structure of flare-associated interplanetary shocks, J. Geophys. Res., 93, 1-6.

Cane, H. V., I. G. Richardson, and T. T. von Rosenvinge, 1994, Cosmic ray decreases and shock structure: A multispacecraft study, J. Geophys. Res., 99, 21,429-21,441.

Cane, H. V., I. G. Richardson, and T. T. von Rosenvinge, 1996, Cosmic ray decreases: 1964-1994, J. Geophys. Res., 101, 21,561-21,572.

Cane, H. V., 2000, Coronal mass ejections and Forbush decreases, Space Sci. Rev., 93, 55-77.

Cane, H. V., and I. G. Richardson, 2003, Interplanetary coronal mass ejections in the near-Earth solar wind during 1996-2002, J. Geophys. Res., 108:1156, 1-13.

Chapman, S., and J. Bartels, 1940, Geomagnetism, 2, 611, Oxford University Press, Oxford

Chen, J., and J. W. Bieber, 1993, Cosmic-ray anisotropies and gradients in three dimensions, Astrophys. J., 405, 375-389.

Compton, A. H. and I. A. Getting, 1935, An apparent effect of galactic rotation on the intensity of cosmic rays, Phys. Rev., 47, 817-821.

Cutler, D. J., and D. E. Groom, 1986, Observation of terrestrial orbital motion using the cosmic-ray Compton-Getting effect, Nature, 322, 434-436.

Duggal, S. P., and M. A. Pomerantz, 1962, Progressive rotation of cosmic-ray diurnal variation vector, Phys. Rev. Lett., 8, 215-216.

Duggal, S. P., and M. A. Pomerantz, 1969, Transient north-south asymmetries of cosmic radiation, proc. 11th ICRC, 2, 351-358.

Erdös, G., and J. Kóta, 1980, Sector structure of the interplanetary magnetic field and anisotropy of 50-1000 GV, Astrophys. Space Sci., 67, 45-59.

Fan, C. Y., P. Meyer, and J. A. Simpson, 1960, Cosmic radiation intensity decreases observed at the earth and in the nearby planetary medium, Phys. Rev. Lett., 4, 421-423.

Forbush, S. E., 1937, On the effects in cosmic-ray intensity observed during the recent magnetic storm, Phys. Rev., 51, 1108-1109.

Forbush, S. E. 1967, A variation, with a period of two solar cycles, in the cosmic-ray diurnal anisotropy, J. Geophys. Res., 72, 4937-4939.

Fujimoto, K., A. Inoue, K. Murakami, and K. Nagashima, 1984, Coupling coefficients of cosmic ray daily variations for meson telescopes, Rep. Cosmic-Ray Res. Lab., 9.

Fushishita, A., T. Narumi, C. Kato, S. Yasue, K. Munakata, Y. Okazaki, T. Kuwabara, J. W. Bieber, P. Evenson, M. R. Da Silva, A. Dal Lago, N. J. Schuch, M. Tokumaru, M. L. Duldig, J. E. Humble, I. Sabbah, and J. Kóta, 2010a, Drift effects and the average features of cosmic ray density gradient in CIRs during successive two solar minimum periods, Adv. Geosci., 21, 199-210.

Fushishita, A., T. Kuwabara, C. Kato, S. Yasue, J. W. Bieber, P. Evenson, M. R. Da Silva, A. Dal Lago, N. J. Schuch, M. Tokumaru, M. L. Duldig, J. E. Humble, I. Sabbah, H. K. Al Jassar, M. M. Sharma, and K. Munakata, 2010b, Precursors of the Forbush decrease on 2006 December 14 observed with the Global Muon Detector Network (GMDN), Astrophys. J., 715, 1239-1247.

Gopalswamy, N., S. Yashiro, and S. Akiyama, 2007, Geoeffectiveness of halo coronal mass ejections, J. Geophys. Res., 112:A06112, 1-13.

Gleeson, L. J., 1969, The equations describing the cosmic-ray gas in the interplanetary region, Planet. Space Sci., 17, 31-47.

Gleeson, L. J., and W. I. Axford, 1967, Cosmic rays in the interplanetary medium, Astrophys. J. Lett., 149, L115-L118.

Gleeson, L. J., and W. I. Axford, 1968, The Compton-Getting effect, Astrophys. Space Sci., 2, 431-437.

Gleeson, L. J., and W. I. Axford, 1968, Solar modulation of galactic cosmic rays, Astrophys. J., 154, 1011-1026.

Gleeson, L. J., and I. H. Urch, 1973, A study of the force-field equation for the propagation of galactic cosmic rays, Astrophys. Space Sci., 25, 387-404.

Gleeson, L. J., and G. M. Webb, 1980, The propagation of cosmic-rays in the interplanetary region (the theory), Fundamentals of Cosmic Phys., 6, 187-312.

Hall, D. L., J. E. Humble, and M. L. Duldig, 1994, Modulation of high-energy cosmic rays in the heliosphere, J. Geophys. Res., 99, 21,433-21,455.

Hall, D. L., M. L. Duldig, and J. E. Humble, 1996, Analysis of sidereal and solar anisotropies in cosmic rays, Space Sci. Rev., 78, 401-442.

Hall, D. L., M. L. Duldig, and J. E. Humble, 1997, Cosmic-ray modulation parameters derived from the solar diurnal variation, Astrophys. J., 482, 1038-1049.

Haurwitz, M. W., S. Yoshida, and S.-I. Akasofu, 1965, Interplanetary magnetic field asymmetries and their effects on polar cap absorption events and Forbush decreases, J. Geophys. Res., 70, 2977-2988.

Hess. V. F., and H. T. Graziadei, 1936, On the diurnal variation of the cosmic radiation, Terrestrial Magnetism and Atmospheric Electricity, 41, 9-14.

Hirshberg, J., A. Alksne, D. S. Colburn, S. J. Bame, and A. J. Hundhausen, 1970, Observation of a solar flare induced interplanetary shock and helium-enriched driver gas, J. Geophys. Res., 75, 1-15.

Hundhausen, A. J., 1972, Interplanetary shock waves and the structure of solar wind disturbances, Solar Wind, C. P. Sonett et al. (eds.), NASA Spec. Publ. SP, 308, 393-417.

Isenberg, P. A., and J. R. Jokipii, 1979, Gradient and curvature drifts in magnetic fields with arbitary spatial variation, Astrophys. J., 234, 746-752.

Jokipii, J. R., 1971, Propagation of cosmic rays in the solar wind, Rev. Geophys. Space Phys., 9, 27-87.

Jokipii, J. R., and D. A. Kopriva, 1979, Effects of particle drift on the transport of cosmic rays. Ⅲ. Numerical models of galactic cosmic-ray modulation, Astrophys. J., 234, 384-392.

Jordan, A. P., H. E. Spence, J. B. Blake, and D. N. A. Shaul, 2011, Revisiting two-step Forbush decreases, J. Geophys. Res., 116:A11103, 1-13.

Kamiya, Y., 1961, Solar magnetic cloud producing cosmic-ray storm, magnetic storm and Type Ⅳ solar radio outburst, J. Geomagnet. Geoelec. Kyoto, 13, 33-41.

King, J. H., and N.E. Papitashvili 2005, Solar wind spatial scales in and comparisons of hourly Wind and ACE plasma and magnetic field data, J. Geophys. Res., 110:A02104, 1-8.

Klein, L. W., L. F. Burlaga, 1982, Interplanetary magnetic clouds at 1 AU, J. Geophys. Res., 87, 613-624.

Klimas, A. J., and G. Sandri, 1971, Foundation of the theory of cosmic-ray transport in random magnetic fields, Astrophys. J., 169, 41-56.

Kóta, J., and J. R. Jokipii, 1982, Cosmic rays near the heliospheric current sheet, Geophys. Res. Lett., 9, 656-659.

Kóta, J., and J. R. Jokipii, 1983, Effects of drift on the transport of cosmic rays. Ⅵ. A three-dimensional model including diffusion, Astrophys. J., 265, 573-581.

Kóta, J., and J. R. Jokipii, 2001, The anisotropies of galactic cosmic rays: 3-dimensional modeling, Adv. Space Res., 27, 607-612.

Kozai, M., K. Munakata, C. Kato, T. Kuwabara, J. W. Bieber, P. Evenson, M. Rockenbach, A. Dal Lago, N. J. Schuch, M. Tokumaru, M. L. Duldig, J. E. Humble, I. Sabbah, H. K. Al Jassar, M. M. Sharma, and J. Kóta, 2014, The spatial density gradient of galactic cosmic rays and its solar cycle variation observed with the Global Muon Detector Network, Earth, Planets and Space, 66:151, 1-8.

Kozai, M., K. Munakata, C. Kato, T. Kuwabara, M. Rockenbach, A. Dal Lago, N. J. Schuch, C. R. Braga, R. R. S. Mendonça, H. K. Al Jassar, M. M. Sharma, M. L. Duldig, J. E. Humble, P. Evenson, I. Sabbah, and M. Tokumaru, 2016, Average spatial distribution of cosmic rays behind the interplanetary shock –Global Muon Detector Network observations–, Astrophys. J., submitted.

Kuwabara, T., K. Munakata, S. Yasue, C. Kato, S. Akahane, M. Koyama, J. W. Bieber, P. Evenson, R. Pyle, Z. Fujii, M. Tokumaru, M. Kojima, K. Marubashi, M. L. Duldig, J. E. Humble, M. R. Da Silva, N. B. Trivedi, W. D. Gonzalez, and N. J. Schuch, 2004, Geometry of an interplanetary CME on October 29, 2003 deduced from cosmic rays, Geophys. Res. Lett., 31:L19803, 1-5.

Kuwabara, T., 2005, Doctoral Dissertation of Shinshu University.

Kuwabara, T., J. W. Bieber, P. Evenson, K. Munakata, S. Yasue, C. Kato, A. Fushishita, M. Tokumaru, M. L. Duldig, J. E. Humble, M. R. Da Silva, A. Dal Lago, and N. J. Schuch, 2009, Determination of interplanetary coronal mass ejection geometry and orientation from ground-based observations of galactic cosmic rays, J. Geophys. Res., 114:A05109, 1-10.

Laurenza, M., M. Storini, G. Moreno, Z. Fujii, 2003, Interplanetary magnetic field polarities inferred from the north-south cosmic ray anisotropy, J. Geophys. Res., 108:1069, 1-7.

le Roux, J. A., and M. S. Potgieter, 1991, The simulation of Forbush decreases with time-dependent cosmic-ray modulation models of varying complexity, Astron. Astrophys., 243, 531-545.

Levy, E. H. 1976, Theory of the solar magnetic cycle wave in the diurnal variation of energetic cosmic rays: Physcal basis of the anisotropy, J. Geophys. Res., 81, 2082-2088.

Lin, Z., J. W. Bieber, and P. Evenson, 1995, Electron trajectories in a model magnetosphere: simulation and observation under active conditions, J. Geophys. Res., 100, 23543-23549.

Liu, Y., J. G. Luhmann, R. Müller-Mellin, P. C. Schroeder, L. Wang, R. P. Lin, S. D. Bale, Y. Li, M. H. Acuña, and J.-A. Sauvaud, 2008, A comprehensive view of the 2006 december 13 CME: From the sun to interplanetary space, Astrophys. J., 689, 563-571.

Lockwood, J. A., 1960, An investigation of the Forbush decreases in the cosmic radiation, J. Geophys. Res., 65, 3859-3880.

McComas, D. J., Ebert, R. W., Elliott, H. A., Goldstein, B. E., Gosling, J. T., Schwadron, N. A., Skoug, R. M. 2008, Weaker solar wind from the polar coronal holes and the whole sun, Geophys. Res. Lett., 35:L18103, 1-5.

Mewaldt, R. A., Davis, A. J., Lave, K. A., Leske, R. A., Stone, E. C., Wiedenbeck, M. E., Binns, W. R., Christian, E. R., Cummings, A. C., de Nolfo, G. A., Israel, M. H., Labrador, A. W., von Rosenvinge, T. T. 2010, Astrophys. J. Lett., 723, L1-L6.

Minnie, J., Bieber, J. W., Matthaeus, W. H., Burger, R. A. 2007, Suppression of particle drifts by turbulence, Astrophys. J., 670, 1149-1158.

Mori, S., and K. Nagashima, 1979, Inference of sector polarity of the interplanetary magnetic field from the cosmic ray north-south asymmetry, Planet. Space Sci., 27, 39-46.

Mori, S., S. Sagisaka, and S. Yasue, 1988, The atmospheric temperature effect on the diurnal variation of cosmic-ray muon intensity observed at 220 m.w.e underground at Matsushiro, J. Geomag. Geoelectr., 40, 1023-1033.

Morishita, I., K. Nagashima, S. Sakakibara, and K. Munakata, 1990, Long term changes of the rigidity spectrum of Forbush decrease, proc. 21st ICRC, 6, 217-219.

Munakata, K., H. Miyasaka, D. L. Hall, S. Yasue, C. Kato, Z. Fujii, K. Fujimoto, and S. Sakakibara, 1997, Long term variation of cosmic-ray diurnal anisotropy observed by a network of multi-directional muon telescopes in a wide range of rigidity, proc. 25th Internat. Cosmic Ray Conf.(Durban), 2, 77-80.

Munakata, K., H. Miyasaka, I. Sakurai, S. Yasue, C. Kato, S. Akahane, S. Koyama, D. L. Hall, Z. Fujji, K. Fujimoto, S. Sakakibara, J. E. Humble, and M. L. Duldig, 2002, Solar cycle variations of modulation parameters of galactic cosmic-rays in the heliosphere, Adv. Space Res., 29, 1527-1532.

Munakata, K., T. Kuwabara, J. W. Bieber, S. Yasue, C. Kato, S. Akahane, M. Koyama, P. Evenson, R. Pyle, Z. Fujii, M. L. Duldig, J. E. Humble, M. R. Silva, N. B. Trivedi, W. D. Gonzalez, and N. J. Schuch, 2003, CME geometry deduced from cosmic ray anisotropy, proc. 28th ICRC, 6, 3561-3564.

Munakata, K., S. Yasue, C. Kato, J. Kota, M. Tokumaru, M. Kojima, A. A. Darwish, T. Kuwabara, and J. W. Bieber, 2006, On the cross-field diffusion of galacitc cosmic rays into an ICME, Adv. Geosci., 2, 115-124.

Munakata, K., M. Kozai, C. Kato, and J. Kóta, 2014, Long-term variation of the solar diurnal anisotropy of galactic cosmic rays observed with the Nagoya multi-directional muon detector, Astrophys. J., 791:22, 1-16.

Murakami, K., K. Nagashima, S. Sagisaka, Y. Mishima, A. Inoue, 1979, Response functions for cosmic-ray muons at various depths underground, IL Nuovo Cimento, 2C, 635-651.

Nagashima, K., S. P. Duggal, and M. A. Pomerantz, 1968, Cosmic ray anisotropy in three-dimensional space: Part I–Formulation of cosmic ray dailyl variation produced by axis-symmetric anisotropy, Planet. Space Sci., 16, 29-46.

Nagashima, K., 1971, Three-dimensional cosmic ray anisotropy in interplanetary space, Rep. Ionos. Space Res. Japan, 25, 189-211.

Nagashima, K., K. Fujimoto, Z. Fujii, H. Ueno, and I. Kondo, 1972, Three-dimensional cosmic ray anisotropy in interplanetary space: Part IV–Origin of solar semi-diurnal variation, Rep. Ionos. Space Res. Jpn., 26, 31-68.

Nagashima, K., S. Sakakibara, A. G. Fenton, and J. E. Humble, 1985, The intensity of the cosmic ray galactic anisotropy to heliomagnetic polarity reversals, Planet. Space Sci., 33, 395-405.

Neher, H. V., and H. R. Anderson, 1964, Change of cosmic-ray intensity with distance from the sun, J. Geophys. Res., 69, 1911-1913.

Nishida, A., 1982, Numerical evaluation of the precursory intcrease to the Forbush decrease expected from the diffusion convection model., J. Geophys. Res., 87, 6003-6009.

Obayashi, T., 1962, Propagation of solar corpuscles and interplanetary magnetic fields, J. Geophys. Res., 67, 1717-1729.

O'Gallagher, 1967, Cosmic-ray radial density gradient and its rigidity dependence observed at soalr minimum on Mariner IV, Astrophys. J., 150, 675-698.

O'Gallagher, J. J., and J. A. Simpson, 1967, The heliocentric intensity gradients of cosmic-ray protons and helium during minimum solar modulation, Astrophys. J., 147, 819-827.

Oh, S. Y., Y. Yi, and J. W. Bieber, 2010, Modulation cycles of galactic cosmic ray diurnal anisotropy variation, Sol. Phys., 262, 199-212.

Okazaki, Y., A. Fushishita, T. Narumi, C. Kato, S. Yasue, T. Kuwabara, J. W. Bieber, P. Evenson, M. R. Da Silva, A. Dal Lago, N. J. Schuch, Z. Fujii, M. L. Duldig, J. E. Humble, I. Sabbah, J. Kóta, and K. Munakata, 2008, Drift effects and the cosmic ray density gradient in a solar rotation period: First observation with the Global Muon Detector Network (GMDN), Astrophys. J., 681, 693-707.

Parker, E. N., 1957, Newtonian development of the dynamical properties of ionized gases of low density, Phys. Rev., 107, 924-933.

Parker, E. N., 1958, Dynamics of the interplanetary gas and magnetic fields, Astrophys. J., 128, 664-676.

Parker, E. N., 1965, The passage of energetic charged particles through interplanetary space, Planet. Space Sci., 13, 9-49.

Potgieter, M. S., and H. Moraal, 1985, A drift model for the modulation of galactic cosmic rays, Astrophys. J., 294, 425-440.

Rao, U. R., K. G. McCracken, and D. Venkatesan, 1963, Asymptotic cones of acceptance and their use in the study of the daily variation of cosmic radiation, J. Geophys. Res., 68, 345-369.

Reames, D. V., 1995, Solar energetic particles: A paradigm shirt, Rev. Geophys. (Suppl.), 33, 585-589.

Reames, D. V., L. M. Barbier, and C. K. Ng, 1996, The spatial distribution of particles acceletated by coronal mass ejection-driven shocks, Astrophys. J., 466, 473-486.

Richardson, I. G., and H. V. Cane, 2010, Near-earth interplanetary coronal mass ejections during solar cycle 23 (1996-2009): Catalog and summary of properties, Sol. Phys., 264, 189-237.

Rockenbach, M., M., A. Dal Lago, N. J. Schuch, K. Munakata, T. Kuwabara, A. G. Oliveira, E. Echer, C. R. Braga, R. R. S. Mendonça, C. Kato, M. Kozai, M. Tokumaru, J. W. Bieber, P. Evenson, M. L. Duldig, J. E. Humble, H. K. Al Jassar, M. M. Sharma, and I. Sabbah, 2014, Global Muon Detector Network used for space weather applications, Space Sci. Rev., 182, 1-18.

Sakakibara, S., K. Munakata, and K. Nagashima, 1985, Rigidity spectrum of Forbush decrease, proc. 19th ICRC, 5, 238-241.

Sakakibara, S., K. Munakata, and K. Nagashima, 1987, Rigidity spectrum of Forbush decrease, proc. 20th ICRC, 4, 67-70.

Sarris, E. T., C. A. Dodopoulos, and D. Venkatesan, 1989, On the E-W asymmetry of Forbush decreases, Sol. Phys., 120, 153-172.

Schardt, A. W., and A. G. Opp, 1967, Particles and Fields: Significant achievements, Rev. Geophys., 5, 411-446.

Schatten, K. H., J. M. Wilcox, and N. F. Ness, 1969, A model of interplanetary and coronal magnetic fields, Sol. Phys., 6, 442-455.

Sinno, K., 1962, Mechanism of cosmic ray storms inferred from some statistical results, J. Phys. Soc. Japan, 17, Suppl. A-Ⅱ, 395-399.

Smith, E. J., 1983, Observations of interplanetary shocks: recent progress, Space Sci. Rev., 34, 101-110.

Suda, T., S. Kudo, and M. Wada, 1981, Cosmic ray N-S asymmetry and interplanetary magnetic field, proc. 17th ICRC, SH 8.2-15.

Swinson, D. B., 1969, 'Sidereal' cosmic-ray diurnal variations, J. Geophys. Res., 74, 5591-5598.

Thambyahpillai, T., and H. Eliiot, 1953, World-wide changes in the phase of the cosmic-ray solar daily variation, Nature, 171, 918-920.

Wada, M., and T. Suda, 1980, Average features of cosmic ray variation associated with sudden commencement of magnetic strom, Scientific Papers of the Institute of Physical and Chemical Research, 74, 1-12.

Wang, C., C. X. Li, Z. H. Huang, and J. D. Richardson, 2006, Effect of interplanetary shock strengths and orientations on storm sudden commencement rise times, Geophys. Res. Lett., 33:L14104, 1-3.

Webb, G. M., and L. J. Gleeson, 1979, On the equation of transport for cosmic-ray particles in the interplanetary region, Astrophys. Space Sci., 60, 335-351.

Wibberenz, G., J. A. le Roux, M. S. Potgieter, and J. W. Bieber, 1998, Transient effects and disturbed conditions, Space Sci. Rev., 83, 309-348.

Wilcox, J. M., and N. F. Ness, 1965, Quasi-stationaly corotating structure in the interplanetary medium, J. Geophys. Res., 70, 5793-5805.

Yasue, S., 1980, North-South anisotropy and radial density gradient of galactic cosmic rays, J. Geomag. Geoelectr., 32, 617-635.

Yasue, S., S. Sakakibara, and K. Nagashima, 1982, Coupling Coefficients of Cosmic Ray Daily Variations for Neutron Monitor Stations, (CRRL Rep., No. 7; Nagoya, Japan: Cosmic-Ray Research Laboratory)

Yermolaev, Y. I., and M. Y. Yermolaev, 2006, Statistic study on the geomagnetic storm effectiveness of solar and interplanetary events, Adv. Space Res., 37, 1175-1181.

Yoshida, S. and S.-I. Akasofu, 1965, A study of the propagation of solar particles in interplanetary space, Planet. Space Sci., 13, 435-448.